2017

Assessment of the High-Resolution Sediment Gravity Flow Record in Prince William Sound, Alaska

Elisabeth Rose Clyne
College of William and Mary - Virginia Institute of Marine Science, erclyne@email.wm.edu

Assessment of the High-Resolution Sediment Gravity Flow Record in Prince William Sound, Alaska.

A Thesis

Presented to

The Faculty of the School of Marine Science

The College of William and Mary in Virginia

In Partial Fulfillment

of the Requirements for the Degree of

Master of Science

---

by

Elisabeth R. Clyne

January 2018

APPROVAL SHEET

This Thesis is submitted in the partial fulfillment of

the requirements for the degree of

Master of Science

_____

Elisabeth R. Clyne

Approved, by the Committee, December 2017

_____

Steven A. Kuehl, Ph.D.

Committee Chairman/ Advisor

_____

Courtney K. Harris, Ph.D.

_____

Chris J. Hein, Ph.D.

_____

James E. Perry, Ph.D.

_____

Joshua R. Williams, Ph.D.

TABLE OF CONTENTS

ACKNOWLEDGEMENTS

I would to thank everyone involved with the data gathering and processing in this thesis. Thanks to Robert Krimmel and Lee Liberty, for providing data on the lake levels and seismic tracklines. To the faculty and staff at Texas A&M, Baylor, Northern Arizona University, and the Large Lakes Observatory for conducting crucial analyses. To Amanda Knobloch, for helping with the stable carbon and nitrogen analyses and Mary Goodwyn and Kendall Rosenberg for help in the sediment lab. To David and Annette Janka, crew of the *Auklet*, and Alicia Williams for their invaluable work, care, and information; the coring (and this thesis) would not have been possible without your effort! Thanks to Mohammad Al Mukaimi for help with the coring and analyses. Thanks to Eric Miller, Nicole Marshall, and Timothy Dellapenna for conducting crucial analysis which laid the foundations of this thesis. To all classmates who helped me while writing this thesis. To my committee members Courtney Harris, Jim Perry, and Chris Hein for providing both professional and personal advice to me along the way. Special thanks to Josh Williams for footing the bill and working so closely with me at all times of the day and year, in the lab, office, and field, to push this project through. To my adviser, Steve Kuehl, for helping me develop, undertake, and complete this project. And of course to my parents and friends for the much needed emotional support. I know I can be a whirlwind of ideas and emotions, but thanks for sticking with me through the thick and this

LIST OF TABLES

LIST OF FIGURES

ABSTRACT

South-Central Alaska is one of the most seismically active and climatologically sensitive places in the world. Within this region, Prince William Sound (PWS) receives abundant sediment from multiple sources, potentially housing a high-resolution environmental record spanning the past 4,000 years. Inputs to PWS are derived from local rivers and glaciers, and may include earthquake- and glacial-outburst-triggered sediment gravity flows. Therefore, this is an ideal location to investigate the long-term record of seismic, glacial, and riverine activity. This study examines the elemental, grain size, and stable isotope signatures in PWS to identify gravity flow deposits and the potential paleoseismic and paleoclimate record. Previous sediment core studies have focused on central and southern PWS, and this study fills a knowledge gap on sediment characteristics in northern PWS. Shelf sediments are transported into PWS via Hinchinbrook Inlet during winter storms, and the Copper River plume is advected into PWS during summer months. Local sources in PWS and the Copper River/Shelf sediments in southern PWS have unique signatures of Sr/Pb, Cu/Pb, K/Ca, Rb/Sr, and Rb/Ca. As a result, sediment gravity flows originating from different locations have distinct provenance signatures and can be distinguished from locally emplaced sediment. Six cores in central and northern PWS were collected and sedimentation rates were determined by ^{210}Pb, ^{137}Cs, and ^{239,240}Pu geochronology. The cores were assessed for elemental content and grain size patterns to identify gravity flow deposits. Deposits, sedimentation rates, and provenance were correlated with five previously collected cores in southern and central PWS. The stable isotopic content of ^{13}C and ^{15}N were assessed across all eleven cores. The sedimentation rates, mean grain size, Sr/Pb and Cu/Pb all decrease moving northward through PWS, and sediments derived in northern PWS have the lowest Sr/Pb, Cu/Pb, δ^{13}C, δ^{15}N, and C/N and highest K/Ca, Rb/Sr, and Rb/Ca values observed. This trend is due to decreasing influence from the Copper River and shelf sediments in the south and increasing influence of local PWS sources in the north. Using these distinct provenances, several earthquake deposits were identified. Earthquakes of magnitudes $6.0 < M_w < 7.0$ produced deposits in the central channel, and those of $M_w \geq 7.0$ with epicenters in PWS had distinctly mixed signatures from generating numerous flows throughout the region. We also identified a flow sourced near the Columbia Glacier region which may have derived from earthquake activity or the glacier's rapid retreat. Based on spatial analysis of the eleven gravity cores, the most robust gravity flow records are captured within deep ponded sediment basins and the area spanning the southern end of the channel to the northern ponded sediment basin.

Assessment of the High-Resolution Sediment Gravity Flow Record in Prince William Sound, Alaska.

CHAPTER 1: INTRODUCTION

Prince William Sound (PWS) is a deep glacially carved basin with a steep watershed traversed by glaciers and rivers amid the Chugach Mountains of south-central Alaska (Fig. 1). One of the most prominent sources of runoff and sediment is the rapidly retreating Columbia Glacier (CG; Fig. 1). PWS is connected to the Gulf of Alaska (GOA) through Hinchinbrook Inlet (HI). The Holocene sediments in HI contain seasonal layers corresponding to shelf-resuspension events during winter storms and the Copper River (CR) summer sediment plume (Marshall, 2015) which is advected into PWS by the Alaskan Coastal Current (ACC) (Wang et al., 2014). The glacial, riverine, and oceanographic conditions of south-central Alaska are in part controlled by the mountainous topography, which captures moist air masses, and are sensitive to global climate drivers (e.g., Pacific decadal oscillation, El Niño Southern Oscillation, Pacific/North America teleconnection, and Arctic Oscillation; Mantua et al., 1997; Neal et al., 2002; L'Heureux et al., 2004; Fleming and Whitfield, 2010; Barron and Anderson, 2011; Kaufman et al., 2011; Wendler et al., 2016). The PWS region also experiences frequent and strong earthquakes because it is located along the Aleutian Megathrust Boundary, where the Pacific Plate is subducting under the North American Plate (Wesson et al., 2007; Shennan et al., 2014; Haeussler et al., 2015; Mueller et al., 2015). It is the location of the second strongest earthquake ever recorded, the March 27, 1964 Great Alaskan ("Good Friday") Earthquake (M_w 9.2, USGS, 2016). PWS is therefore an ideal location to potentially contain a sedimentary record of both paleoseismic activity and regional/global paleoclimate.

In the deep central channel of PWS, approximately 100 m of sediment have been deposited within the last 4,000 years (Finn et al., 2015). In near surface sediments of this region the most distinctive deposits originate from episodic sediment gravity flows (Miller, 2014; Kuehl

et al., 2017), which are dense flows laden with sediments moving along the seabed under the action of gravity (Middleton and Hampton, 1973). The steep bathymetry of PWS allows sediment banks to accumulate which can readily undergo failure and generate gravity flows. Such accumulation may occur rapidly in regions receiving large sediment fluxes from the CG and CR. Source rocks in the Chugach Mountains (where the CG resides) are relatively high in K and Rb, while the CR drainage basin is comparatively higher in Sr and Ca. This leads to elevated K/Ca, Rb/Sr, and Rb/Ca ratios for local sediments from the CG region and minima associated with greater CR influence (Miller, 2014; Marshall, 2015; Kuehl et al., 2017). Thus, gravity flows from regions fed by the CG and the CR could mobilize large quantities of sediment with unique provenance signatures over long distances, distinguishing the deposits from locally emplaced sediment.

Bank failure and gravity flows can be triggered during energetic events such as earthquakes (Kuenen and Migliorini, 1950; Heezen and Ewing, 1952). Kuehl et al. (2017) used the unique provenance signatures from the PWS watershed and the CR to identify deposits associated with the 1964 earthquake, the 1899 Yakutat magnitude $M_w > 8.0$ earthquake, and three earthquakes of lower magnitudes, the smallest being M_w 6.4. Historically, the predominant method for studying the frequency of severe earthquakes in South-Central Alaska has been through investigation of terrestrial tsunami deposits and terraces uplifted above sea level during megathrust earthquakes ($M_w \geq 8.0$) (e.g., Plafker, 1969; Shennan et al., 2007; Carver and Plafker, 2008; Shennan et al., 2014). However, this record is limited to large ($M_w \geq 8.0$) earthquakes with proximal epicenters, thus the sensitivity of the marine sedimentary record to earthquakes both above and below M_w 8.0 offers a valuable tool for assessing the regional seismicity at a higher resolution. The marine sedimentary record also offers a valuable comparison with the terrace and

tsunami dating method. This has important implications for geohazard assessment and characterization of plate mechanics in the eastern Aleutian Megathrust Boundary.

Gravity flows and bank failure can also occur during glacial outburst floods (Mulder et al., 2003). Outburst floods occur when a glacially dammed lake breaks the ice dam or the water levels rise enough to float the dam (Walder and Costa, 1996) and may potentially occur due to earthquake-induced dam failure (Mulder et al., 2003). Such outburst floods can trigger a hyperpycnal flow, which results when fresh flood waters are denser than surrounding marine waters due to their sediment load and therefore flow along the seafloor (Mulder et al., 2003). Two lakes previously dammed by the CG, Terentiev and Kadin, underwent numerous draining and refilling cycles during recent glacial retreat until the levels became stable when they became undammed in 2000 (Krimmel, 2001). These rapid draining events may have occurred as outburst floods (Krimmel, 2001). The growth and retreat of glaciers is heavily controlled by local climate, which in south-central Alaska is in part dictated by large-scale global oscillations (e.g., Mantua et al., 1997; Neal et al., 2002; L'Heureux et al., 2004; Fleming and Whitfield, 2010; Barron and Anderson, 2011; Kaufman et al., 2011; Wendler et al., 2016). Thus the presence or absence of outburst activity over time in the sedimentary record may be dictated by the glacial terminus position and has the potential to serve as a proxy for local and global climate shifts. Furthermore, gravity flows from earthquakes and outburst floods may be distinguishable from each other in PWS, as earthquake deposits generally have an erosive base with a fining upwards grain size trend (Bouma, 1962), while hyperpycnal deposits may first coarsen upwards from the base before fining upwards, and may contain higher levels of terrestrial organic matter (Mulder et al., 2003; Zavala et al; 2012; Talling, 2014).

Previously, five cores were collected between HI and central PWS, and they contain distinct deposits related to the 1964 earthquake and events interpreted o be from earthquakes in 1983, 1928, 1912, and 1899 (Miller, 2014; Kuehl et al., 2017). This study collects six new gravity cores from central and northern PWS to complete a south-north transect through the central channel with the previous cores (Fig. 2) and capture a regional-scale overview of gravity flow activity and sedimentation trends. A few studies have assessed the sedimentation rates in northern PWS (e.g., Klein, 1983; Jaeger et al. 1998) but none have assessed the sediment provenance or gravity flow record. We seek to identify gravity flow deposits in northern PWS and correlate them with the southern cores using the established provenance ratios and to attempt to identify the deposits as turbidity currents or hyperpycnal flows by analyzing deposit grain size and organic signatures ($\delta^{13}C$ and $\delta^{15}N$). We also wish to determine the location within PWS capturing the most robust record of historic gravity flow activity (for future long-coring studies) and to fill a knowledge gap on the sedimentary record of an understudied, climatically sensitive region.

CHAPTER 2: BACKGROUND

2.1 Geologic Setting

The geology of the PWS region is composed of the Southern Margin Composite Terrane, which is subdivided into the Chugach Terrane in the north and west and the Prince William Terrane in the central and southeastern PWS (Fig. 3) (Moffit, 1954; Dumoulin, 1987; Winkler, 2000). Within the Chugach Terrane is the Late Mesozoic Valdez Group, containing primarily slates and phyllitic graywackes comprised of quartz, orthoclase and plagioclase feldspar, muscovite and chlorite (Sharma, 1979). South of the Chugach Terrane is the Prince William Terrane, predominately composed of the Orca Group deposited during the Paleocene-Eocene as a deep-sea fan complex along an uplifting continental margin (Moffit, 1954; Dumoulin, 1987;

Winkler, 1976, 2000). The Orca group makes up the basement rock of PWS (Finn et al., 2015), lies unconformably atop the Valdez group (Moffit, 1954), and is composed of sandstone, siltstone and mudstone with intermittent basaltic flows, breccia, and tuff (Dumoulin 1987; Winker, 1976, 2000). The Chugach Terrane began to build onto the North American continent during the early Mesozoic and continued in pulses through the late Cretaceous; the Prince William Terrane followed during the Eocene (Winkler, 2000).

2.2 Climatic Setting

The winter climate of Southern Alaska is primarily dictated by the Aleutian Low, a low-pressure system which influences sea surface temperature and pressure, circulation, ice cover, storms, etc. in the North Pacific (Overland et al. 1999; Rondionov et al., 2005; Hartmann and Wendler, 2005). The Aleutian Low varies on a decadal time scale (Overland et al., 1999) and is directly related to the North Pacific Index (NPI), the area-weighted sea-level pressure over the region 30°N-65°N, 160°E-140°W (Trenberth and Hurrell, 1994). The Aleutian Low and NPI are intrinsically related to the PDO, which is an inter-decadal climate pattern visible in sea surface temperature, sea level pressure, wintertime land surface air temperature, precipitation, streamflow and salmon landing records (e.g., Mantua et al., 1997; Neal et al., 2002; L'Heureux et al., 2004; Fleming and Whitfield, 2010; Barron and Anderson, 2011; Kaufman et al., 2011; Wendler et al., 2016). An intensified Aleutian Low occurs during a positive/warm PDO phase, increasing the advection of warm, moist air and hence storminess in southern Alaska during winters (Mantua et al., 1997 Hartman and Wendler, 2005). These storms can generate precipitation in excess of 300-800 cm/year along the southeastern Alaskan coast (Paulson et al., 1991; L'Heureux et al., 2004). During a negative/cold PDO phase, the Aleutian Low is weakened, and southern Alaska experiences fewer winter storms and less precipitation (Mantua et al., 1997 Hartman and Wendler, 2005). CR discharge is likely highly influenced by the PDO:

during warm PDO phases, monthly and seasonal streamflow increase during the winter due to increased rainfall, while cold PDO phases experience more winter snowfall and a larger meltwater discharge during the summer months (Neal et al., 2002).

2.3 Oceanographic Setting

PWS has a surface area spanning 8,400 km^2 and it contains a volume of 1,700 km^3 of water delivered by precipitation, snowmelt, glaciers and the GOA (Halverson et al., 2013). The tidal range within PWS is macro tidal and tidal amplitude varies between 4 to 6 m (Wang et al., 2013; Schoch and McCammon, 2013). Currents within PWS are dominated by tides (Vaughan et al., 2001) with typical velocities ranging from 0.3 - 0.5 m s^{-1} (Niebauer et al., 1994). The main connection between PWS and the GOA is HI, which is approximately 20 km long, 12-20 km wide, and 350 m deep (Fig. 2) (Halverson et al., 2013). The average depth of PWS is 200 m; however a deep (~425 m) central channel approximately 15 km wide spans from the CG region south to HI (Fig. 2 and 4) (Halverson et al., 2013).

Within the GOA is the Alaskan Coastal Current (ACC), which is a buoyant, density driven current that flows north and westward along the coast (Royer, 1979; Johnson et al., 1988). The strength of the current is controlled by down-welling favorable winds and freshwater discharge inputs. During the summer months when coastal winds are relatively low, the flow is weak. During the months of September to February when the Aleutian Low dominates, strong westward winds create a more robust ACC. The ACC carries roughly a third of the freshwater surface CR plume into PWS through HI in the summer according to the model of Wang et al., 2014. Of the portion of the CR plume entering PWS, the model indicates that two thirds eventually exit PWS through Montague Strait in the south (Wang et al., 2014). Seasonal influences from the ACC, tides, and winds set up an anticyclonic gyre in PWS from January to

April and a strong cyclonic gyre from September to December (Niebauer et al., 1994; Jin and Wang, 2004).

2.4 Prince William Sound Sedimentation

2.4.1 Copper River Sediments

Seismic profiles through HI and central PWS show foreset beds of Holocene sediment dipping into PWS, with a maximum thickness around 200 m (CS4, Fig. 5) (Carlson and Molnia, 1978; Stocks, 1996; Liberty and Finn, 2013; Finn et al., 2015). Clay mineralogy (Naidu et al., 1976; Molnia and Hein, 1982; Klein, 1983; Stocks, 1996) and satellite images (Feely et al., 1979) indicate that some of these sediments are likely derived from the CR plume. The sedimentation rate in HI cores PWS-07 and PWS-08 (Fig. 6 and 7) are 4.4 ± 0.5 cm yr^{-1} and 4.0 ± 0.4 cm yr^{-1} respectively, and X-ray fluorescence (XRF) core scans show cyclic variations in the Sr/Pb ratio (Miller, 2014; Kuehl et al., 2017). High Sr/Pb indicates coarser sediment and dominance of CR inputs while a low Sr/Pb ratio indicates finer sediments and/or dominance of local PWS inputs. This serves as a proxy for changes in seasonal CR sedimentation: Coarser (high Sr/Pb) grained bands represent shelf sediment from the Gulf (derived from the CUR) resuspended by winter storms, and fine (low Sr/Pb) grained bands represent local sediments accumulated during the calmer summer months (Miller, 2014; Kuehl et al., 2017).

Marshall (2015) conducted an analysis of the 18-year record of waves in HI and concluded that winter storms frequently generate waves with bottom orbital velocities in excess of 0.19 m/s, sufficiently high to resuspend continental shelf sediments. The seasonal nature of the wave climate helps explain the banding observed in southern cores PWS-07 and PWS-08, with some larger events potentially impacting PWS-09 (Fig. 8). In HI, winter storm resuspension deposits account for 65% of the 200 m thick Holocene sediment deposit and are predominantly sourced from the shelf and originally sourced from the CR basin (Marshall, 2015). The CR

drainage basin rocks are relatively high in copper content, thus high ratios of Cu/Pb, along with aforementioned Sr/Pb, serve as proxies for CR sediment (Kuehl et al., 2017). Summer sediments show both CR and local PWS sources, however local sources dominate as local discharge within PWS is higher in the summer than in winter and there is decreased shelf resuspension of CR sediments (Marshall, 2015; Kuehl et al., 2017).

2.4.2 Local PWS Sediments

Moving north from HI into PWS along the central channel, sedimentation rates decrease towards the center of PWS to 0.24-1.1 cm yr^{-1} (Klein, 1983; Miller, 2014). From central PWS north toward the CG, the sedimentation rates increase to 0.57-1.3 cm yr^{-1} (Klein, 1983; Miller, 2014). The initial decrease in sedimentation rate moving away from HI is likely due to decreasing delivery of the CR sediment plume and shelf resuspension, while the increase moving northward from the center of PWS is likely due to increasing delivery from the CG.

The central channel of PWS contains Holocene sediments spanning ~4,000 years down to a neoglacial unconformity (Fig. 5; Finn et al., 2015). There are also two deep (>450m depth) basins (Fig. 4), herein referred to as the northern and southern ponded sediment basins (Fig. 4). Based on seismic reflection data, a unit of highly reflective ponded sediments in the northern basin and has been interpreted as CG sediments / outburst flood deposits (Fig. 5; Stocks, 1996; Finn et al., 2015). Clay mineral abundances in these sediments are 40% illite and 60% kaolinite/chlorite, which is indicative of a CG source (Klein, 1983). Based on seismic reflector continuity to a dated sediment core in southern PWS (EW0408-98JC, IMLGS, 2004), the upper 40 m of the northern ponded sediment basin is estimated to be underlain by Little Ice Age (LIA) sediments which are only 300 years old (Finn et al., 2015). This implies all 40 m have accumulated since the LIA and that rates of deposition are much higher (i.e., average >13 cm yr^{-1}) than the surrounding region. The flat sea bed and horizontal, parallel internal layering of the

northern ponded sediment basin suggests deposition by regular sediment gravity flows (Syvitski, 1989).

2.5 Earthquakes and Turbidites

2.5.1 Subduction Earthquakes

Southern Alaska lies along the Aleutian Megathrust boundary (AMB), which is one of the three most tectonically active regions in the world (Ryan et al., 2011). Megathrust plate boundaries are regions where tectonic plates are actively subducting and are characterized by earthquake hypocenters along the interface between the subducting plate and the overriding plate. Convergent boundaries along continental margins such as the AMB, where less dense continental crust overrides denser oceanic crust, subduct at shallow angles resulting in high coupling of the plates and severe earthquakes (Condie, 1997). The AMB spans 3,000 km starting around Middleton Island in the GOA and stretches east, boasting at least 29 active volcanoes (Ryan et al., 2011). The offshore trench is 5 to 6 km deep, and the Pacific plate is subducting at a rate of 54-76 mm yr^{-1} (Ryan et al., 2001). The region has been tectonically active since the Late Jurassic or Early Cretaceous, but the most recent orogeny began in the Pliocene, 5.3 mya (Plafker, 1969).

Historical records (USGS, 2016) of earthquakes in Alaska are fragmented and incomplete prior to the 20th century. The earliest instrumentally recorded earthquake within PWS was a magnitude (M_w) 7.0 in 1912. The epicenter was either located northwest of CG (Engdahl and Villaseñor, 2002), or 32 km southwest of CG as recalculated by Doser et al. (2006) (Fig 9). USGS online records span back to 1925 and inventory several earthquakes of significant magnitude ($M_w > 6.0$) within PWS, the largest being the 1964 Great Alaskan Earthquake of M_w 9.2. In 1899, an earthquake of $M_w > 8.0$ occurred over 300 km east of PWS near Yakutat.

Witness observations confirmed earthshaking and tsunamis generated by slope failures in Valdez from this event (Lander, 1996).

2.5.2 Recurrence Intervals

Classically, earthquake source zones are characterized by a recurrence interval, which is the average amount of time between earthquakes of similar magnitude. In PWS, paleoseismic studies have utilized well-preserved Holocene marine terraces that were uplifted during great earthquakes ($M_w > 8.0$) (Plafker, 1969; Plafker et al., 1992; Plafker and Rubin, 1978; Shennan and Hamilton, 2006; Shennan et al., 2007; Carver and Plafker, 2008) and tsunami deposits (e.g., Ryan et al., 2011; Shennan et al., 2014) to estimate recurrence intervals. Radiocarbon dating of organic material on the terraces allows a minimum age to be assigned to the uplift event, and by comparing multiple events and dates it is possible to estimate the average time between great earthquakes. In the CR delta-PWS region, the recurrence interval has been estimated at between 600 and 950 years (Plafker et al., 1992). The time elapsed between the 1964 and penultimate earthquake has been determined as 833 ± 34 years, and roughly 420 to 610 years between older earthquakes in PWS region (Shennan et al., 2014). This method limits recurrence interval estimates to only the greatest magnitude earthquakes in the region accompanied by many meters of uplift/subsidence ($M_w>8.0$).

2.5.3 Turbidity Currents

Great earthquakes can generate sediment gravity flows, which are density flows laden with sediments moving along the seabed under the action of gravity (Middleton and Hampton, 1973). Gravity flows triggered by earthquakes commonly take the form of surge-induced turbidity currents, which occur when an underwater bed of sediments undergoes slope failure during the shaking (Kuenen and Migliorini, 1950; Heezen and Ewing, 1952). Once in motion, turbidity currents transport large quantities of sediment downslope over long distances and can

be highly erosive. When a surge-induced turbidity current initiates, the density is close to that of the in situ sediments at the failure location (1300-1700 kg m^{-3}); as water is entrained, the density and concentration rapidly decreases, yet the current can continue to move downslope even with low particle concentrations due to the increase of density through salt water entrainment (Mulder et al., 2003). The concentration gradient across a turbidity current from top to bottom is strong, so the base and top may behave differently (Stacey and Bowen, 1988; Kneller and Buckee, 2000; Mulder et al., 2003). Based on field observations, laboratory experiments, and models, surge-induced turbidity currents typically have velocities greater than 4 m s^{-1}, can occasionally travel on the order of 30-40 m s^{-1} (Mulder et al., 1997; Piper and Savoye, 1993, Mulder et al., 2003), and accelerate to peak velocity rapidly after initiation (Mulder et al., 2003). Surge turbidity currents are unsteady flows, meaning the flows accelerate and decelerate abruptly, and they tend to be short lived events lasting on the order of minutes to hours (Mulder et al., 2003).

Dependent on the sea floor slope, the availability of erodible sediments, and flow velocity, turbidity currents can be classified into one of three different regimes described by Chen et al. (2013): decelerating, autosuspending, and accelerating. The accelerating regime occurs on steep slopes where there is stronger gravitational forcing on a flow's velocity. This results in more turbulence along the bottom boundary, which generates upward lift to counteract the settling of suspended particles. If there is an erodible bed and enough turbulence, entrainment of additional sediment will cause the flow to gain velocity as it becomes denser and thus has greater gravitational forcing downslope. If the flow depletes all the readily erodible sediments (Pantini, 2001), and/or after other external forces (e.g., moving upslope) slow it down, it can enter the autosuspending regime (Bagnold, 1962). Autosuspending flows travel at a relatively constant velocity in steady state, while upward turbulent lift exceeds particle settling. Flows

traveling on gentle slopes experience less gravitational forcing and may not generate enough upward turbulent lift to counteract particle settling. As they lose suspended sediment, they become less dense and decelerate. This is known as the decelerating regime, and such flows tend to be short lived, have short runout distances (the maximum distance the flow travels before stopping), and deposit most of their mass as bedload along the flow's main path (Chen et al., 2013).

2.5.4 Turbidites

Sedimentary sequences deposited by turbidity currents are known as turbidites (Kuenen, 1957) and their grain size, erosional, and structural pattern is classically known as the Bouma sequence (Bouma, 1962). The Bouma sequence is composed of an erosive base with coarse grain sediments, such as medium to fine sand, and a fining upwards in grain size into a gradational top contact (Fig. 10). Structures which may be present in turbidites include ripple, cross, parallel and convolute laminations (Bouma, 1962). Turbidites have been recognized as volumetrically the most important clastic accumulations in the deep sea (Normark et al., 1993). Mud turbidites in particular make up a higher portion of material flux to the deep sea than sandy turbidites (Goldfinger et al., 2013). They are common structures in submarine fans at the mouths of submarine canyons.

Turbidites have been used as a proxy for great ($M_w > 8.0$) earthquake paleoseismicity (e.g., Noda et al., 2008; Goldfinger et al., 2003a, 2003b, 2012, 2013), and successfully dating earthquakes down to M_w 7.0 (Goldfinger et al., 2013). Instrumental records of earthquakes span a few centuries globally, encompassing only part of regional seismic cycles. To test concepts such as the seismic-gap hypothesis, clustering, and recurrence models requires longer records spanning multiple seismic intervals (Goldfinger et al., 2012). Sediment gravity flows can occur

during seismic activity without the extensive uplift required to generate terraces, offering a high-resolution seismic record. However, it must be determined that the parent turbidity current was generated by an earthquake and not by local activities capable of triggering slope failure, such as storm waves or rapid sedimentation upslope (Noda et al., 2008). There are two ways to test if a turbidite was deposited by an earthquake (region-wide slope failure) and not other triggers: synchronous emplacement and confluence (Talling, 2014).

Synchronous emplacement is tested by taking multiple widespread cores in an attempt to capture the entire local seismic event record and dating sediment layers in the cores just above and below each turbidite (Talling, 2014). If the same age bracket turbidites are deposited in numerous cores from different basins, it implies generation by regionally widespread slope-failure events. To test confluence, the number of turbidites deposited in a channel or basin is counted and compared to the number deposited in a tributary flowing into the channel/basin (Talling, 2014). If the numbers are the same on the upstream and downstream side of a confluence, this also indicates synchronous wide-spread emplacement. This method supports generation by a very wide-spread event, such as a large earthquake, and can help rule out other triggers which can generate synchronous turbidity currents on smaller scales, such as hurricane winds (Talling, 2014).

However, there are some complications with these two tests. Widespread slope failure can lead to synchronous turbidite deposits with different compositions, complicating correlation of deposits. Additionally, erosion at the base of a turbidite can complicate dating and thus if events were synchronous (Talling, 2014). During confluence tests, the number of detected turbidites within a channel/basin core is highly dependent on slope (Talling, 2014). A sloped location along the channel side may not capture deposits from every current as well as a location

on the channel floor. Both tests can be convoluted by the fact that slope failure (and thus turbidite generation) during an earthquake also depends on sedimentation rates and slope stability (Noda et al., 2008), thus a true earthquake turbidite may still not appear in all cores. Lastly, not all major earthquakes deposit extensive turbidites, as was the case with the 2004 and 2005 Sumatran and 2010 Chilean earthquakes (all M_w>8.5), which results in an underrepresented paleoseismic sedimentary record (Talling, 2014).

The bathymetry of PWS is characterized by steep slopes and deep channels, thus seismic events have been able to consistently generate turbidity currents. Cores PWS-10 and PWS-12, contain records of turbidites associated with events in 1983, 1964, 1928, 1912 and 1899 (Miller, 2015; Kuehl et al., 2017). These are marked by shifts in the CG and CR provenance ratios. The 1983, 1964, and 1912 events are correlated with earthquakes with epicenters near the CG. The 1928 deposit is correlated with an earthquake in the central (USGS, 2016) or southern PWS (epicenter recalculated by Doser et al., 2001), and the 1899 deposit with slippage from the Yakutat great earthquakes near the CR (Kuehl et al., 2017). PWS-09 (Fig. 8; Miller, 2014) also contains a turbidite from 1964 at 70 - 80 cm with an increase from < 10% to > 60% sand, minimas in K/Ca and Rb/Sr and a maxima in Sr/Pb.

2.6 Columbia Glacier

2.6.1 The Glacier

The CG is a tidewater glacier sourced from the Chugach mountain range which terminates in Columbia Fjord on the northern edge of PWS (Fig. 11). Glaciers form as snow high in the mountains is continually packed down into ice with less annual melt than accumulation. Tidewater glaciers terminate directly into a marine body of water and their bases rest on the seabed instead of floating. The portion of the glacier grounded below sea level is called the marine-based reach. The CG margin was growing around 1020 CE, slowed growth in the 1450s

to late 1700s, and then accelerated to its maximum reach in 1810 (Beckwith-Laube et al., 2004; Barclay et al., 2009). This stable terminus was located on a combination of a submerged moraine shoal and Heather island, located near the mouth of Columbia Bay.

In 1978 rapid retreat began due to surface lowering, causing the CG to recede from Heather Island, and it completely retreated from the shoal in 1983 (Meier et al., 1985). Since this period the glacier has been experiencing ongoing rapid retreat driven by calving in ~300 m deep water and increases in subglacial runoff (Brown et al., 1982; Sikonia, 1982). The retreat rate accelerated until the early 1990s, slowed for two periods from 1994-1997 and 2000-2006, and has since accelerated through present (O'Neel et al., 2005). These shifts in retreat rate were driven by retreat over a deep subglacial basin and the subsequent steepening of the glacier surface (Boldt et al., 2016).

CG has retreated 23 km at an average rate of 0.7 km yr^{-1} since the onset of retreat in the early 1980s (Boldt et al., 2016). As of 2015 it spanned 944 km^2 of area and was receding at a rate of 0.519 km yr^{-1} (McNabb et al., 2015). It has lost over 50% of the volume it had in 1957 and has separated into two dynamically distinct branches known as the west branch and the main branch (Krimmel, 2001; O'Neel et al., 2005; Rasmussen et al., 2011; McNabb et al., 2012).

The glacier is a prominent source of sediment to the northern regions of PWS. The average sedimentation rate within the fjord over the whole retreat period is 5 cm yr^{-1} (Boldt et al., 2016) and the rate beyond the terminus over the past 100 years is estimated as 0.2 cm yr^{-1} (Jaeger et al., 1998). Within Columbia Bay there is low uniform ^{210}Pb activity around 1.1 ± 0.2 DPM g^{-1} with little to no excess ^{210}Pb (Boldt et al., 2016). Low excess lead indicates that the sediment particles were unable to scavenge lead (i.e. cohesion of ^{210}Pb in the water column to sediment particles) during deposition. This could be due to high settling rates from buoyant

surface plumes not allowing adequate time for lead scavenging (e.g., Jaeger and Nittrouer, 1999; Kuehl et al., 1986), which is supported by the ^{234}Th estimated sedimentation rates of ~0.4 cm day^{-1} during the melting season (Boldt, 2014).

It is also possible that sediment was delivered without settling through the water column (e.g., Mullenbach and Nittrouer, 2000), possibly by sediment gravity flows along the bottom. Within Columbia Bay there are horizontal parallel layers of sediment on the order of tens of meters thick (Boldt et al., 2014; 2016). The thickness of subglacial sediment packages pre-retreat, as determined from boreholes through the glacier, were on the order of decimeters (Humphrey et al., 1993). By comparing this to the thickness of the modern layers in the Bay, Boldt et al., 2016, determined it most likely these layers were emplaced by sediment gravity flows during the most recent retreat. Such flows typically play a large role in sediment transport in temperate fjords (such as Columbia Bay) and leave parallel laminations (Syvitski, 1989). Other redistribution processes such as slumping, iceberg gouging and melting, waves generated by calving, and deep tidal currents have likely also contributed to the formation of these layers (Boldt et al., 2016).

It is also possible that early in the retreat large quantities of sediment were delivered beyond the terminal moraine into PWS. From 1982-1995 annual sediment flux was estimated as 3 million m^3 yr^{-1}, and while the terminus was still within 2 km of the moraine it is approximated that 15% (50 million m^3) of the total that sediment flux crossed the moraine into PWS (Boldt et al., 2016). Thus, there may be a record of changing glacial activity captured in the sediments of northern PWS.

2.6.2 Glacial Outburst Floods

Glacial outburst floods occur when subglacial water or a lake dammed by a glacier rapidly drains. The dams may also be a moraine composed of till and ice pushed up by the glacier. Glacial ice dams can be broken by earthquakes (Mulder et al., 2003) and floated when the lake water levels become sufficiently deep (Walder and Costa, 1996). Further possible causes of dam break and erosion include water pressure, turbidity currents, and overfilling, such as occurred at Hubbard Glacier in Russell Fjord in 1986 and 2002 (Mayo, 1989; Trabant et al., 2003). One of the most famous outbursts occurred in Iceland at the Vatnajokull ice cap when the Grímsvötn volcano erupted beneath the ice in 1996 (Gudmundsson et al., 1997). The flood waters will drain through subglacial conduits, transporting large volumes of glacial sediment.

Two lakes were historically dammed by the CG: Terentiev and Kadin (Fig. 11). Lake Kadin (and presumably Terentiev) was fed partially by direct glacier melt and by precipitation from an off-glacier drainage basin (Meier et al., 1994). There are sparse records of lake water levels prior to 1976, but given the stability of the glacier during this period it is presumed that they remained stable or periodically underwent outbursts (Krimmel, 2001). Between 1976 and 2000, the average lake water levels decreased about 8.5 m per year. This rate is similar to the ice ablation rate during this period, suggesting that ice thickness controlled the lake levels (Krimmel, 2001). Terentiev's levels stabilized in 1992 at 13m depth, and Kadin reached 15 m depths in 2000, even though ice still dammed its outlet at the time. Currently the lakes are completely undammed and therefore no longer produce outburst floods (Fig. 11, personal communication with R. Krimmel, 2017).

During the rapid retreat of CG the lakes underwent many draining and refilling cycles (Fig. 11). Refilling of the lakes between outburst events occurred periodically during

precipitation and wind-driven glacier melting events (Meier et al., 1994). Lake Terentiev underwent water level drops on the order of 80 m in 1986 and 1989. Lake Kadin experienced lake level drops on the order of 90 m during 1982, 1986, 1990, 1993, and 1995, followed by two smaller events on the order of 50 m in 1997 and 2000. Lake Kadin outflow was either zero or very low under normal conditions (Stone, 1988), indicating that decreases in water level occurred entirely during large events. These events were likely subglacial outbursts which lasted on the order of hours to days, as there was never observed evidence of supraglacial flow (personal communication from R. Krimmel, 2017).

Another type of outburst flood may have been triggered by rapid evacuation of a subglacial reservoir of sediment and water during the early stages of retreat. Thinner regions of the glacier have less pressure at the base and are frozen, while areas under thicker portions (greater pressure) induce basal melting and allow water to flow (Rothlisberger, 1972). When the base of a glacier is frozen, water and sediment in the subglacial system are trapped and rapidly accumulate in a subglacial reservoir, raising the reservoir and glacier base over time until the bed slope is sufficient to allow melting and an outburst flood occurs as the reservoir empties (Alley et al., 2003). Boldt et al. (2016) discovered that this phenomenon occurred two times during the retreat of CG, both as the terminus retreated over sills between subglacial basins. When the terminus reached the reverse slopes on the northern sides of the sills, the retreat slowed as the terminus ice was thinner and allowed basal freezing. Water and sediment gradually pooled in the up-glacier basin, raising the basal surface until the reservoirs rapidly emptied via gravity flows. While the terminus of CG was pinned on the moraine early in retreat, the ice was substantially thinner than portions up-glacier as it resided on a reverse slope (Boldt et al., 2016; McNabb et

al., 2012). Thus, a similar phenomenon could have occurred in the early 1980s as the terminus retreated over the reverse slope on the northern side of the terminal moraine.

2.6.3 Hyperpycnal Flows

Outburst floods entering marine waters may result in a type of gravity flow known as a hyperpycnal flow. Hyperpycnal flows are negatively buoyant freshwater flows that move along the seafloor due to having greater density than the ambient water from the suspended particle load they carry (Mulder and Syvitski, 1995). Hyperpycnal flows are generated when large quantities of sediment-laden freshwater (concentrations in excess of 36 - 43 g L^{-1}) empty into a standing body of marine water, usually during an event such as a river flood, dam erosion, or glacial outburst flood (Mulder and Syvitski, 1995). They can also be generated by settling due to convective fingering in sediment plumes with concentrations as low as 1 g L^{-1} (Mulder et al., 2003). In Columbia Bay, concentrations in excess of ~30 g L^{-1} exceed the density of the ambient fjord seawater (Boldt et al., 2016).

Hyperpycnal flows are characterized by their suspended sediment load and their freshwater content (Mulder et al., 2003). These flows move on the order of < 2 m s^{-1}, do not carry a bed load, and can persist for minutes to weeks (Mulder and Syvitski, 1995; Mulder et al., 2003). They are composed of three semi-distinct regions: the plunging point, the main body, and the leading head. The plunging point is the location where the surface floating stream flow ends and the underflow or density current begins (Singh and Shah, 1971). When rapid flowing freshwater meets relatively static reservoir water, the flow momentum creates a pressure gradient between the bodies of water. Together with friction and slope of the seabed, the plunging point develops as the bottom moving portion of the flow pushes out before the surface portion of the flow. Eventually the surface portion plunges to join the newly formed main body (Singh and Shah, 1971). The main body is in balance between gravity, entrainment, seabed and internal

friction, and sedimentation rate (Siegenthaler and Buhler, 1985), and is responsible for any sustained scour and deposition on the seafloor (Kassem and Imran, 2001). Mixing in the leading head dictates how far a flow can travel before losing its identity (Kassem and Imran, 2001). The flows are maintained as entrainment of sea-water increases the density of the water and dilutes the suspended sediments, decreasing internal friction; and as erosion of the sea floor increases the flow density (Mulder et al., 1998).

Hyperpycnal flows can be autosuspensional, but in gentle slope conditions they are decelerating and primarily supported through wave- or current-induced velocity shear (Wright and Friedrichs, 2006). Hyperpycnal flows have weaker gravitational forcing compared to turbidity currents due to lower densities and hence move too slowly to be highly erosive (Mulder et al., 2003). Travel via accelerating regime may be possible if there are readily erodible mud beds (Chen et al., 2013).

2.6.4 Hyperpycnites

Hyperpycnal flows deposit recognizable layers called hyperpycnites. Mulder et al. (2003) developed a model of hyperpycnite structure where they are composed of two units: an upper and a lower. The lower unit displays a coarsening upwards sequence (inverse grading), which is deposited by three different mechanisms: incorporation of mud clasts at the base, freezing of successive laminar boundary layers, and a steady waxing flow discharge over time (Fig. 10). The upper unit is a classical fining-upwards sequence deposited by the waning flow. The contact between these two units may be erosive if peak discharge was large enough to prevent sedimentation and to erode the recently deposited particles (Mulder et al., 2001). Hyperpycnites may also contain climbing ripples (Migeon et al., 2001; Mutti et al., 2003), laminae representing hydrodynamic fluctuation in the bottom boundary layer (Hess and Chough, 1980), and terrestrial

flora/fauna material (Mulder et al., 2003, Zavala et al., 2012). According to this model, hyperpycnal flows generated by a rapid surge in freshwater, such as an outburst flood, leave hyperpycnites that may lack the lower unit and appear turbidite-like with a highly erosive base and fining-upwards unit.

Another model proposed by Talling (2014) claims that hyperpycnal flows move on the order of < 50 cm s^{-1}, are dilute (< 0.01 vol.% sediment) and leave behind deposits similar to that seen in freshwater lake and reservoir hyperpycnal flows: mm to 2-10 cm thick fine grained deposits. Fine sand may be present but the hyperpycnites are mainly mud and may be rich in organic matter. The thin nature of the deposit is due to dilute sediment concentrations and slow aggradation rates during the flows, and there is little or no erosion. There may be inverse grading, but variations in grading and flow can produce complex gradational patters.

Talling (2014) supports that grain size patterns, terrestrial organic matter, compositional changes, and thickness/pinching are helpful tools to identifying hyperpycnites from other deposits. However, Talling (2014) cautions against using these as the only diagnostic tools in any model due to the complex nature of the formation of these different signals. For example changes in grading may be due to more than simply flow velocity; there could be changes in flow concentration. Turbidites can also have similar grain size and terrestrial organic content as a hyperpycnite if the sediment bank that failed was loaded with sediments derived from a continental freshwater source. Dating a deposit and comparing the age with the dates of known floods is another way to identify hyperpycnites. However, if the deposit date is not well constrained, or if historical trigger events occurred close in time, it can be hard to correlate the dates. By counting the number of hyperpycnal deposits between two well-dated horizons (e.g., the 1964 earthquake deposit and the core-top) the frequency of the flows can be estimated.

Problems with this method arise due to assumptions regarding the regularity of flow occurrence and the successful representation of every flow at the coring site.

Both of these models indicate that hyperpycnites may be rich in organic matter and may contain inverse grading with no erosional base. This contrasts with the theoretical structure of a turbidite, which has an erosional coarse base that fines upwards and may not be rich in organic matter.

CHAPTER 3: METHODS

3.1 Core Collection

The six new sediment cores analyzed for this study were collected July 20 – 24 2016 onboard the *R/V Auklet*. Cores were collected with a gravity corer using 2-m polycarbonate tubes with 9.5 cm inner diameters and saw-tooth design core catchers. The cores were collected in a south-to-north transect in the central channel of PWS spanning from central PWS to the mouth of Columbia Bay (Fig. 2; refer to Table 1 for coordinates). Gravity cores were not recovered in the northern ponded sediments basin with the corer used in this study. Coring equipment was deployed multiple times at three separate locations within the basin, and for each attempt the equipment returned covered with streaks of mud, indicating that penetration had occurred but the core catcher was unable to retain the sediment. This suggests the northern ponded sediment basin contains highly unconsolidated surface sediments.

3.2 Core Processing

Split cores were subsampled at 1 cm resolution. The wet samples were weighed and dried at ~80°C for the analysis of water content. The dried samples were then ground and stored in 7 ml borosilicate glass vials to be used for $\delta^{13}C$ and $\delta^{15}N$ analyses. The remaining dry sediment was composited in 3 cm intervals and tightly packed into 70 ml petri dishes for gamma spectroscopy. The photographs and X-radiographs were analyzed for fine sediment structures.

The X-radiography shows differences in sediment density which can often be correlated with changes in grain size, ripple structures, and erosional/depositional contacts. Regions of interest in the cores as indicated by the photographs, X-radiographs and the XRF elemental ratios (see section 3.4) were subsampled as necessary from the remaining core halves at higher resolution for grain size and $\delta^{13}C$ and $\delta^{15}N$ analyses.

3.3 Geochronology – Radioactive Isotope Analyses

3.3.1 ^{210}Pb Dating

Sediment age dating was performed using ^{210}Pb, a naturally occurring radioactive isotope with a half-life ($t_{1/2}$) of 22.3 years. As part of the ^{238}U decay series, there are two mechanisms by which ^{210}Pb is supplied to sediments: atmospheric fallout produced by the decay of ^{222}Rn (unsupported or excess) and in situ decay of ^{226}Ra (supported; Krishnaswamy et al., 1971; Nittrouer et al., 1979). Excess ^{210}Pb adsorbs onto particles in the water column and accretes in the seabed. Over time, the quantity of excess lead in the seabed decays until only in situ supported quantities remain. Using the Constant Flux Constant Sedimentation Rate model (CF:CS), the activity of excess and supported lead present at core-top (C_0) and the background supported levels at depth z (C_z) are used to determine the rate of sedimentation S. Using the decay constant λ for ^{210}Pb (0.0311 yr^{-1}), S is calculated using equation 1 (Nittrouer, 1984):

$$S = \frac{\lambda z}{\ln\left(\frac{C_0}{C_z}\right)} \quad (1)$$

This equation assumes a steady sediment flux and negligible mixing in the region of steady decay. After completing a linear regression of ln(excess ^{210}Pb) versus depth, equation 1 can be rearranged into equation 2 to determine the sedimentation rate (S):

$$S = -\frac{\lambda}{m} \quad (2)$$

where m is the slope of the linear regression line. This is also known as the linear sediment accumulation rate (LAR). The age of a layer can then be estimated as a function of distance downcore using the LAR.

The activities of ^{210}Pb were directly measured via gamma ray spectroscopy at VIMS. The petri dishes were then sealed with electrical tape, and left to sit for at least three weeks to allow the ^{214}Pb and ^{214}Bi daughters to achieve secular equilibrium. The samples were counted with Canberra germanium detectors for 24 hours to measure gamma radiation. The detector counts were recorded using Genie^{TM} and ORTEC® MAESTRO® spectroscopy software, corrected for detector background readings, and converted to units of decays per minute per gram (DPM g^{-1}). During ^{210}Pb decay, a beta particle (electron) is released from the nucleus with a gamma ray of energy 46.5 keV, allowing for measurement of total ^{210}Pb radioactivity. The supported lead levels were measured using the average radioactivity of in-situ parent isotopes ^{214}Pb at 295 keV and 352 keV, and ^{214}Bi at 609 keV. Excess ^{210}Pb activity is then calculated as the total activity minus the supported activity. An attenuation factor (A) to correct for self-sample attenuation was calculated using equation 3 (Cutshall et al., 1983):

$$A = \frac{\ln\left(\frac{T}{I}\right)}{\left(\frac{T}{I}\right)-1} \quad (3)$$

T is the attenuated beam intensity determined by counting samples with a ^{210}Pb source on top for 300 s and subtracting the intensity of the ^{210}Pb generated from within the sample. *I* is the unattenuated beam intensity of the ^{210}Pb source counted on top of an empty petri dish for 300 s. The attenuation factor was multiplied by the raw counts per minute value from the detector activity reading at 46.5 keV before conversion to DPM g^{-1}.

3.3.2 ^{137}Cs and ^{239,240}Pu Dating

The ^{210}Pb sedimentation rates were compared sedimentation rates obtained from ^{137}Cs ($t_{1/2}$ = 30.17 y) and ^{239,240}Pu ($t_{1/2}$ = 24,100 and 6,561 y, respectively) geochronology. Both isotopes were anthropogenically introduced by atmospheric fallout during nuclear weapon testing, which began in 1954 and had a global peak in 1963. Combined, these isotopes can be used to quantify sedimentation rates within the last century. The ^{137}Cs emissions at 661 keV in each sample were measured using Canberra germanium detectors at VIMS over a 24 hour period. The activities were calculated in decays per minute per gram (DPM g^{-1}) and plotted downcore to locate the 1963 peak and 1954 first appearance.

The combined amount of $^{239+240}$Pu isotopes present was determined through chemical separation (at VIMS) and measurement on a Thermo X Series II quadrupole inductively coupled mass spectrometer (ICP-MS) at the University of Northern Arizona based on the procedures of (Ketterer et al., 2002; Ketterer et al., 2004). Briefly, dried sediment samples (3-4 g) were ashed at 600 °C for 8 hours to remove organic material, then mixed with 20 mL of trace metal grade HNO_3 and underwent microwave digestion. The mixture was vortexed, and the supernatant was decanted into borosilicate vials and evaporated to incipient dryness. Then 3 mL of 8 M HNO_3 (Nitric Acid) and 0.5 mL of $NaNO_2$ (Sodium Nitrate) were added to convert all Pu to Pu (IV). EIChrom UTEVA resin columns were conditioned with 2mL of 8M HNO_3 containing 0.3% H_2O_2 (Hydrogen Peroxide), then the aqueous solution was passed through the column. Pu was eluted from the column by conversion from Pu (IV) to PU (III) with 2 mL of 2 M HNO_3 containing 0.02M $NH_2OH.HCL$ (Hydroxylannonium Chloride) and 0.02M $C_6H_8O_6$ (Ascorbic Acid). Samples were evaporated to incipient dryness and brought to 10 mL with 2% HNO_3 for direct ICP-MS analyses.

Both ^{137}Cs and $^{239+240}Pu$ have been used as an independent check on ^{210}Pb derived sedimentation rates (e.g., Krishnaswamy et al., 1971; Nittrouer et al., 1984; Kuehl et al., 1986; Kuehl et al., 2012). The Pu isotopes' longer half-lives make them useful in modern sediment dating as ^{137}Cs activity approaches the limit of detection because two half-lives have passed since peak global deposition in 1963. The distance downcore to the 1963 peak or the first appearance in 1954 of ^{137}Cs and $^{239+240}Pu$ divided by the number of years elapsed yields a constant sedimentation rate for comparison to the ^{210}Pb calculated sedimentation rate (Nittrouer et al., 1984).

3.4 Elemental Analysis - X-Ray Fluorescence

Core scanning X-Ray Fluorescence (XRF) was performed to determine relative downcore elemental ratios. XRF scans were conducted at the University of Minnesota's Large Lakes Observatory using the ITRAX XRF Core-scanner. The core-scanner X-radiographed the cores at 60 keV/50mA (voltage/current), then radiated the cores with 30 keV/55mA energy X-rays generated from a 3kW Mo X-ray tube and sampled at 0.5 cm resolution with a dwell time of 20 s. The scans measured most elements from Al to U, but this study focuses on K, Ca, Cu, Rb, and Sr. Downcore elemental profiles were aligned and compared to assess relative elemental ratios between cores.

3.5 Grain Size - Laser Diffraction

Subsamples from the newly collected cores PWS-(17-28) were analyzed via laser diffraction at Texas A&M University to assess grain size fluctuations downcore. Samples were mixed with a sodium hexametaphosphate as a dispersant, and directly analyzed on a Malvern Mastersizer 2000 with HydroG dispersion unit under constant sonication. Each sample was measured in triplicate, and reported values are an average of those results. High resolution

subsampling intervals of 1 cm and 0.5 cm were taken in layers of interest as indicated by changes in XRF ratios, visual color, and X-radiography. The remaining 'background' areas of each core were taken in 1 cm increments every 10 cm downcore.

3.6 Stable Isotopes ^{13}C and ^{15}N – Isotope Ratio Mass Spectrometry

The stable carbon ($\delta^{13}C$), nitrogen ($\delta^{15}N$), and C/N ratios were measured to help identify varying signatures of terrestrial versus marine organic sources of C and N in the sediment samples. The predominant plant types present in the Copper River Delta are C-3 marsh plants (Boggs, 2000). C-3 plants have higher ^{12}C content, resulting in $\delta^{13}C$ values in the range of -23 to -30 ‰, while marine phytoplankton (-18 to -24 ‰) and other sources such as C-4 salt marsh plants and benthic macroalgae (-12 to -18 ‰) are more enriched (higher values) (Cloern, et al., 2002; Bianchi, 2007; Bianchi and Canuel, 2011). Nitrogen isotopes can also have lower terrestrial signatures (vascular plants, soils, C-3 plants; -2 to +6.4 ‰) than marine sources (phytoplankton, C-4 plants, benthic microalgae; 0 to 9 ‰) (Bianchi, 2007; Bianchi and Canuel, 2011). Vascular terrestrial plants tend to have higher carbon content due to higher amounts of cellulose and lignin, while marine microalgae and microbes have higher nitrogen content from higher amounts of amino acid proteins. Thus a higher C/N ratio (>15) can indicate a greater terrestrial organic carbon content, while lower ratios (~5-10) indicate marine dominated organic carbon (Hu et al., 2006; Bianchi, 2007). Use of these ratios in conjunction may help to identify sediment samples derived from different regions, such as the CR, CG, and locally emplaced PWS sediment.

For the $\delta^{13}C$ and $\delta^{15}N$ analyses, cores PWS-10 and PWS-12 from Kuehl et al. (2017) and all newly obtained cores were finely subsampled in regions of interest identified in the XRF, X-radiograph and visual images, and were coarsely sampled (~ every 10 cm) throughout the rest of

the core. Cores PWS-(07, 08, 09) were measured using the surface 3-cm interval composited by Miller (2014). Homogenized samples were acidified with 3 mL of 1 M HCl, dried at 60° C for 48 hours, and 50-60 mg of sediment was weighed into 5x9 mm tins. The samples were then combusted and analyzed via Isotope Ratio Mass Spectrometry using a Costech Elemental Analyzer (Costech EA) at Baylor University.

CHAPTER 4: RESULTS

4.1 Core Descriptions

Coordinates for 2016 cores are in Table 1 and locations are shown in Fig. 2. Core descriptions are based on visual photographs and X-radiographs of structure, texture, and color taken immediately after the cores were split. The visual and X-radiograph mosaics are plotted alongside grain size, XRF, and stable isotope data of PWS-17 through PWS-28, respectively in Figs. 12-17. The sediments collected for this study are generally dark greenish gray in color (Gley 1 4/10Y), fine grained, and have little to no structure outside potential gravity flow deposits. Such deposits are marked by faint laminations and in some cases a dark gray (Gley 1 4/N) color, with coarse bases in the X-radiograph mosaics. With the exception of PWS-17 and PWS-28, the cores show faint mottling. PWS-28 (Fig. 17) has a dark gray color and sporadic gravel and cobbled sized particles, with occasional faint dark laminations. In the X-radiograph the laminations indicate thin fine grained layers spaced ~10-20 cm apart downcore.

The most prominent deposits in the X-radiograph and visual images occur in PWS-(17, 18, 22). There are fine laminated layers apparent in the X-radiograph of PWS-17 (Fig. 12, 60-70 cm), and in both the X-radiograph and visual image of PWS-22 (Fig. 15, 40-50 cm). PWS-18 (Fig. 13) contains two thick deposits (16-48 cm and 70 cm – bottom) with uniform color and structure separated by a region with some mottling. The upper deposit from 16 - 48 cm is dark gray (Gley 1 4/N) and the lower deposit is dark greenish gray (Gley 1 4/5GY) from 43 - 49 cm.

4.2 ^{210}Pb Behavior and Sedimentation Rates

Profiles of ^{210}Pb and ^{137}Cs activity were determined in all cores, and additionally ^{239,240}Pu was measured in PWS-17 and PWS-18. Sedimentation rates and associated errors for ^{210}Pb and ^{137}Cs are shown in Table 2 (Appendix 1), and the average rates are plotted as age models of depth versus time (Fig. 18). The ^{239,240}Pu maxima/appearance in cores PWS-17 and PWS-18 closely resembled that of the ^{137}Cs (Fig. 19), so a separate rate is not reported.

Three distinct types of ^{210}Pb profiles are apparent: steady state, non-steady state, and quasi-steady state (Fig. 20). Profiles defined at steady state display a region of exponentially decreasing activity with occasional fluctuations in event layers followed by a region of uniform activity supported by ^{226}Ra decay. The quasi-steady state profiles display steady state-like exponential decay, but also contain fluctuations in the ^{210}Pb activities that are not associated with event layers. The non-steady state profiles contain large regions of negligible excess ^{210}Pb activity, rendering the steady-state assumption invalid in calculating the sedimentation rate.

Cores PWS-17 and PWS-20 are treated as steady state. Sedimentation rates are calculated using the CF:CS model and equation 2. There is good agreement between the ^{210}Pb sedimentation rate and the rates estimated by the 1963 peak and 1954 first appearance in ^{137}Cs and ^{239,240}Pu (Table 2). The average sedimentation rate in PWS-17 is 1.28 ± 0.18 cm yr^{-1} and in PWS-20 is 1.41 ± 0.11 cm yr^{-1}.

The ^{210}Pb profiles in cores PWS-25 and PWS-22 are treated as quasi-steady state. The ^{137}Cs profiles in PWS-25 does not show a distinct peak associated with 1963 (Figs. 19 and 21), thus the Cs-estimated sedimentation rates use only the first appearance. The ^{210}Pb profile in PWS-25 contains some fluctuations in total ^{210}Pb activity between 10 cm and 20 cm, however there are no event layers evident in the visual, X-radiograph, or XRF scans, and the profile appears otherwise steady-state. PWS-22 contains three small ^{137}Cs peaks, and the peak around 35

cm is taken as 1963 because of its proximity to the inferred 1964 turbidite (Fig. 21). PWS-22 contains fluctuations in activity associated with event layers interpreted as the 1983 and 1964 events. However, there is a region with no indication of an event layer in any other data that shows negligible ^{137}Cs activity from 60 – 90 cm followed by a reappearance deeper in the core (~90 cm) with a corresponding increase in excess ^{210}Pb (Fig. 21). Since this region does not appear to be a gravity flow deposit, everything above 90 cm is treated as steady state. The ^{137}Cs and ^{210}Pb profiles in PWS-25 and the activity below 90 cm in PWS-22 are further explored in the section 5.2.3. The sedimentation rates in both cores are calculated using equation 2. The average sedimentation rate calculated in PWS-22 is 0.99 ± 0.11 cm yr^{-1} and in 25 is 0.77 ± 0.14 cm yr^{-1}.

PWS-18 and PWS-28 are both regarded as non-steady state. PWS-18 contains two large mixed regions of low ^{210}Pb and ^{137}Cs, ^{239,240}Pu activity (Fig. 19) which are associated with 1983 and 1964 based on their provenance (see section 4.3). The 1964 deposit is not entirely cored through in PWS-18, thus everything from the core base and up accumulated during/since the 1964 event. We considered excluding the regions of low activity to attempt a CF:CS model calculation, however it is not clear where the top of the 1964 deposit ends and background conditions resume. The CF:CS model applied to the upper 20 cm above the 1983 layer gives an accumulation rate of 0.44 ± 0.5 cm yr^{-1}. ^{137}Cs and ^{239,240}Pu are uniformly mixed within the 1964 event layer and are present through the core bottom. As a result, the apparent peak in activity (Fig. 19) cannot be confidently labeled as 1964 since it is likely the isotope profiles are truncated by the underlying mixed region. Assuming all the sediment in the core accumulated post-1964 (i.e., using the bottom as 1964, this results in an estimated rate of > 2.46 cm yr^{-1}.

In PWS-28, the first appearance of ^{137}Cs occurs around 20 cm while excess ^{210}Pb is detected only down to 5 cm (Fig. 19). The remainder of the core is composed of uniform (1.6 ±

0.05 DPM g^{-1}) ^{210}Pb activity. Assuming the first appearance of ^{137}Cs corresponds to 1954, this results in an estimated sedimentation rate of 0.32 cm yr^{-1}. Using the top two sample points with excess ^{210}Pb and the CF:CS model, the rate calculated is 0.12 cm yr^{-1}. However, the steady state assumption is violated by the observation of ^{137}Cs ~15 cm below the first appearance of ^{210}Pb, thus the CF:CS model is not plausible. Therefore, we were not able to confidently assign an accumulation rate to this core.

4.3 X-Ray Fluorescence Core Scans

XRF core scans produced downcore profiles of emission intensities (i.e., counts) for all measured elements. Ratios determined by Miller (2014), Marshall (2015), and Kuehl et al. (2017) as indicative of the local PWS watershed (K/Ca, Rb/Sr, and Rb/Ca) and CR sediment (Sr/Pb and Cu/Pb) are plotted alongside core mosaics for PWS-(17-28) (Figs. 12-17, Appendix 2). The XRF ratios are the primary data used to identify unique deposits in the cores and to delineate their upper and lower boundaries. Any sediments from outside these regions is henceforth referred to as 'background' sediment. The core-averaged background K/Ca ratio increases northward while the Sr/Pb ratio generally decreases (Table 3). The highest observed ratio of K/Ca occurs near CG in PWS-28 (0.68 ± 0.06) and is approximately two to three times higher than seen in all other cores.

Trends in the provenance signatures are compared between sediments of similar age in each core. Any trends which are consistent between cores and fall in the same age bracket are assumed as having been deposited by the same mechanism at the same time. We identify deposits which date near 1983 and 1964 in PWS-(17, 20, 22) and which correlate to the large deposits in PWS-18. PWS-17 additionally contains deposits from 1928, 1912, and 1899 events (Fig. 12).

4.4 Grain Size Profiles

In cores PWS-(17-28) the background mean grain size and sand+silt content decrease northward, while the clay content increases (Table 4, Appendix 3). The northern-most core PWS-28 has the lowest sand and silt content (1.0 ± 2.1% and 41.9 ± 3.1%, respectively), highest clay content (57.1 ± 3.8%), and smallest mean grain size (8.1 ± 4.7 μm) of all cores. Sediments associated with gravity flow deposits are not included in the core-averaged grain sizes and percentages.

The gravity flow deposits from 1983 were sampled in PWS-(17, 18, 20, 22). In PWS-18 the deposit is thick (~30 cm) with lamina in the base overlain by fine sediment (mean grain size 7.3 ± 3.3 μm) (Fig. 13) and in 20 it is composed of a coarse layer (mean grain size 318.6 ± 145.9 μm) (Fig 15). There are no significant grain size shifts in the deposits of PWS-17 and PWS-10 at the resolution they were sampled. The gravity flow deposits from 1964 in PWS-(17, 20, 22) were sampled in high resolution, and in PWS-18 the deposit was coarsely sampled. The deposit has a coarse base which fines upward in PWS-(17, 20, 22); PWS-18 appears to contain finer grains than the background. The 1928 event layer in PWS-17 (Fig. 12) was sampled in high resolution, but contains no distinct shifts in grain size. The 1912 and 1899 events were only sampled with a single point in each in the middle of the deposits, and both are finer grained than the background.

4.5 Stable Isotopes $\delta^{13}C$ and $\delta^{15}N$

Stable isotopes were analyzed in surface samples (0-3 cm) from PWS-(07, 08, 09) and downcore (every 10 cm and in higher resolution in deposits) in PWS-(10-28). The values of $\delta^{13}C$, $\delta^{15}N$, and C/N are plotted downcore in the individual core mosaics for PWS-(17-28) (Figs. 12-17, Appendix 4) and for PWS-10 and PWS-12 (Figs. 22 and 23). The surface samples in PWS-(07, 08, 09) display a slight increasing trend in $\delta^{13}C$ and a decreasing trend in C/N moving northward with no clear trend in $\delta^{15}N$ (Fig. 24). Core-averaged background $\delta^{13}C$, $\delta^{15}N$, and C/N

remain relatively consistent across PWS-17 to PWS-25 (Table 5). PWS-28 has the lowest mean stable isotope values (-24.87 ± 0.2 ‰ $\delta^{13}C$, 3.90 ± 0.3 ‰ $\delta^{15}N$, and 8.40 ± 0.8 C/N) of all cores. The extrema values (i.e., maximum value if the ratio increases, minimum value if it decreases) of the 1983 and 1964 deposits are generally lower in $\delta^{13}C$, higher in $\delta^{15}N$, and lower in C/N than the background (Fig. 24). The 1928 deposit was only coarsely sampled, but contains the lowest $\delta^{13}C$ sample in all of PWS-10 (-25.9 ± 0.04 ‰) (Fig. 24). The 1912 deposit $\delta^{13}C$ signatures are lower than the background in PWS-12 and PWS-17. The 1899 deposit is lower with respect to background in both PWS-12 and 17.

CHAPTER 5: DISCUSSION

5.1 South-North Background Sedimentation Trends

Results from the new cores collected for this study (PWS-(17-28)) were combined with those of previous studies (PWS-(07-12); Miller, 2014; Marshall, 2015; Kuehl et al., 2017) to elucidate trends throughout PWS, from HI to CG. The ensemble dataset generally shows decreasing sedimentation rate and mean grain size moving north from HI to CG, consistent with, but extending, the trends observed by Miller (2014) in PWS-07 through PWS-12 (Fig. 25). The sedimentation rates in PWS are highest in HI (4.4 ± 0.5 cm yr^{-1}) and decrease northward until PWS-10 (1.1 ± 0.1 cm yr^{-1}). The rates remain relatively consistent from PWS-10 to PWS-20 with the exception of PWS-18 which is located in the southern ponded sediment basin. The rates then continue to decrease northward until PWS-25, which has the lowest sedimentation rate calculated (0.77 ± 0.14 cm yr^{-1}). The core-averaged grain size and sand/silt content decrease northward, while the clay content increases (Fig. 25). The HI cores (PWS-07 and PWS-8) have mean grain sizes around 45 μm, while the southern cores PWS-09 through PWS-17 range from 22.3 to 18.1 μm. The northern cores PWS-18 through PWS-28 have smaller mean grain sizes ranging from 14.3 to 8.1 μm.

Miller (2014) and Marshall (2015) found the elevated sedimentation rates and mean grain size in HI and southern PWS are due to a combination of sediments directly deposited from the CR plume during summer, and winter storm resuspension events on the continental shelf which mobilize previously deposited coarser CR sediment from the GOA into HI. This influence is supported by elevated Sr/Pb in HI which decreases northward as K/Ca increases (Fig. 26). The progressive increasing $\delta^{13}C$ and decreasing C/N moving northward through PWS-(07, 08, 09) (Fig. 24) may also be related to changing influence from the CR and shelf sediments. Suspended sediment samples from the CR have $\delta^{13}C$ values of -24.5 ± 0.6 ‰ and C/N values of 12.7 ± 4.8 (Personal communication with J. Williams, 2017) and surface samples from the delta are in the range of -23.4 to -23.7 ‰ (Walinsky et al., 2009), while surface samples in HI (PWS-07) have $\delta^{13}C$ values of -24.33 ± 0.04 ‰ and C/N values of 14.5 ± 0.7, which further supports the CR as a potential source of the HI signatures.

The CG may act as a source of fine particles, high K/Ca, and low Sr/Pb, $\delta^{13}C$, $\delta^{15}N$, and C/N signatures (as seen in PWS-28) from northern PWS. However, the sedimentation rate in PWS-28 could not be calculated using ^{210}Pb, and it is not clear if the glacier still actively delivers substantial quantities of sediment beyond the moraine into PWS. The low ^{210}Pb values (1.6 ± 0.05 DPM g^{-1}) throughout PWS-28 are similar to the constant 1.1 ± 0.2 DPM g^{-1} observed within Columbia Bay that Boldt et al. (2016) attributed to high sedimentation rates from plume settling and sediment gravity flows that yielded no excess ^{210}Pb activity (Bolt et al., 2017). The possibility exists that sediment beyond the moraine currently accumulates by similar processes as within the fjord. PWS-28 contains faint banding every 10-20 cm in the visual and X-radiograph images (Fig. 17) that may indicate the occurrence of numerous sediment gravity flows. However, these gravity flows may have only occurred during early/prior to retreat, and the sedimentation

rate since this period may have dropped to the order of a few mm per year. Around ~1985 the glacier retreated beyond 2 km from the moraine, when Bolt et al. (2016) estimate significant sediment delivery to PWS ceased. If there was a significant decrease in the sedimentation rate or a cessation of gravity flows at the location of PWS-28 at this time, excess ^{210}Pb scavenging may have begun. If the first appearance of excess ^{210}Pb at 5 cm corresponds to ~1985, this indicates a sedimentation rate of 0.16 cm yr^{-1} since.

5.2 The 1964 Great Alaskan Earthquake

5.2.1 Regional Deposit Structure and Provenance

The 1964 deposit is identified and correlated using analogous trends in the provenance ratios in sediments that are of similar age in multiple cores (Fig. 27). The age ranges of the deposits are calculated using the LAR (Table 6) for the cores in this study and from Miller (2014). The 1964 deposit depth is plotted on the age models (Fig. 18), and there is good agreement between the date and the models of steady state cores PWS-17 and PWS-20. The northern cores PWS-(12, 18, 22) contain slightly coarser bases, with respect to background, and fine upwards (Fig. 27). PWS-18 did not capture the base of the flow, but the lower half is slightly coarser, suggesting a coarse base exists. The deposit is likely thicker (> 50 cm) in this core compared to all other sites because it is located in the southern ponded sediment basin, which acts as a retention area for flows. PWS-09 and PWS-17 also contain coarse bases which fine upwards. Excluding the deposit in PWS-18, the mean thickness is 12.3 cm with the thinnest in PWS-10 (7 cm). The coarse base and fining upward structure in most cores supports that the deposit is a turbidite created as a result of a turbidity current generated by the 1964 earthquake.

The extrema values of K/Ca and Sr/Pb (Fig. 26) and stable isotopes (Fig. 24) in the 1964 deposit are plotted alongside the average background values for each core. There are no clear

south-to-north trends, however the K/Ca value of the deposit is significantly different from that of the background (i.e., heteroscedastic t-test $p < 0.05$) in PWS-(10, 12, 17, 18, 22). The $\delta^{13}C$ deposit extrema values are significantly different in PWS-(12, 18, 22). To further compare the distinct signatures in the deposit, the XRF data is plotted as K/Ca versus Sr/Pb (Fig. 28) and the stable isotope data as $\delta^{13}C$ versus $\delta^{14}N$ (Fig. 29). These plots emphasize the deviation of deposit values from the background and allow the intensity of the deviations to be compared between cores. Within the deposits there are generally lower Sr/Pb, higher K/Ca, and lower values of $\delta^{13}C$ and $\delta^{14}N$ than the background. This trend is most distinct in PWS-12 and PWS-18 where the 1964 deposit plots outside the background.

A coarse (88% sand+silt) deposit around 80 cm in PWS-09 (Fig. 8 and 27) was previously inferred by Marshall (2015) to be from a period of increased CR discharge dated to 1977 by Miller (2014). Marshall speculated the deposit should also appear in PWS-08, however the 1977 interval dates to 150 cm depth and there is no clear deposit in the XRF ratios or grain size (Fig. 7). The ^{137}Cs peak associated with 1964 in PWS-09 occurs near 80 cm (Miller, 2014), which supports it may instead be from a 1964 gravity flow near HI. This also may explain why the deposit is not present in PWS-08 as the core is not long enough to capture the 1964 interval. If this deposit is from a HI-sourced flow, it may explain why the coarse layer in PWS-09 has higher Sr/Pb and lower K/Ca.

5.2.2 Central Channel Turbidity Current

Strong earthquakes can trigger submarine and terrestrial landslides in regions with steep slopes. Submarine slides can displace large quantities of water and cause localized tsunamis. There were 20 documented local tsunamis generated within minutes of the 1964 earthquake across different regions in PWS (Lander, 1996). Of the documented locations, those connected to

the central channel occurred around the Valdez arm in Tatitlek, Jack Bay, Valdez, Anderson Bay, and Shoup Bay. Several of the sites explicitly documented submarine landslides which damaged docks and generated tsunamis (Ryan et al., 2010; Haeussler et al., 2014; Brothers et al., 2016). The most extreme case was Valdez, where thirty people died when the dock sunk during the slide and the resultant tsunami destroyed all waterfront facilities (Nicolsky et al., 2013). All sites were struck by the tectonic tsunami waves (generated offshore by large scale vertical displacement) within 24 hours of the earthquake (Lander, 1996). The arrival of the tectonic waves could have disturbed the coastline and triggered additional gravity flows. Given the synchronous occurrence of the observed slides and tsunamis across PWS, it is likely that such activity was ubiquitous in PWS during the 1964 earthquake (Ryan et al., 2010; Haeussler et al., 2014; Brothers et al., 2016). The observed 1964 deposit in PWS-(09, 10, 12, 17, 18, 20, 22) supports the occurrence of widespread gravity flow activity. The subsequent turbidity current in the central channel would have been supplied with sediment from many different regions, giving it a heavily mixed signature in the proxies (Figs. 28 and 29).

The main gravity flow likely started at the channel head in the north and flowed southward. This is supported by the elevated PWS signatures in the deposits and the observed slides which started in the Valdez Arm. The only northern deposit with a sandy base (61.6% sand) is in PWS-20 (Fig. 27). This site is only 2 km east of PWS-12, but there is a submarine ridge over 40 m high between the sites (Fig. 4). PWS-20 may have received a separate turbidity current from the northeast near Tatitlek instead of the central channel which contained larger quantities of sand. The great decrease in thickness and structure between the northern cores (PWS-(18-28)) and PWS-10 suggests the northern turbidity current reached the limit of its

runout in southern PWS at the end of the central channel and the base of the slope towards PWS-09 and HI (Fig. 4).

The 1964 event deposit in PWS-17 contains coarser material (Fig. 27) and higher $\delta^{13}C$ (-20.5 ± 0.04 ‰; Fig. 29) than observed in PWS-(12, 18, 22). Starting from the base and moving up, there is an initial decrease in K/Ca and Rb/Sr, followed by increasing values. The $\delta^{13}C$ is high in the base which then shows a sharp decrease followed by a secondary peak. The presence of northern signatures in the 1964 deposit at PWS-10 and the upper portion of the PWS-17 deposit suggest this region received sediment from the northern flow. However, the lower sand content (< 10%) in most northern deposits suggests it is unlikely that PWS-17 received sand (28.1%) from the northern flow. This unique grain size compared to the other deposits and the sharp reversal of XRF and stable isotope signatures in PWS-17 may be due to inputs from multiple gravity flows.

PWS-17 may have received the HI-sourced flow present in PWS-09 composed of coarser particles and decreased PWS ratios, and later distal deposition of fine grains and PWS signatures from the northern flow. However, the surface samples in PWS-(07, 08, 09) do not indicate that HI contains higher (-20 ‰) $\delta^{13}C$ values. One possibility is that these 3 cm thick samples homogenized the summer and winter deposits in HI, which may have different signatures of $\delta^{13}C$. The summer deposition contains sediment transported directly from the CR plume, which has lower $\delta^{13}C$ (-24.5 ± 0.6 ‰, personal communication with J. Williams, 2017). Winter deposits are composed of sediment that has been on the GOA shelf for an unknown length of time and may have amassed higher (more marine) $\delta^{13}C$ signatures. Winter deposits are also the primary source of coarse material in HI and likely contributed most of the coarse material in the flow to PWS-09, and potentially PWS-17. Another possibility is that a flow sourced east of the central

channel delivered the unique $\delta^{13}C$ signatures. A 1964 deposit is observed in Orca Bay in core PWS-13 (Fig. 2) of Miller (2014). Further, samples from Simpson Bay (fjord connected to Orca Bay) contain $\delta^{13}C$ signatures around -22 ‰, with the highest observed at -19.47 ‰ (Pondell, 2008), supporting that an eastern PWS flow could have supplied the unique signature to PWS-17.

The wide-spread occurrence of turbidites associated with 1964 and their high degree of structural and compositional variability across PWS indicate that the entire region experienced numerous synchronous surge-induced currents which flowed into, mixed together, and overlaid one another within the central channel. Thus a megathrust earthquake turbidite may stand apart in the sedimentary record from smaller magnitude events based on the spatial extent of its deposition, the mixture of proxies in its composition, and layering from numerous flows.

5.2.3 Northeastern Channel Flank

PWS-25 was the shallowest of the northern PWS cores (379 m) and was taken along the northeastern flank of the central channel (Fig. 2 and 4), thus a gravity flow channelized in the deeper portions of the channel may not pass over this site. There is a single coarse sample at 10 cm (increase in sand content from less than 1% to 35%) coincident with a sharp maxima in Sr/Pb (Fig. 16). The core contains no other indication of a deposit related to the 1964 turbidity current in the other XRF ratios, stable isotopes, or visual/X-radiograph images. While there is no clear 1963 peak in ^{137}Cs, the highest value of ^{137}Cs occurs around 10 cm coincident with the sandy layer (Fig. 21). However, the 1954 first appearance depth requires that 40 cm of sediment were deposited over the 10 year period between the first appearance and 'apparent' 1963 peak. The CF:CS sedimentation rate is 0.77 ± 0.14 cm yr^{-1}, supported by the low sedimentation rate (0.65 cm yr^{-1}) in nearby core 204 of Jaeger et al. (1998) (Fig. 4). This indicates that the rates in this

region cannot account for 40 cm of deposition over 10 years. Additionally, if this layer corresponds to the 1963 ^{137}Cs peak or the 1964 earthquake, an additional 40 cm of sediment should have accumulated overtop by the coring year 2016, which is not the case. It is not clear why the sandy layer and higher ^{137}Cs occur at 10 cm depth, but given the discrepancy between this depth and the LAR age estimates, it is likely this layer does not correspond to the 1963 ^{137}Cs peak or 1964 earthquake.

At the base of the eastern channel flank just 6 km south of PWS-25 is PWS-22 (427 m depth). Although there is a clear 1964 turbidite in PWS-22, suggesting the main channel flow passed over this site, the region of low ^{210}Pb and negligible ^{137}Cs activity (60 – 90 cm) may also have resulted from the 1964 event (Fig. 21). One possible explanation is that the 1964 earthquake generated nearby slides of older (low ^{210}Pb and negligible ^{137}Cs) material that moved downslope and were deposited over younger sediments. This could leave behind no unique XRF, stable isotopes, or grain size signatures if there was no turbulent mixing and if there is no significant difference in the provenance signatures between the upper and lower sediment packages. The slide deposit could then be topped by the 1964 turbidity current, which may have occurred simultaneously or arrive from a distal location shortly after the slump (Fig. 21).

5.3 The 1983 Gravity Flow

5.3.1 Regional Deposit Structure and Provenance

A deposit from the 1983 event is present in cores PWS-(10, 12, 17, 18, 20, 22), indicating it was a large flow on par with the 1964 northern turbidity current (Fig. 30). The age ranges of the deposits are calculated using the average LAR and are shown in Table 6. The 1983 deposit ranges from 2-10 cm thick in all cores with the exception of PWS-18 (32 cm). PWS-20 is the only core with a coarse layer (80% sand+silt) indicating it may have been disconnected from the central channel flow by the submarine ridge (Fig. 4) and received a separate proximal flow from

the northeast near Tatitlek. The deposits in PWS-12 and PWS-18 are characterized by thin lamina in the base topped by finer grains (< 10 μm) and have a dark gray color (Fig. 30). The XRF ratios display consistent signatures across all cores with an increase in local PWS signatures and a decrease in CR signatures, and the stable isotopes show lower signatures than the background (Fig. 30). According to the model of Talling (2014), the thin, fine grained structure and increased signatures of terrestrial organics suggests the deposit may be a hyperpycnite.

Sediments from the 1983 gravity flows are plotted as their extrema values alongside core-averaged background of K/Ca and Sr/Pb (Fig. 26) and of stable isotopes (Fig. 24). The deposit is significantly different (t-test, $p<0.01$) from the background in PWS-12 in K/Ca, in PWS-10 in $\delta^{13}C$, and in PWS-18 in both K/Ca and $\delta^{13}C$. The extrema in K/Ca and $\delta^{13}C$ in PWS-12 and PWS-18 are close to the values observed in the core-averaged background of PWS-28 (Fig. 24 and 26), which serves as an endmember for CG (i.e., local PWS) sediment. The PWS-12 and PWS-18 deposits are also have more distinct signatures from the background than the 1964 deposit and have similar values to that seen in PWS-28 (Figs. 28 and 29). The dark gray color and finer grain sizes (7.3 to 9.2 μm) of the deposit in these cores is also similar to that seen in PWS-28 (8.1 ± 4.7 um).

Compared with the 1983 deposit, the 1964 turbidite in PWS-18 has an intermediate color between that of the background and 1983 deposit. The K/Ca and stable isotope signatures of the turbidite likewise fall between the background and 1983 deposit (Figs. 28 and 29). This suggests the 1964 turbidity current contained glacial sediment which was heavily mixed with other sources from around PWS during the earthquake, while the 1983 event appears to have been comprised largely of undiluted CG-derived sediment.

5.3.2 Timing and Triggering Mechanisms

The distinct provenance of the 1983 deposit from the 1964 turbidite and the similarity to CG sediment indicates the 1983 gravity flow was sourced solely from the northern reaches of PWS. With deposits up to 30 cm thick (PWS-18), over 40 km away from the potential source region (i.e., CG), the 1983 event was evidently a large gravity flow. Miller (2014) interpreted this deposit to be derived from seismic activity. In 1983, on July 12th there was a M_w 6.6 earthquake approximately 12 km west of Columbia Bay, and another on September 7th of M_w 6.4 approximately 23 km west (Fig. 9). It is unlikely that an earthquake of this magnitude could generate slides or slumps across the entire PWS as did the magnitude 9.2 (~8000 times more energy released), but it is possible that slopes near the CG region rapidly accumulated sediment and could have undergone failure during the earthquake(s), thus initiating a turbidity current. It is also possible that the earthquake(s) caused the ice-dams in the lakes to break (Post and Mayo, 1971; Mulder et al., 2003), or caused the glacier to release a subglacial outburst flood, potentially resulting in an earthquake-generated hyperpycnal flow. However, Meier et al. (1984) documented no visible surface water discharge from the terminus during either of these events.

The sedimentation rates in PWS-10 and PWS-12 date the deposit across the mid- to late 1980s (Miller, 2014), with 1983 representing the oldest age. Age models for cores PWS-(17, 20, 22, 25) indicate that the depth of the 1983 deposit (plotted as a blue bar, Fig. 18) dates from the mid-1980s through 1990s. Therefore, the 1983 earthquakes do not correspond exactly with the event deposit age. Another potential trigger could have been the fall in the levels of Lake Kadin in 1982 and/or both lakes in 1986, which may have flushed large quantities of subglacial sediment into PWS. Alternatively, during the early onset of retreat off the moraine in the early and mid-1980s a large subglacial reservoir of freshwater and sediment may have rapidly discharged into PWS. There are documented occurrences from later in the retreat of CG

experiencing large increases in sedimentation while the terminus passing over submarine shoals (Boldt et al., 2016), so it may be possible such a phenomenon occurred at the onset as well. If the lake level fall or potential subglacial reservoir flushing caused an outburst flood, substantial quantities of CG sediment would have been transported to PWS via hyperpycnal flow. Any resulting deposits would be within the dating range of the observed deposit.

While deposit structure and composition indicate the gravity flow originated from the CG region, it cannot be confidently concluded that it was delivered via hyperpycnal flow. For example, glacially derived sediment may build up in northern PWS over time via plume settling or local gravity flows from the glacier. This sediment would have lower stable isotope signatures, finer grain sizes, higher K/Ca, Rb/Sr, and Rb/Ca signatures, and possibly a color similar to that seen in PWS-28. This sediment could then be remobilized during earthquakes or tsunamis as a turbidity current which could leave a deposit similar to that seen in our cores. While the majority of the deposits do not have bases as coarse as in 1964 (i.e., a turbidite), they also do not display the characteristic coarsening upwards base of theoretical hyperpycnites (Fig. 30 and 10). Therefore, in this case, the available data on thicknesses, grain size, XRF, and stable isotopes offer no conclusive insight into the type of flow which mobilized the sediment. Though, the known occurrence of the earthquakes, the glacial signature of the deposit, and the established occurrence of earthquake-induced gravity flows in PWS indicate that it was most likely deposited by a northern turbidity current triggered by the 1983 earthquake(s).

5.4 Additional Event Deposits

PWS-17 contains three additional deposits which are correlated with the 1928, 1912, and 1899 deposits (Fig. 31) observed in PWS-10 and PWS-12 by Miller (2014) and Kuehl et al. (2017). The 1928 deposit is present in PWS-10 and PWS-17 and was most likely caused by a M_w

6.8 earthquake in southern PWS (Fig. 9). Dosier et al. (2001) recalculated the epicenter as being located along northern Montague Island (southwestern PWS). Both cores display increases in PWS signatures. There is no related deposit present at PWS-12, suggesting that local slumps or flows were generated within southern PWS, deposited at sites PWS-10 and PWS-17, and reach the limit of runout before PWS-12.

The 1912 deposit is present in PWS-12 and PWS-17, and may also be present in PWS-10 from 96 – 103 cm (Fig. 31; previously unnoted by Miller (2014)). In PWS-10 the center of the deposit dates to 1921. It is possible an earthquake that occurred in 1925 (M_w = 6.6) in northwestern PWS (Fig. 9) generated the PWS-10 deposit instead of the 1912 earthquake. However, it seems unlikely a northern earthquake would generate a localized deposit in southern PWS without leaving a record in northern PWS (i.e., there is no 1925 deposit in any other core), which has proven sensitive to seismic activity. Thus, this deposit is interpreted as part of the 1912 event. In 1912 a M_w 7.0 (recalculated as 7.25 by Doser et al. (2006)) earthquake occurred west/southwest of Columbia Bay (Fig. 9) which may have triggered wide-spread activity around PWS. In PWS-10 the deposit has an increase in Sr/Pb and $\delta^{13}C$ while there is a decrease in K/Ca and no change in Rb/Sr (Fig. 31), suggesting a possible flow from HI or another location in southern PWS. In PWS-12 the deposit has elevated levels of K/Ca, lower Sr/Pb, and a lower $\delta^{13}C$ signature compared to the background (Figs. 31), and the signatures plot between the 1964 and 1983 events (Figs. 28 and 29) indicating a northern source. In PWS-17 the base of the deposit appears to have CR signatures and a small peak in $\delta^{13}C$ which reverse into PWS signatures moving upwards (Figs. 31), suggesting there may have been separate flows from northern and southern sources similar to that discussed for the 1964 gravity flow in section 5.2.2.

PWS-17 and PWS-12 contain deposits dating to around 1899. In September of 1899, the Yakutat Bay region (Fig. 9) experienced a series of severe earthquakes occurring on Sept. 3rd, 10th, and the 23rd (Martin, 1910). The most severe earthquake occurred on the 10th and was upwards of M_w 8.0, generating submarine landslides and tsunamis in Valdez over 300 km away from the epicenter (Lander, 1996). It is likely that the deposits in PWS-17 and PWS-12 are related to this period of activity. Several samples from the 1899 deposit in PWS-17 have higher K/Ca than the background and all other deposits in the core (Fig. 28), and in the stable isotopes of PWS-12 (Fig. 29) the event also plots as lower than the background. This indicates the 1899 event was sourced from northern PWS. These proxies and the record of slides in Valdez suggest a significant northern flow traversed the central channel. The 1899 turbidity current may not have been on the same scale as flows related to earthquakes $M_w \geq 7.0$ within PWS (i.e., 1983, 1964, and 1912), which may account for the lack of any deposits (southern or northern) in PWS-10.

5.5 Paleoseismic Preservation Potential in PWS

Earthquakes of significant magnitude ($M_w > 6.0$) within PWS spawn gravity flows capable of traversing large distances. Cores spanning 34 km along the central channel contain deposits with distinct provenance from the 1964 earthquake and the 1983 event (Fig. 32). However, there is high variability in the presence, thickness, and provenance of deposits across PWS. PWS-20 and PWS-22 do not contain deposits from the 1928, 1912, or 1899 events, suggesting they are only sensitive to the largest central channel flows.

Of the cores in the northern central channel (i.e. PWS-(12, 18, 20, 22, 25, 28)), the most distinct deposits in terms of their proxy (Figs. 28 and 29), visual, X-radiograph, and grain size signature (Figs. 27 and 30) are in PWS-12 and PWS-18. As northern-derived flows pass over the

northern ponded sediment basin and move upslope towards the site of PWS-12 (Fig. 4), they likely decelerate and facilitate higher sedimentation with little erosion. The notably thick deposits in PWS-18 suggest the southern ponded sediment basin (Fig. 4) is a region of extensive deposition and captures most of the turbidity currents traveling down the central channel. Jaeger et al. (1998) collected core 202 KC1 just 2.5 km south of PWS-18 located in the southern ponded sediment basin (Fig. 4). They observed inferred turbidity current deposits with similar thickness, position, and low excess ^{210}Pb activity as the 1983 and 1964 deposits in PWS-18. The base of the 1964 turbidite was not captured by PWS-18 or Core 202 KC (128 cm and ~250 cm length, respectively) indicating that the 1964 turbidite in this basin is greater than 170 cm thick (Jaeger et al., 1998).

In the northern ponded sediment basin, 2 m gravity cores could not be retrieved between three different sites, probably because the surface sediments are too unconsolidated. This suggests sediments also accumulate in the northern ponded sediment basin rapidly. Since the sedimentation rates in northern PWS are low (< 1 cm yr^{-1}), the basin may be receiving large quantities of sediment from periodic gravity flows. Such large deposits are easier to identify than thin diffuse deposits and allow grain size, elemental, and stable isotopic signatures to be assessed in high resolution. Thus, the southern ponded sediment basin and the potential deposits in the northern basin make these locations ideal for capturing a robust record of northern central channel sediment gravity flows.

Southern PWS contains distal deposition from northern flows and is sensitive to flows sourced locally from the eastern (e.g., the 1964 deposit in PWS-13) and western (e.g., the 1928 deposit in PWS-10) PWS and potentially within HI (e.g., the 1964 deposit in PWS-09). While the XRF and stable isotope deposit signatures in PWS-17 may not be as distinct from the

background as in PWS-12 and PWS-18 (Figs. 28 and 29), this site still receives well-defined deposits (Figs, 12, 27, 30) and appears more sensitive to turbidite deposition than the site of PWS-10 because it contains deposits related to every event detected in this and previous studies (Miller, 2014; Kuehl et al., 2017). PWS-09 contains a record of gravity flows derived near HI with distinct provenance from the background (Fig. 28) and, when compared with the record in PWS-17, can help identify which flows are coming from the north vs south.

Overall, for future studies, the best locations to capture and reconstruct a regional paleoseismic record ranges from the southern flank of the central channel (near PWS-09), through the sites of PWS-17 to PWS-12, and ponded sediment basins (Fig. 32). Deposit thicknesses in this region are large enough to be clearly separate from the background in the XRF data and allow for easy subsampling in the lab for high resolution grain size and stable isotope analyses. Long cores collected from these regions have the potential to house a 4,000 year history.

CHAPTER 6: CONCLUSIONS

This work has filled a knowledge gap in northern PWS on the recent (<100 years) sedimentation rates and the grain size, elemental, and stable isotopic composition. The paleoseismic record assessed here is a vital tool for seismological studies within south central Alaska. The sedimentary record of earthquakes represents a secondary form of evidence, with primary forms being that which directly reflect the amount of slip on a fault (McCalpin and Nelson, 2009). However, all events (i.e. earthquakes or clusters of earthquakes) of magnitudes 6.5 or greater which occurred within central-eastern PWS or along the adjacent coastlines have corresponding turbidites in the central channel. This indicates that the sedimentary record is relatively complete and may only underepresent the number of events when considering high

temporal resolutions (i.e. earthquakes occurring on the scale of a few days to years apart). Such records reduce the large epistemic uncertainties encountered when attempting to characterize the seismicity of major fault systems (McCalpin, 2009).

The methods developed and employed in this work used to assess the paleoseismic record in south-central Alaska are novel to this region. This approach may also be useful in other seismically active locations around the globe. In order for this approach to be viable, a location must have (1) a semi-enclosed basin which is known to spawn/receive gravity flows during earthquakes, (2) steep bathymetry which focuses flows into identifiable regions of run-out and/or ponding, and (3) at least one external sedimentary source with unique provenance signatures compared to locally emplaced sediments (such as the CG or CR in this study).

- Along with the elemental ratios identified by Miller (2014) and Marshall (2015), stable isotopes $\delta^{13}C$ and $\delta^{15}N$ and the C/N ratio are useful tools in distinguishing gravity flow deposits from one another and from background sediment. In particular, sediment from northern PWS near the CG has distinctly high K/Ca, Rb/Sr, and Rb/Ca ratios, and lower Sr/Pb, Cu/Pb, $\delta^{13}C$, $\delta^{15}N$, and C/N relative to the background sediment in the central channel of PWS.

- There are highly varied degrees of mixing in the elemental ratios and stable isotope values between deposits from different events (e.g., 1983 vs. 1964, Figs. 28 and 29) which result from the differing locations and magnitudes of earthquakes in south-central Alaska. Earthquakes on the order of $M_w < 7.0$ trigger flows nearby the epicenter (e.g., 1983 and 1928), while those of $M_w \geq 7.0$ may spawn flows from many locations at once (e.g., 1964 and 1912). The northern PWS may be more sensitive to earthshaking since the distal 1899 event only appears to have generated gravity flows from the north. This may allow the relative

magnitude (i.e., M_w > or < 7.0) and relative location (i.e., north vs south PWS) of earthquakes in the paleoseismic record to be determined.

- There is large variability between deposits of the same event in the thickness, color, grain size, and proxy signatures which is highly dependent upon proximity to the flow source and local bathymetry. The ideal location to assess the paleoseismic record in PWS spans from the southern end of the central channel to the northern ponded sediment basin (Fig. 32). The southern flank (PWS-09) contains a record of southern flows, while the site of PWS-17 has deposits from numerous locations. The southern ponded sediment basin at PWS-18 is an area with thick deposits which may also capture northern and southern flows. The region of PWS-12 contains a record of northern flows which may also be captured in thicker deposits in the northern ponded sediment basin. A transect of cores taken at these sites will contain a record of earthquakes and may allow the relative location and magnitude of different events to be assessed.

REFERENCES

Alley, R., Lawson, D., Larson, G., Evenson, E., Baker, G., 2003. Stabilizing feedbacks in glacier-bed erosion. Nature 424 (6950), 758-760.

Bagnold, R., 1962. Auto-suspension of transported sediment: Turbidity currents. Proceedings of the Royal Society of London, Series A, Mathematical and Physical Sciences 265(1322), 315-319.

Barclay, D., Wiles, G., P. Calkin, 2009. Holocene glacier fluctuations in Alaska. Quaternary Science Reviews 28, 2034-2048.

Barron, J. and L. Anderson, 2011. Enhanced Late Holocene ENSO/PDO expression along the margins of the eastern North Pacific. Quaternary International 235 (1-2), 3-12.

Beckwith-Laube, M., Wiles, G., Calkin, P., Post, A., 2004. Tree-ring dated 1000-year advance of Columbia Glacier. 34th International Arctic Workshop Program and Abstracts, 30.

Beuselinck, L., Govers, G., Poesen, J., Degraer, G. and L. Froyen, 1998. Grain-size analysis by laser diffractometry: comparison with the sieve-pipette method. CATENA 32 (3-4), 193-208.

Bianchi, T., 2007. Biogeochemistry of Estuaries. Oxford University Press, New York.

Bianchi, T. and E. Canuel, 2011. Chemical Biomarkers in Aquatic Ecosystems. Princeton University Press, Princeton.

Boldt, K., 2014. Fjord sedimentation during the rapid retreat of tidewater glaciers: observations and modeling. Program of Oceanography Doctor of Philosophy dissertation, University of Washington, Seattle, Washington, 1-162.

Boldt, K., Hallet, B., Pratt, T., O'Neel, S., 2016. Observations and modeling of fjord sedimentation during the 30 year retreat of Columbia Glacier, AK. Journal of Glaciology 62 (234), 778-793.

Boggs, K., 2000. Classification of community types, successional sequences, and landscapes of the Copper River Delta, Alaska. General Tehcnical Report PNW-GTR-469. U.S. Department of Argriculture.

Bouma, A., 1962. Sedimentology of some Flysch deposits: A graphic approach to facies interpretation. Elsevier, Amsterdam.

Brothers, D., Haeussler, P., Liberty, L., Finlayson, D., Geist, E., Labay, K. and M. Byerly, 2016. A submarine landslide source for the devastating 1964 Chenega tsunami, southern Alaska. Earth and Planetary Sciences Letters 438, 112-121.

Brown, C., Meier, M. and A. Post, 1982. Calving Speed of Alaska Tidewater Glaciers, With Application to Columbia Glacier. U.S. Geologic Survey Professional Paper 1258-C.

Carlson, P. and B. Molnia, 1978. Minisparker profiles and sedimentologic data from the R/V "Acona" cruise (April 1976) in the Gulf of Alaska and Prince William Sound. United States Geological Survey Open-File Report 78-381.

Carver, G. and G. Plafker, 2008. Paleoseismicity and Neotectonics of The Aleutian Subduction Zone-An Overview, in Active Tectonics and Seismic Potential of Alaska, edited by J. Freymueller, P. Haeussler, R. Wesson and G. Ekstrom, 43-64.

Chen, S., Geyer, R. and T. Hsu, 2013. A numerical investigation of the dynamics and structure of hyperpycnal river plumes on sloping continental shelves. Journal of Geophysical Research: Oceans 118, 2702-2718.

Cloern, J., Canuel, E. and D. Harris, 2002. Stable carbon and nitrogen isotope composition of aquatic and terrestrial plants of the San Francisco Bay estuarine system. Limnology and Oceanography 47 (3), 713-729.

Condie, K., 1997. Plate Tectonics and Crustal Evolution: Fourth Edition. Pergamon Press Inc., Tarrytown, NY.

Cutshall, N., Larsen, I. and C. Olsen, 1983. Direct analysis of 210Pb in sediment samples: Self-absorption corrections. Nuclear Instruments and Methods 206, 309-312.

Doser, D. and W. Brown, 2001. A study of historic earthquakes of the Prince William Sound, Alaska region. Bulletin of the Seismological Society of America, 842-855.

Doser, D., 2006. Relocation of earthquakes (1899-1917) in south-central Alaska. Pure and Applied Geophysics 163, 1461-1476.

Dumoulin, J., 1987. Sandstone composition of the Valdez and Orca Groups, Prince William Sound, Alaska. U.S. Geological Survey Bulletin 1774, 1-37, http://pubs.er.usgs.gov/publication/b1774 .

Engdahl, E. and A. Villaseñor, 2002. Global Seismicity: 1900-1999. International Handbook of Earthquake and Engineering Seismology 81 (A), 665-690.

Feely, R., Baker, E., Schumacher, J., Massoth, G. and W. Landing, 1979. Processes affecting the distribution and transport of suspended matter in the northeast Gulf of Alaska. Deep-Sea Research 26A, 445-464.

Finn, S., Liberty, L., Haeussler, P. and T. Pratt, 2015. Landslides and Megathrust Splay Faults Captured by the Late Holocene Sediment Record of Eastern Prince William Sound, Alaska. Bulletin of the Seismological Society of America 105 (5), 2343-2353.

Fleming, S. and P. Whitfield, 2010. Spatiotemporal Mapping of ENSO and PDO Surface Meteorological Signals in British Columbia, Yukon, and Southeast Alaska. Atmosphere-Ocean 48 (2), 112-131.

Goldfinger, C., Nelson, C. and J. Johnson, 2003a. Deepwater turbidites as Holocene earthquake proxies-The Cascadia subduction zone and northern San Andreas fault sytems. Annali Geofisica 46, 1169-1194.

Goldfinger, C., Nelson, C. and J. Johnson, 2003b. Holocene earthquake records from the Cascadia subduction zone and northern San Andreas fault based on precise dating of offshore turbidites. Annual reviews of Earth and Planetary Science 31, 555-577.

Goldfinger, C., Nelson, C., Morey, A., Johnson, J., Patton, J., Karabanov, E., Gutierrez-Pastor, J., Eriksson, A., Gracia, E., Dunhill, G., Enkin, R., Dallimore, A. and T. Vallier, 2012. Turbidite Event History-Methods and Implications for Holocene Paleoseismicity of the Cascadia Subduction Zone. U. S. Geologic Survey Professional Paper 1661-F.

Goldfinger, C., Morey, A., Black, B., Beeson, J., Nelson, C. and J. Patton, 2013. Spatially limited mud turbidites on the Cascadia margin: segmented earthquake ruptures? Natural Hazard Earth System Science 13, 2109-2146.

Gudmundsson, M., Sigmundsson, F. and H. Björnsson, 1997. Ice-volcano interaction of the 1996 Gjálp subglacial eruption, Vatnajökull, Iceland. Nature 389, 954-957.

Haeussler, P., Parsons, T., Finlayson, D., Hart, P., Chaytor, J., Ryan, H., Lee, H., Labay, K., Peterson, A. and L. Liberty, 2014. New Imaging of Submarine Landslides from the 1964 Earthquake Near Whittier, Alaska, and a Comparison to Failures in Other Alaskan Fjords. S. Krastel et al. (eds), Submarine Mass Movements and Their Consequences. Advances in Natural and Technological Hazards Research 37, DOI 10.1007/978-3-319-00972-8 32.

Haeussler, P., Armstrong, P., Liberty, L., Ferguson, K., Finn, S., Arkle, J. and T. Pratt, 2015. Focused exhumation along megathrust splay faults in Prince William Sound, Alaska. Quaternary Science Reviews 113, 8-22.

Halverson, M., Belanger, C. and S. Gay, 2013. Seasonal transport variations in the straits connecting Prince William Sound to the Gulf of Alaska. Continental Shelf Research 63, S63-S78.

Hartmann, B. and G. Wendler, 2005. The significance of the 1976 Pacific climate shift in the climatology of Alaska. Journal of Climate 18, 4824-4838.

Hess, R. and S. Chough, 1980. The Northwest Atlantic Mid-Ocean Channel of the Labrador Sea: II. Deposition of parallel laminated levee-muds from the viscous sublayer of low density turbidity currents. Sedimentology 27, 697-711.

Heezen, B. and M. Ewing, 1952. Turbidity Currents and Submarine Slumps, and the 1929 Grand Banks Earthquake. American Journal of Science 250, 849-873.

Hu, J., Ping'an, P., Jia, G., Mai, B. and G. Zhang, 2006. Distribution and sources of organic carbon, nitrogen and their isotopes in sediments of the subtropical Pearl River estuary and adjacent shelf, Southern China. Marine Chemistry 98, 274-285.

Humphrey, N., Kamb, B. and M. Fahnestock, 1993. Characteristics of the bed of the lower Columbia Glacier, Alaska. Journal of Geophysical Research 98, 837-846.

IMLGS, 2004. Index to Marine and Lacustrine Geological Samples. https://www.ngdc.noaa.gov/geosamples/leg.jsp?leg=EW0408

Jaeger, J., Nittrouer, C., Scott, N. and J. Milliman, 1998. Sediment accumulation along a glacially impacted mountainous coastline: north-east Gulf of Alaska. Basin Research 10, 155-173.

Jaeger, J. and C. Nittrouer, 1999. Sediment deposition in an Alaskan fjord; controls on the formation and preservation of sedimentary structures in Icy Bay. Journal of Sedimentary Research 69 (5), 1011-1026.

Jin, M. and J. Wang, 2004. Interannual variability and sensitivity study of the ocean circulation and thermohaline structure in Prince William Sound, Alaska. Continental Shelf Research 24, 393─411.

Johnson, W., Royer, T. and J. Luick, 1988. On the seasonal variability of the Alaska Coastal Current. Journal of Geophysical Research 93 (C10), 12,423-12,437

Kassem, A. and J. Imran, 2001. Simulation of turbid underflows generated by the plunging of a river. Geology 29 (7), 655-658.

Kaufman, C., Lamoureux, S. and D. Kaufman, 2011. Long-term river discharge and multidecadal climate variability inferred from varved sediments, southwest Alaska. Quaternary Research 76 (1), 1-9.

Ketterer, M., Hafer, K., Jones, V. and P. Appleby, 2004. Rapid dating of recent sediments in Loch Ness: inductively coupled plasma mass spectrometric measurements of global fallout plutonium. Science of The Total Environment 322 (1-3), 221-229.

Ketterer, M., Watson, B., Matisoff, G. and C. Wilson, 2002. Rapid Dating of Recent Aquatic Sediments Using Pu Activities and $^{240}Pu/^{239}Pu$ As Determined by Quadrupole Inductively Coupled Plasma Mass Spectrometry. Environmental Science and Technology 36, 1307-1311

Klein, L., 1983. Provenances, depositional rates and heavy metal chemistry of sediments, Prince William Sound, southcentral Alaska. University of Alaska, Master of Science thesis, Fairbanks, Alaska, 1-107.

Kneller, B. and C. Buckee, 2000. The structure and fluid mechanics of gravity currents: A review of some recent studies and their geological implications. Sedimentology 47 (1), 62-94.

Krimmel, R., 2001. Photogrammetric data set, 1957─2000, and bathymetric measurements for Columbia Glacier, Alaska. United States Geological Survey Water-Resources Investigations Report 01─4089, 1-46.

Krishnaswamy, S., Lal, D., Martin, J. and M. Meybeck, 1971. Geochronology of lake sediments. Earth and Planetary Science Letters 11 (1-5), 407-414.

Kuehl, S., DeMaster, D. and C. Nittrouer, 1986. Nature of sediment accumulation on the Amazon continental shelf. Continental Shelf Research 6 (1/2), 209-255.

Kuehl, S., Ketterer, M. and J. Miselis, 2012. Extension of ^{239}–^{240}Pu sediment geochronology to coarse-grained marine sediments. Continental Shelf Research 36, 83-88.

Kuehl, S., Miller, E., Marhsall, N. and T. Dellapenna, 2017. Recent paleoseismicity record in Prince William Sound, Alaska, USA. Geo-Marine Letters, doi:10.1007/s00367-017-0505-7.

Kuenen, P., 1957. Sole Markings of Graded Graywacke Beds. The Journal of Geology 65 (3), 231-258.

Kuenen, P. and C. Migliorini, 1950. Turbidity currents as a cause of graded bedding. Journal of Geology, 58, 91–127.

Lander, J., 1996. Tsunamis affecting Alaska. 1737–1996. No. 31 in NGDC Key to Geophysical Research, NOAA National Geophysical Data Center, Boulder, Colorado.

L'Heureux, M., Mann, M., Cook, B., Gleason, B. and R. Vose, 2004. Atmospheric circulation influences on seasonal precipitation patterns in Alaska during the latter 20th century. Journal of Geophysical Research 109 (D6), doi: 10.1029/2003JD003845.

Liberty, L. and S. Finn, 2013. Near surface expression of megathrust splay faults, Prince William Sound area, Alaska, U.S. Geological Survey Earthquake Hazards Program Final Report for Award #G11AP20143, 1-23, http://earthquake.usgs.gov/research/external/reports/G11AP20143.pdf

Mantua, N., Hare, S., Zhang, Y., Wallace, J. and R. Francis, 1997. A Pacific interdecadal climate oscillation with impacts on salmon production. Bulletin of the American Meteorological Society 78 (6), 1069─1079.

Marshall, N., 2015. Signature of Recent Sediment Accumulating in Prince William Sound, Alaska: A Record of Storms, Earthquakes, and Seasonal Inputs. School of Marine Science Master of Science thesis, Virginia Institute of Marine Science, College of William and Mary, Williamsburg, Virginia, 1-172.

Martin, L., 1910. Alaskan earthquakes of 1899. Geological Society of America Bulletin 21 (1), 339-406.

Mayo, L., 1989. Advance of Hubbard Glacier and 1986 outburst of Russell Fiord, Alaska, U.S.A.. Annals of Glaciology 13.

McCalpin, J., 2009. Application of Paleoseismic Data and Seismic Hazard Assessment and Neotectonic Research. In: Paleoseismology. International Geophysics 95, 1-106. doi: 10.1016/S0074-6142(09)95009-4

McCalpin, J. and A. Nelson, 2009. Introduction to Paleoseismology. In: Paleoseismology. International Geophysics 95, 1-27. doi: 10.1016/S0074-6142(09)95001-X

McNabb, R., Hock, R. and M. Huss, 2015. Variations in Alaska tidewater glacier frontal ablation, 1985-2013. Journal of Geophysical Research 120 (1), 120-136.

McNabb, R., Hock, R., O'Neel, S., Rasmussen, L., Ahn, Y., Braun, M., Conway, H., Herreid, S., Joughin, I., Pfeffer, T., Smith, B. and M. Truffer, 2012. Using surface velocities to calculate ice thickness and bed topography: a case study at Columbia Glacier, Alaska, USA. Journal of Glaciology 58 (212), doi: 10.3189/2012JoG11J249.

Meier, M., Post, A., Krimmel, R. and C. Driedger, 1984. The 1983 Recession of Columbia Glacier. U.S. Geological Survey Open-file Report 84-059, https://pubs.usgs.gov/of/1984/0059/report.pdf

Meier, M., Rasmussen, L. and D. Miller, 1985. Columbia Glacier in 1984: Disintegration Underway. U.S. Geologic Survey Open-file Report 85-81, https://pubs.usgs.gov/of/1985/0081/report.pdf

Meier, M., Lundstrom, S., Stone, D., Kamb, B., Engelhardt, H., Humphrey, N., Dunlap, W., Fahenstock, M., Krimmel, R. and R. Walters, 1994. Mechanical and hydrologic basis for the rapid motion of a large tidewater glacier. Journal of Geophysical Research 99 (B8) 15,219-15,229.

Middleton, G. and M. Hampton, 1973. Sediment gravity flows: mechanics of flow and deposition. In: Middleton, G., Bouma, A., Turbidites and Deep Water Sedimentation. Soc. Econ. Paleontol. Mineral., Pac. Sect., Short Course, 1-38.

Migeon, S., Savoye, B., Zanella, E., Mulder, T., Faugères, J. and O. Weber, 2001. Detailed seismic-reflection and sedimentary study of trubidite sediment waves on the Var Sedimentary Ridge (SE France): significance for sediment transport and deposition and for the mechanisms of sediment-wave construction. Marine and Petroleum Geology 18 (2), 179-208.

Miller, E., 2014. High-resolution records of seismicity and seasonal sedimentation from Prince William Sound, Alaska, using XRF core scanning. School of Marine Science Master of Science thesis, Virginia Institute of Marine Science, College of William and Mary, Williamsburg, Virginia, 1-140.

Moffit, F., 1954. Geology of Prince William Sound region, Alaska, in Mineral resources of Alaska, 1951-53, U.S. Geol. Surv. Bull. 989-E, E225–E310.

Molnia, B. and J. Hein, 1982. Clay mineralogy of a glacially dominated, subarctic continental shelf: Northeastern Gulf of Alaska. Journal of Sedimentary Petrology 52, 515-527.

Mueller, C., Briggs, R., Wesson, R. and M. Petersen, 2015. Updating the USGS seismic hazard maps for Alaska. Quaternary Science Reviews 113, 39-47.

Mulder, T. and J. Syvitski, 1995. Turbidity Currents Generated at River Mouths during Exceptional Discharges to the World Oceans. The Journal of Geology 102 (3), 285-299.

Mulder, T., Savoye, B. and J. Syvitski, 1997. Numerical modelling of a mid-sized gravity flow: the 1979 Nice turbidity current (dynamics, processes, sediment budget and seafloor impact). Sedimentology 44, 305-326.

Mulder, T., Syvitski, J. and K. Skene, 1998. Modeling of Erosion and Deposition by Turbidity Currents Generated at River Mouths. Journal of Sedimentary Research 68 (1), 124-137.

Mulder, T., Migeon, S., Savoye, B. and J. Faugères, 2001. Inversely graded turbidite sequences in the deep Mediterranean: a record of deposits from flood-generated turbidity currents? Geo-Marine Letters 21, 86-93.

Mulder, T., Syvitski, J., Migeon, S., Faugères, J. and B. Savoye, 2003. Marine Hyperpycnal Flows: initiation, behavior and related deposits. A review. Marine and Petroleum Geology 20 (6-8), 861-882.

Mullenbach, B. and C. Nittrouer, 2000. Rapid Deposition of fluvial sediment in the Eel Canyon, northern California. Continental Shelf Research 20 (16), 2191-2212.

Mutti, E., Tinterri, R., Benevelli, G., Angella, S., di Baise, D. and G. Cavanna, 2003. Deltaic, mixed and turbidite sedimentation of ancient foreland basins. Marine and Petroleum Geology, 20 (6-8), 733-755.

Naidu, A., Freitag, G. and T. Mowatt, 1976. Clay minerals and recent sediments of the continental shelf, northern and western Gulf of Alaska. In Proceedings, Alaska Science Conference, 27th: Fairbanks, Alaska, v. II, Alaska Division of American Association for the Advancement of Science, University of Alaska, 202-212.

Neal, E., Walter, M. and C. Coffeen, 2002. Linking the pacific decadal oscillation to seasonal stream discharge patterns in Southeast Alaska. Journal of Hydrology 263, 188─197.

Nicolsky, D., Suleimani, E., Haeussler, P., Ryan, H., Koehler, R., Combellick, R. and R. Hansen, 2013. Tsunami Inundation Maps of Port Valdez, Alaska. State of Alaska, Department of Natural Resources. Report of Investigations 2013-1.

Niebauer, H., Royer, T. and T. Weingartner, 1994. Circulation of Prince William Sound, Alaska. Journal of Geophysical Research 99, 14,113-14,126.

Nittrouer, C., Sternberg, R., Carpenter, R. and J. Bennett, 1979. The use of Pb-210 geochronology as a sedimentological tool: application to the Washington continental shelf. Marine Geology 31, 297-316.

Nittrouer, C., DeMaster, D., McKee, B., Cutshall, N. and I. Larsen, 1984. The effect of sediment mixing on Pb-210 accumulation rates for the Washington continental shelf. Marine Geology 54 (3-4), 201-221.

NOAA, 2016. Prince William Sound, AK 8/3 arc-second MHHW DEM. Retrieved online from: http://www.ngdc.noaa.gov/dem/squareCellGrid/download/735.

Noda, A., TuZino, T., Kanai, Y., Furukawa, R. and J. Uchida, 2008. Paleoseismicity along the southern Kuril Trench deduced from submarine-fan turbidites. Marine Geology 254 (1-12), 73-90.

Normark, W., Posamentier, H. and E. Mutti, 1993. Turbidite systems: State of the art and future directions. Reviews of Geophysics 31 (2), 91-116.

O'Neel, S., Pfeffer, T., Krimmel, R. and M. Meier, 2005. Evolving force balance at Columbia Glacier, Alaska, during its rapid retreat. Journal of Geophysical Research: Earth Surface 110 (F3), doi: 10.1029/2005JF000292.

Overland, J., Adams, J. and N. Bond, 1999. Decadal variability of the Aleutian Low and its relation to high-latitude circulation. Journal of Climate 12, 1542-1547.

Pantini, H., 2001. Experimental evidence for autosuspension, in Particulate Gravity Currents. Edited by W. McCaffrey, B. Kneller, and J. Peakall. International Association of Sedimentology Special Publication 31.

Paulson, R., Chase, E., Roberts, R. and D. Moody, 1991. National Water Summary 1988─89 Hydrologic events and floods and droughts. U.S. Geological Survey Water Supply Paper 2375, 1-591, http://pubs.er.usgs.gov/publication/wsp2375.

Pfeffer, W., 2007. The opening of a New Landscape: Columbia Glacier at Mid-retreat. American Geophysical Union, Washington, DC.

Piper, D. and B. Savoye, 1993. Processes of late Quaternary turbidity current flow and deposition on the Var deepsea fan, north-west Mediterranean Sea. Sedimentology 40, 557-582.

Plafker, G., 1969. The Alaska Earthquake March 27, 1964: Regional Effects. U.S. Geologic Survey Professional Paper 543-1.

Plafker, G. and M. Rubin, 1978. Uplift history and earthquake recurrence as deduced from marine terraces on Middleton Island, Alaska. Proceedings of Converence VI, Methodology for identifying seismic gaps and soon-to-break gaps: U.S. Geological Survey Open-File Report 78-943, 687-721, http://dggs.alaska.gov/webpubs/usgs/of/text/of78-0943.pdf.

Plafker, G., Lajoie, K. and M. Rubin, 1992. Determining Recurrence Intervals of Great Subduction Zone Earthquakes in Southern Alaska by Radiocarbon Dating, in Radiocarbon After Four Decades: an Interdisciplinary Perspective, edited by R. Taylor, A. Long and R. Kra, 436-453.

Pondell, C., 2008. Organic Matter Analysis of sediments from Simpson Bay, Alaska using Elemental, Stable Isotopic, and Molecular Signatures. Office of Undergraduate Research, Senior Thesis, Texas A&M University, 1-54.

Post, A. and L. Mayo, 1971. Glacier Dammed Lakes and Outburst Floods in Alaska. Department of the Interior U.S. Geological Survey, Hydrologic Investigations Atlas HA-455, 1-10, https://pubs.usgs.gov/ha/455/report.pdf.

Rasmussen, L., Conway, H., Krimmel, R. and R. Hock, 2011. Surface mass balance, thinning and iceberg production, Columbia Glacier, Alaska, 1948-2007. Journal of Glaciology 57 (203), 431-440.

Rondionov, S., Overland, J. and N. Bond, 2005. The Aleutian Low and winter climatic conditions in the Bearing Sea. Part 1: Classification. Journal of Climate 18, 160-177.

Rothlisberger, H., 1972. Water pressure in intra- and subglacial channels. Journal of Glaciology 11 (62), 177-203.

Royer, T., 1979. On the effect of precipitation and runoff on coastal circulation in the Gulf of Alaska. Journal of Physical Oceanography 9, 555─563.

Ryan, H., Lee, H., Haeussler, P., Alexander, C. and R. Kayen, 2010. Historic and Paleo-Submarine Landslide Deposits Imaged Beneath Port Valdez, Alaska: Implications for Tsunami Generation in a Glacial Fiord, in: D. Mosher et al. (Eds.), Submarine Mass Movements and Their Consequences. Advances in Natural and Technological Hazards Research 28.

Ryan, H., von Huene, R., Wells, R., Scholl, D., Kirby, S. and A. Draut, 2011. History of Earthquakes and Tsunamis Along the Eastern Aleutian-Alaska Megathrust, with Implications for Tsunami Hazards in the California Continental Borderland. U.S. Geologic Survey Professional Paper 1795-A, http://pubs.usgs.gov/pp/1795/.

Schoch, G. and M. McCammon, 2013. Demonstrating the Alaska Ocean Observing System in Prince William Sound. Continental Shelf Research, doi:10.1016/j.csr.2011.12.011

Shanmugam, G., 1997. The Bouma Sequence and the turbidite mind set. Earth-Science Reviews 42, 201-229.

Sharma, G., 1979. The Alaskan Shelf: Hydrographic, Sedimentary and Geochemical Environment. Springer-Verlag New York Inc., 1-498.

Shennan, I. and S. Hamilton, 2006. Coseismic and pre-seismic subsidence associated with great earthquakes in Alaska. Quaternary Science Reviews 25 (1-2), 1-8.

Shennan, I., Long, A. and N. Barlow, 2007. Recurrent Holocene Paleoseismicity and Associated Land/Sea Level Changes in South Central Alaska. Department of Geography, University of Durham.

Shennan, I., Bruhn, R., Barlow, N., Good, K. and E. Hocking, 2014. Late Holocene great earthquakes in the eastern part of the Aleutian megathrust. Quaternary Science Reviews 84, 86-97.

Siegenthaler, C. and J. Buhler, 1985. The kinematics of turbulent suspension currents (turbidity currents) on inclined boundaries. Marine Geology 64, 19-40.

Sikonia, W. 1982. Finite Element Glacier Dynamics Model Applied to Columbia Glacier, Alaska. Geologic Survey Professional Paper 1258-B.

Singh, B. and C. Shah, 1971. Plunging phenomenon of density currents in reservoirs. La Houille Blanche 26, 59-64.

Stacey, M. and A. Bowen, 1988. The Vertical Structure of Density and turbidity Currents: Theory and Observations. Journal of Geophysical Research 93 (C4), 3528-3542.

Stocks, D., 1996. Prince William Sound, Alaska: Distal Depocenter for Copper River Sediment. College of William and Mary Bachelor of Science thesis, Williamsburg, Virginia, 1-44.

Stone, D., 1988. An investigation of the integrity of the Kadin lake ice dam. Senior thesis, University of Colorado, Boulder.

Syvitski, J., 1989. On the deposition of sediment within glacier-influenced fjords: Oceanographic controls. Marine Geology 85, 301-329.

Talling, P., 2014. On the triggers, resulting flow types and frequencies of subaqueous sediment density flows in different settings. Marine Geology 352, 155-182.

Trabant, D., March, R. and D. Thomas, 2003. Hubbard Glacier, Alaska: Growing and advancing in spite of global climate change and the 1986 and 2002 Russell Lake outburst floods. U.S. Geologic Survey Fact Sheet 001-03.

Trenberth, K. and J. Hurrell, 1994. Decadal atmosphere-ocean variations in the Pacific. Climate Dynamics 9, 303─319.

USGS, 2016. Earthquakes. Retrieved online from: http://earthquake.usgs.gov/earthquakes/

Vaughan, S., Mooers, C. and S. Gay, 2001. Physical variability in Prince William Sound during the SEA study (1994-98). Fisheries Oceanography 10 (1), 58-80.

Wendler, G., Galloway, K. and M. Stuefer, 2016. On the climate and climate change of Sitka, Southeast Alaska. Theoretical and Applied Climatology 126 (1-2), 27-34.

Walder, J. and J. Costa, 1996. Outburst floods from glacier-dammed lakes: the effect of mode of lake drainage on flood magnitude. Earth Surface Processes and Landforms 21, 701─723.

Walinsky, S., Prahl, F., Mix, A., Finney, B., Jaeger, J. and G. Rosen, 2009. Distribution and composition of organic matter in surface sediments of coastal Southeast Alaska. Continental Shelf Research 29, 1565-1579.

Wang, Y., Xue, H., Chai, F., Chao, Y. and J. Farrara, 2014. A model study of the Copper River plume and its effects on the northern Gulf of Alaska. Ocean Dynamics 64, 241─258.

Wang, X., Chao, Y., Zhang, H., Farrara, J., Li, Z., Jin, X., Park, K., Colas, F., McWilliams, J., Paternostro, C., Shum, C., Yi, Y., Schoch, C. and P. Olsson, 2013. Modeling tides and their influence on the circulation in Prince William Sound, Alaska. Continental Shelf Research 63, S126-S137.

Wesson, R., Boyd, O., Mueller, C., Bufe, C., Frankel, A. and M. Petersen, 2007. Revision of Time-Independent Probabilistic Seismic Hazard Maps for Alaska. U.S. Geological Survey Open File Report 2007-1043, https://pubs.usgs.gov/of/2007/1043/pdf/of07-1043_508.pdf

Winkler, G., 1976. Deepsea fan deposition of the lower tertiary Orca Group, eastern Prince William Sound, Alaska. U.S. Geological Survey Open File Report 76-83, 1-20, http://pubs.er.usgs.gov/publication/ofr7683.

Winkler, G., 2000. A geologic guide to Wrangell-Saint Elias National Park and Preserve, Alaska: a tectonic collage of northbound terranes. U.S. Geological Survey Professional Paper 1616, 1-58, https://pubs.usgs.gov/pp/p1616/P1616-508.pdf.

Wright, L. and C. Friedrichs, 2006. Gravity-driven sediment transport on continental shelves: a status report. Continental Shelf Research 26 (17-18), 2092-2107.

Zavala, C., Arcuri, M. and L. Blanco Valiente, 2012. The importance of plant remains as diagnostic criteria for the recognition of ancient hyperpycnites. Revue de Paléobiologie, Genève 11, 457-469.

TABLES

Core	Latitude	Longitude	Water Depth (m)
*PWS-07	60.30260	-146.75635	218
*PWS-08	60.37836	-146.79203	290
*PWS-09	60.43691	-146.81041	350
*PWS-10	60.50308	-146.96746	419
*PWS-12	60.67800	-146.90296	437
PWS-17	60.51273	-146.84250	422
PWS-18	60.61911	-146.83777	450
PWS-20	60.68938	-146.87027	426
PWS-22	60.73575	-146.93805	427
PWS-25	60.78943	-146.95305	379
PWS-28	60.93461	-147.09305	280

Table 1. Coordinates of coring locations for all cores in the N-S transect the central channel. Cores marked with an asterisk (*) were taken by Miller (2014).

Core	^{210}PB - LAR				^{137}Cs/^{239,240}Pu Peak			^{137}Cs/^{239,240}Pu Max Penetration			Average	Max	Min	Error
	cm yr^{-1}	+	-	R^2	cm yr^{-1}	+	-	cm yr^{-1}	+	-		cm yr^{-1}		
PWS-17	**1.20**	1.33	1.10	0.76	**1.27**	1.36	1.13	**1.38**	1.40	1.35	**1.28**	1.40	1.10	0.18
PWS-18*	**0.44**	0.51	0.38	0.94	**-**	-	-	**>2.46**	-	-	**-**	>2.46	0.44	1.01
PWS-20	**1.35**	1.41	1.30	0.92	**1.40**	1.44	1.33	**1.48**	1.52	1.43	**1.41**	1.52	1.30	0.11
PWS-22*	**0.99**	1.11	0.89	0.75	**0.98**	1.02	0.91	**0.99**	1.02	0.97	**0.99**	1.11	0.89	0.11
PWS-25	**0.69**	0.80	0.63	0.78	**-**	-	-	**0.85**	0.87	0.77	**0.77**	0.87	0.63	0.14

Table 2. ^{210}Pb linear sedimentation accumulation rates (LAR) calculated from the CF:CS model, the ^{137}Cs peaks and max penetration, and the average LAR. PWS-17 and PWS-18 were also analyzed for ^{239,240}Pu and the peak/max penetration depths match that of the ^{137}Cs. *PWS-18: The top 19 cm above the 1983 deposit were used to estimate the ^{210}Pb sedimentation rate. The maximum penetration of ^{137}Cs/^{239,240}Pu estimate used the core base, since low levels of ^{137}Cs and ^{239,240}Pu persist through the bottom. The error is the maximum difference between the average rate and the maximum/minimum of the range. *PWS-22: Calculated using sediment above the nil ^{137}Cs and low excess ^{210}Pb region (90cm, Fig. 21).

Core	Mean background K/Ca	Mean background Sr/Pb
PWS-17	0.27 ± 0.02	24.6 ± 3.7
PWS-18	0.28 ± 0.02	21.8 ± 3.2
PWS-20	0.28 ± 0.02	21.8 ± 3.6
PWS-22	0.31 ± 0.02	20.9 ± 3.2
PWS-25	0.37 ± 0.02	22.0 ± 3.8
PWS-28	0.68 ± 0.06	13.9 ± 1.9

Table 3. The whole-core mean K/Ca and Sr/Pb ratios in the background, which is defined as any sediment not part of a gravity flow deposit. Reported errors represent the standard deviation (1σ).

Core	%Sand	%Silt	%Clay	Mean(μm)
PWS-17	4.9 ± 1.8	57.3 ± 2.5	37.8 ± 2.5	18.1 ± 4.8
PWS-18	1.6 ± 0.9	59.7 ± 3.4	38.8 ± 3.1	11.3 ± 1.7
PWS-20	2.5 ± 2.0	59.1 ± 3.3	38.4 ± 2.0	13.6 ± 4.0
PWS-22	1.9 ± 1.3	56.2 ± 2.5	41.9 ± 2.0	11.6 ± 2.6
PWS-25	4.9 ± 1.7	49.9 ± 2.0	45.2 ± 2.3	31.7 ± 3.6
PWS-28	1.0 ± 2.1	41.9 ± 3.1	57.1 ± 3.8	8.1 ± 4.7

Table 4. The whole-core mean percentages of sand, silt, clay, and volume weighted mean grain size (μm) values in the background, which is defined as any sediment not part of a gravity flow deposit. Reported errors represent the standard deviation (1σ).

Core	$\delta^{13}C$	$\delta^{15}N$	C/N
PWS-07*	-24.33 ± 0.04	5.91 ± 0.12	14.5 ± 0.7
PWS-08*	-24.15 ± 0.04	5.34 ± 0.12	12.0 ± 0.5
PWS-09*	-23.77 ± 0.04	5.89 ± 0.12	10.33 ± 0.6
PWS-10	-24.34 ± 0.4	5.57 ± 0.3	11.40 ± 1.3
PWS-12	-23.74 ± 0.2	5.80 ± 0.4	10.27 ± 1.0
PWS-17	-23.44 ± 0.4	5.68 ± 0.2	10.78 ± 0.8
PWS-18	-23.50 ± 0.2	5.81 ± 0.4	10.3 ± 1.1
PWS-20	-23.77 ± 0.5	5.93 ± 0.2	10.63 ± 1.3
PWS-22	-23.74 ± 0.2	5.84 ± 0.2	10.39 ± 1.1
PWS-25	-23.67 ± 0.2	5.70 ± 0.2	10.20 ± 0.4
PWS-28	-24.87 ± 0.2	3.90 ± 0.3	8.40 ± 0.8

Table 5. The whole-core mean stable isotope values and C/N ratio in the background, which is defined as any sediment not part of a gravity flow deposit. Reported errors represent the standard deviation (1σ) . *PWS-(07, 08, 09) are values from surface layer samples only, thus are not core averaged.

Core	1983 Deposit		1964 Deposit		1928 Deposit		1912 Deposit		1899 Deposit	
	Depth	Age	Depth	Age	Depth	Age	Depth	Age	Depth	Age
PWS-09	-		70-80	**1979-74**	-		-		-	
PWS-10	25-28	**1989-86**	43-49	**1972-67**	80-90	**1930-24**	96-103	**1924-18**	-	
PWS-12	32-38	**1987-83**	63-70	**1964-59**	-		120-129	**1921-15**	140-149	**1906-99**
PWS-17	22-32	**1999-91**	52-67	**1976-64**	108-115	**1926-31**	133-147	**1912-01**	159-167	**1887-93**
PWS-18*	16-48	**1979**	70-	-	-		-		-	
PWS-20	34-48	**1994-82**	66-81	**1968-58**	-		-		-	
PWS-22	12-22	**2004-94**	34-46	**1982-70**	-		-		-	

Table 6. The depths and associated ages of each gravity flow deposit in central channel cores PWS-09 through PWS-22. Ages were calculated using the average sedimentation rates in Table 2. *The 1983 event in PWS-18 is dated by assuming the top 16 cm accumulated at a rate of 0.44 cm yr^{-1} since 1983.

FIGURES

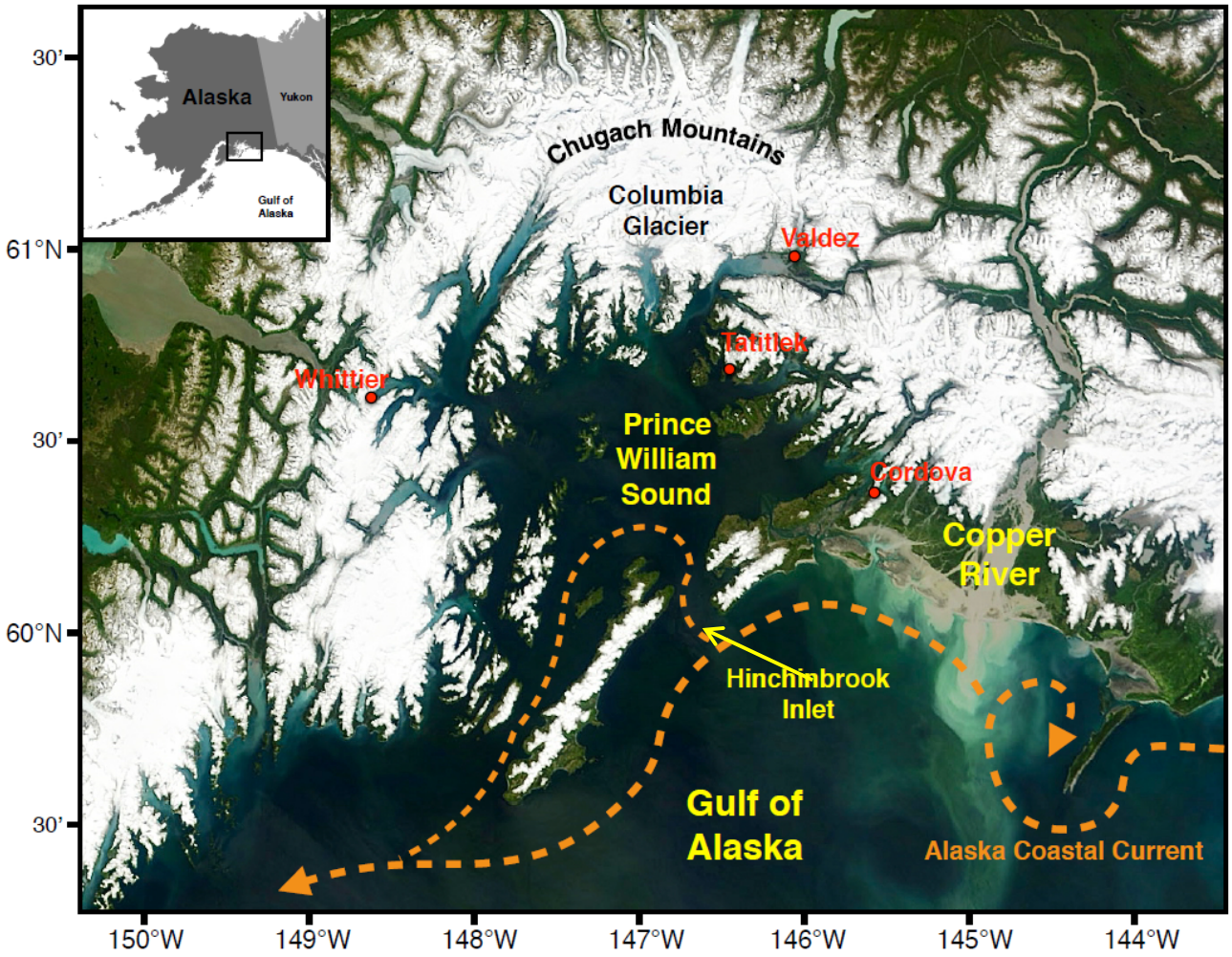

Figure 1. Map of Prince William Sound (PWS) and the coast of Alaska. The upper left inset shows the location of PWS within Alaska. Major bodies of water are labeled in yellow, towns are labeled in red, and the Chugach Mountains and glacier are labeled in black. The orange dashed line represents the generalized path of the Alaska Coastal Current (ACC).

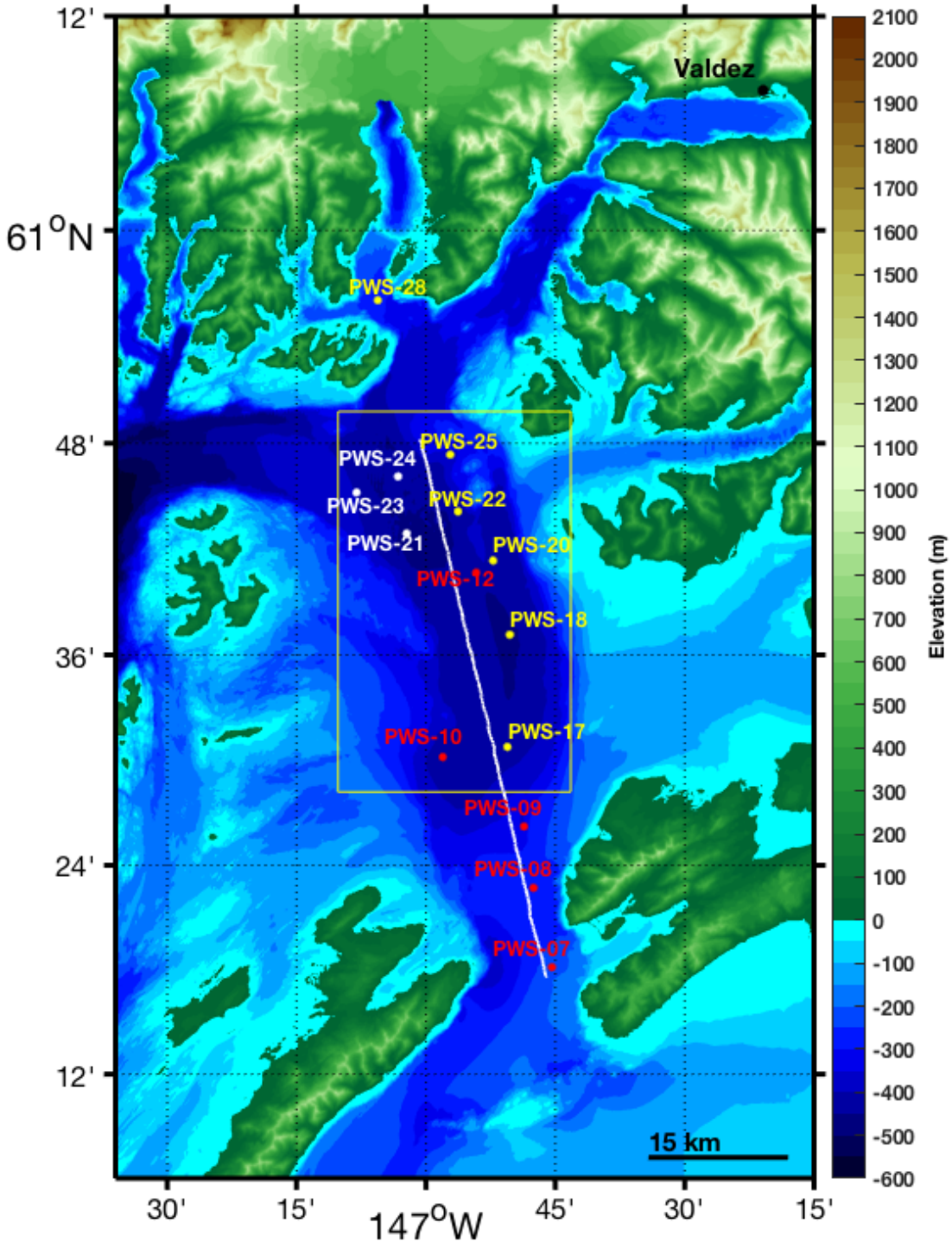

Figure 2. Topography and bathymetry of the PWS region showing successful core locations (yellow) and failed locations (white)from this study, and those of Miller (2014) (red). The upper left inset represents the location of the central channel within PWS. Cores PWS-10 through PWS-20 were taken in the central channel, PWS-22 and PWS-25 along the eastern flank, and PWS-28 near the mouth of Columbia Bay. CS4 (white line) is a seismic trackline profile (Liberty and Finn, 2013, Fig. 5). The yellow box outlines the area shown in Fig. 4. Bathymetry data from NOAA (2016).

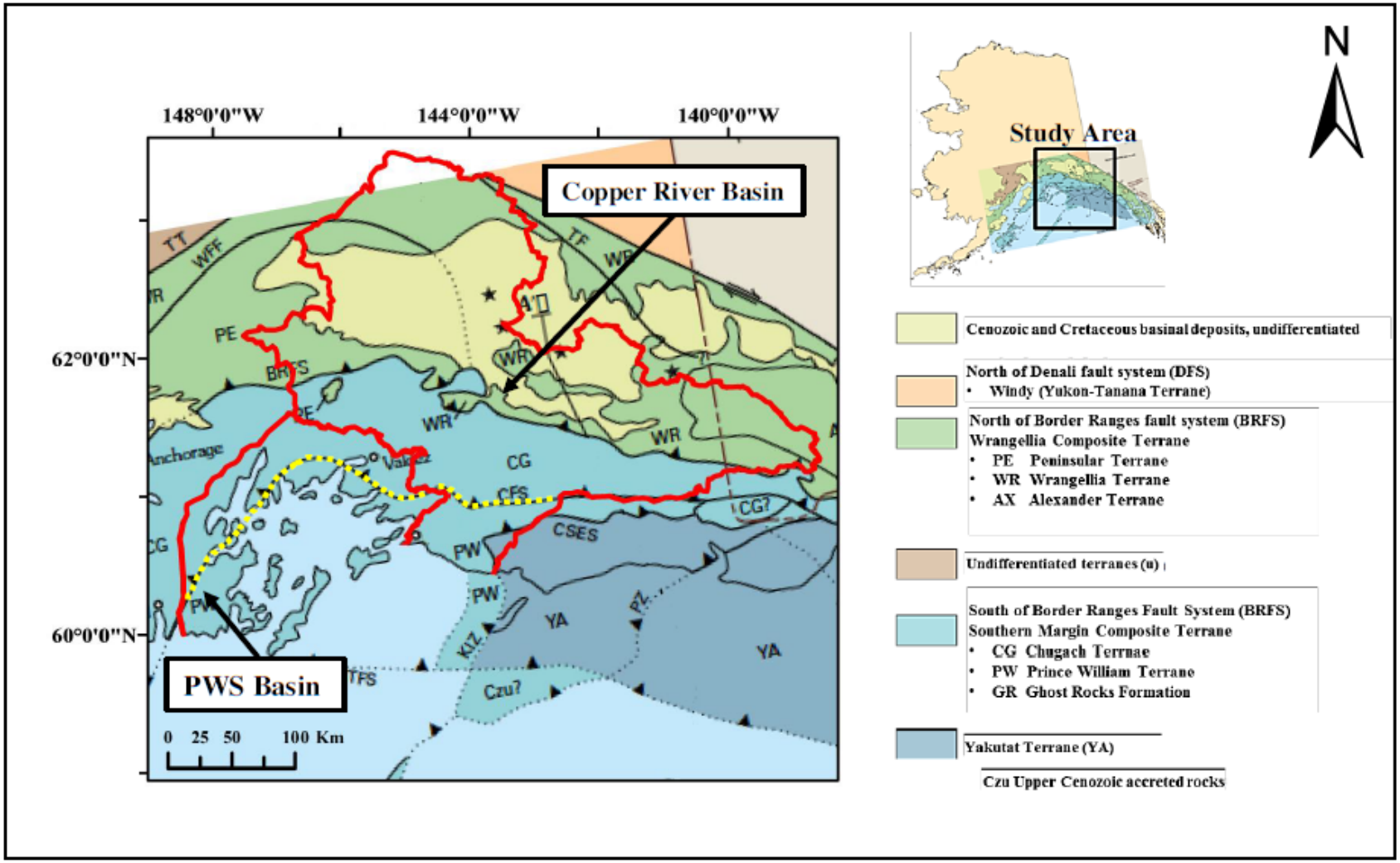

Figure 3. Map of the geologic terranes in PWS. The CR and PWS basins are outlined in red. The PWS basin is composed of Southern Margin Composite terrane (light blue), which is subdivided into Chugach Terrane (CG) and the Prince William Terrane (PW). Image modified from Winkler (2000).

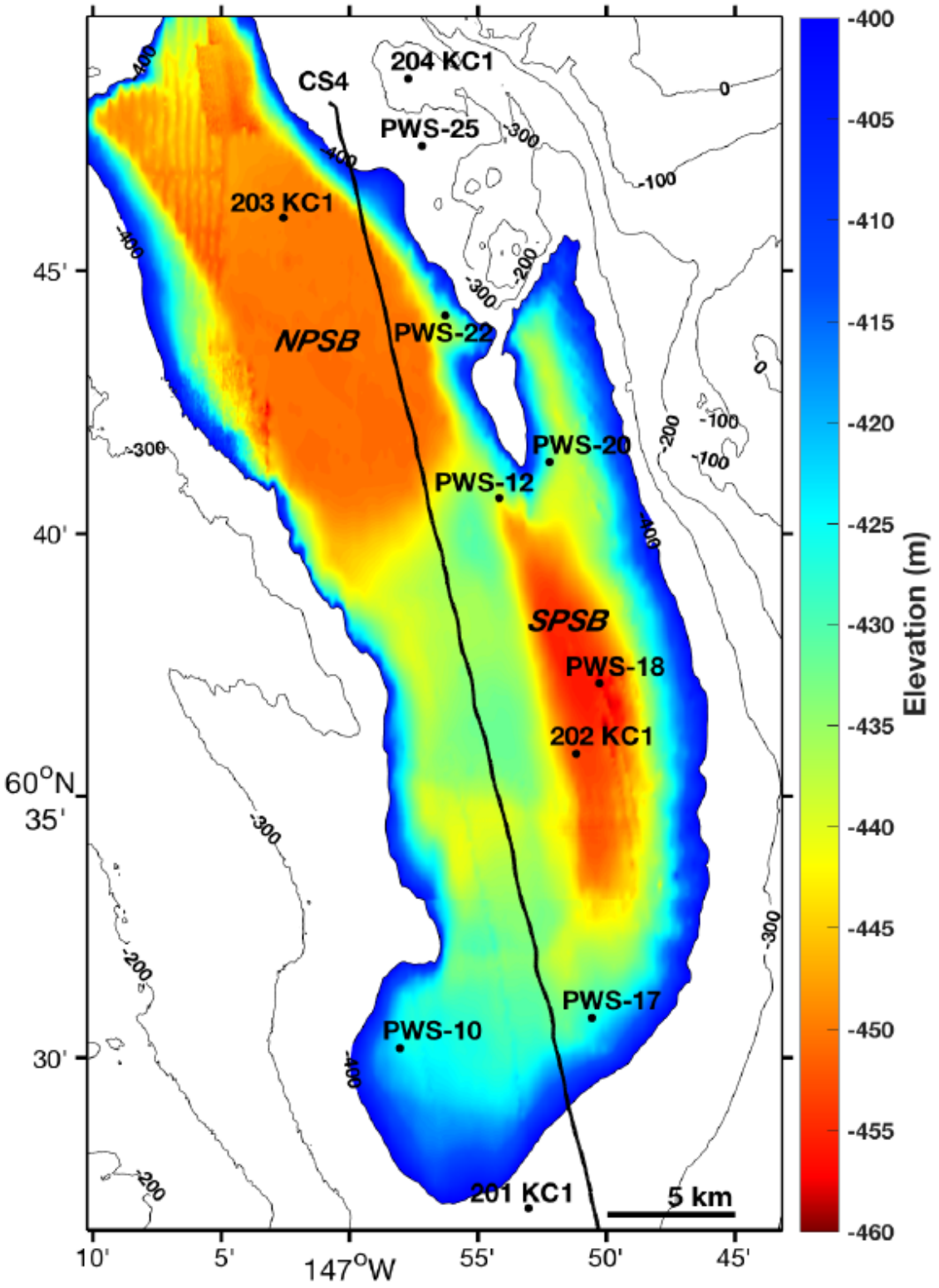

Figure 4. Bathymetric map of the PWS central channel from -400 m to -460 m below sea level. Any elevation above -400 m is white. The northern (NPSB) and southern (SPSB) ponded sediment basins are marked. Core locations and trackline CS4 (Liberty and Finn, 2013) are displayed in black. Included are cores 201-204 KC1 from Jaeger et al. (1998).

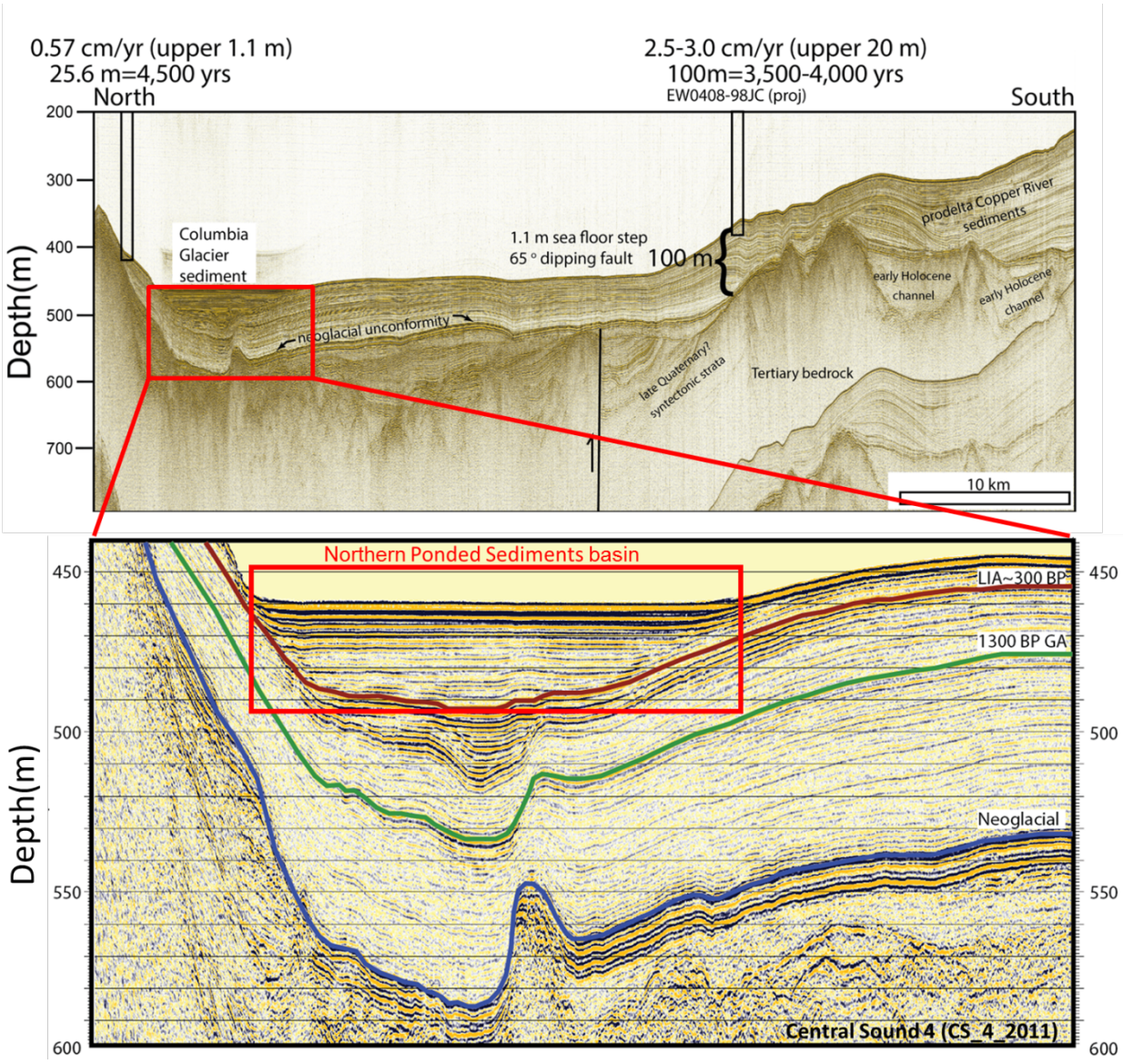

Figure 5. Seismic reflection profile CS4 (Liberty and Finn, 2013) (see Fig. 2 and 4) from PWS. Top image shows the entire CS4 transect. Foreset beds are visible on the southern end in HI. The bottom image is a close up of the northern ponded sediment basin, interpreted as Columbia Glacier derived sediments by Stocks (1996), Liberty and Finn (2013), and Finn et al. (2015). The Little Ice Age (LIA) ~300 year boundary in burgundy is extrapolated from the sedimentation rate in jumbo piston core EW0408-98JC (Finn et al., 2015 and references) along the CS4 trackline. The Neoglacial unconformity underlies ~100 m of Holocene sediments and has been interpreted to date from 3,500 to 4,000 years in EW0408-98JC, and 4,500 years by a northern sedimentation rate of 0.57 cmyr^{-1} from Klein (1983). Images courtesy of Lee Liberty (personal communication; Finn et al., 2015).

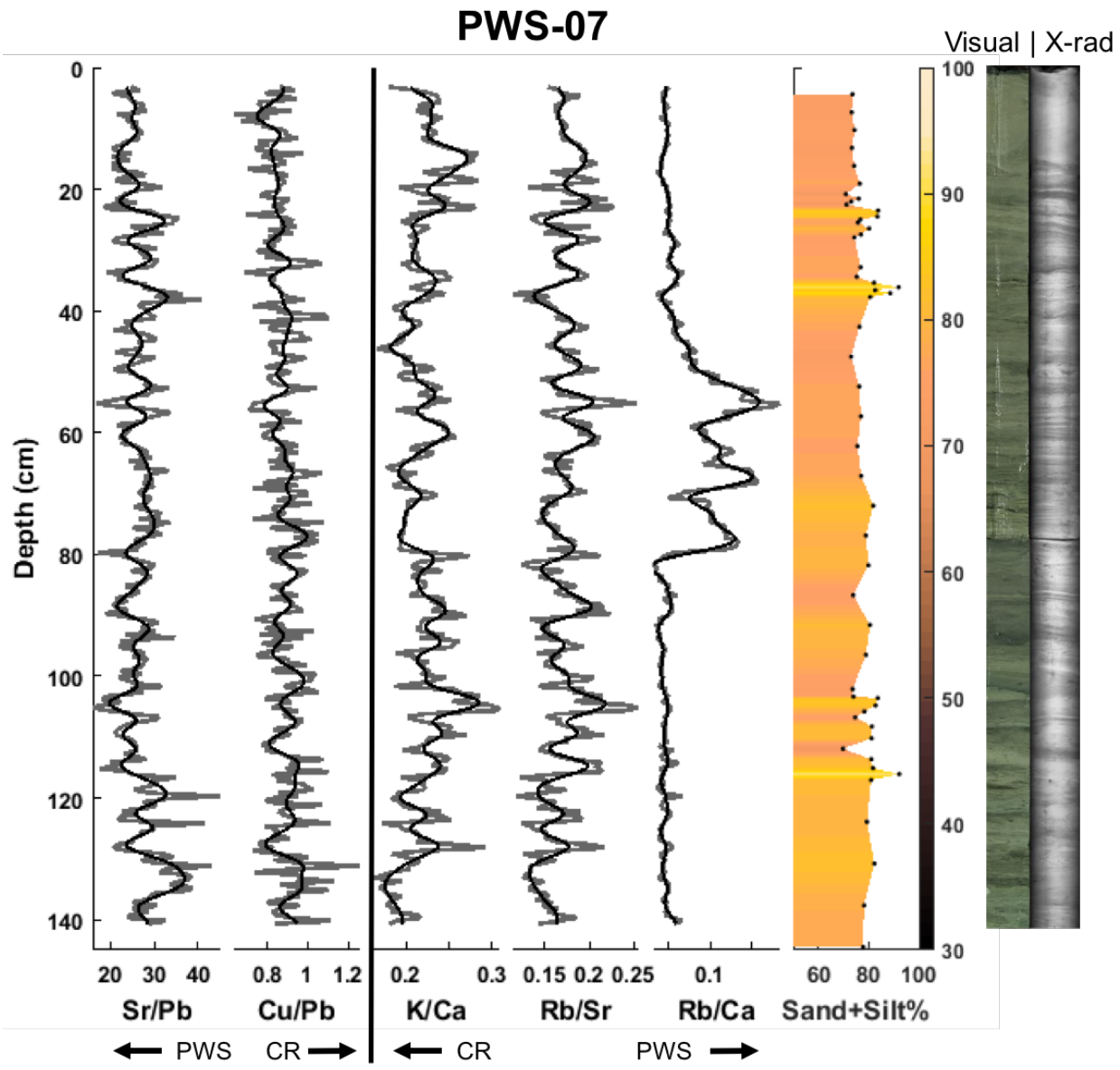

Figure 6. Visual and negative X-radiograph (shown on the right side) images of core PWS-07 aligned with XRF ratios Sr/Pb, Cu/Pb, K/Ca, Rb/Sr, and Rb/Ca and grain size. For the Sr/Pb and Cu/Pb ratios, a decrease in value indicates a more PWS signature while an increase indicates a stronger CR signature. The opposite is true for the K/Ca, Rb/Sr, and Rb/Ca signatures. The black line is the XRF data with a low pass filter applied. The visual (left) and X-radiograph (right; X-ray scan highlighting density changes) banding correspond to seasonal deposits from the CR plume and wintertime wave resuspension. The deposits around 55 and 85 cm date to 2001 and 1992 and are related to wave resuspension and increased CR discharge, respectively (Marshall, 2015). This core was the southernmost taken in HI by Miller (2014).

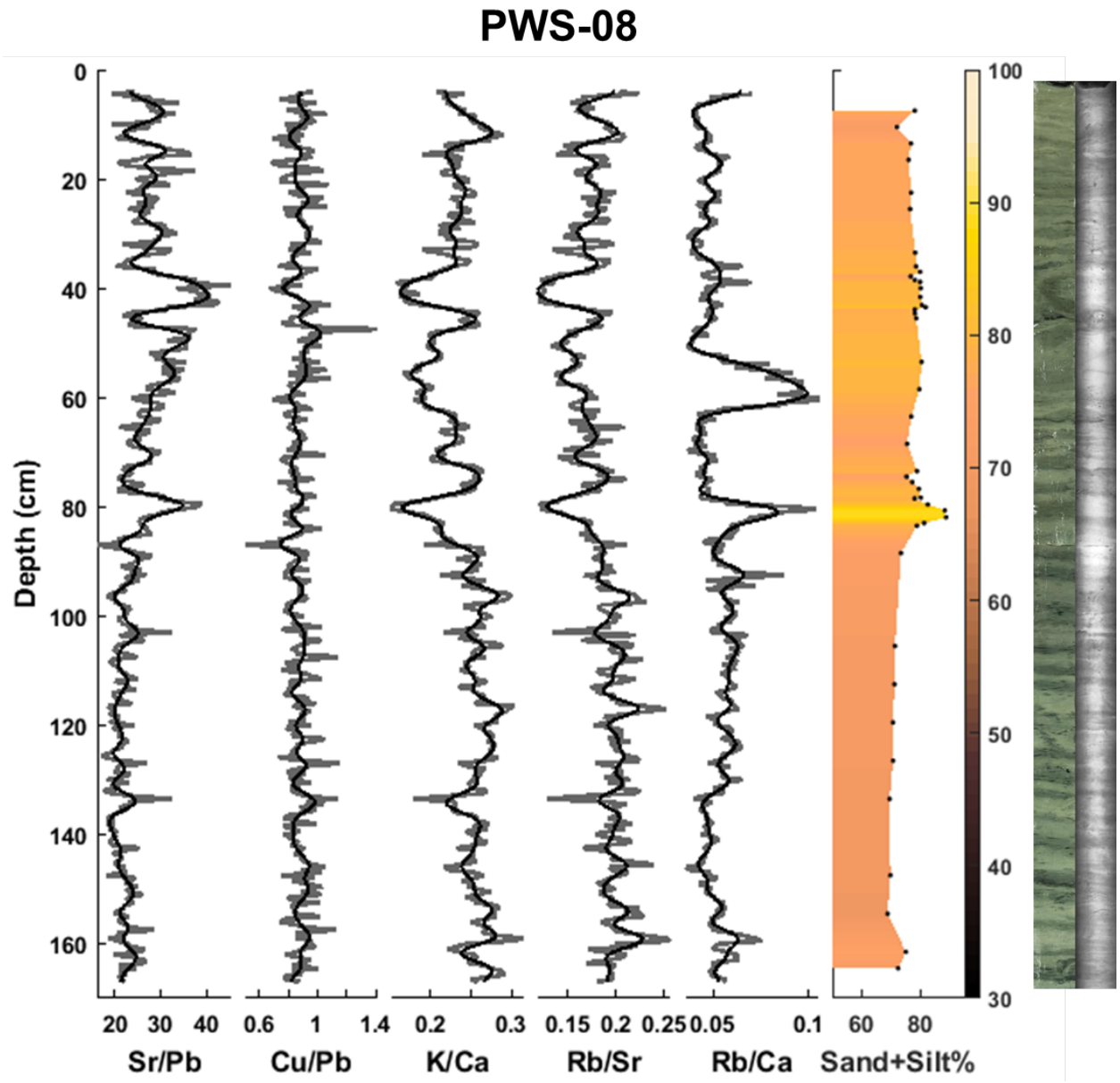

Figure 7. Visual and negative X-radiograph images of core PWS-08 aligned with XRF ratios Sr/Pb, Cu/Pb, K/Ca, Rb/Sr, and Rb/Ca and grain size. The visual and X-radiograph banding correspond to seasonal deposits from the CR plume and wintertime wave resuspension. The deposits near 45 and 80 cm date to 2001 and 1992 and are related to wave resuspension and increased CR discharge, respectively (Marshall, 2015). This core was taken in the north end of HI by Miller (2014).

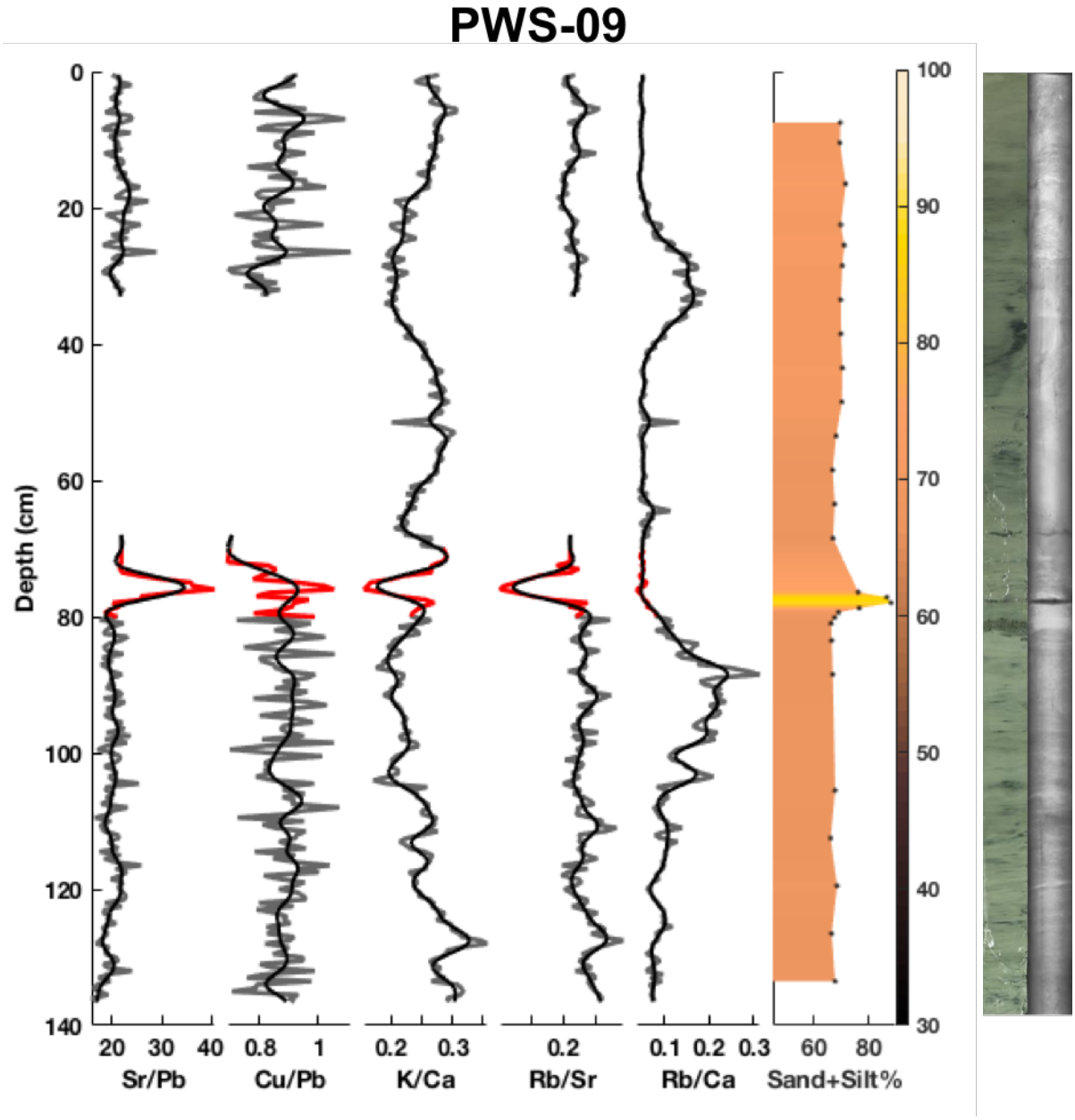

Figure 8. Visual and negative X-radiograph images of core PWS-09 aligned with XRF ratios Sr/Pb, Cu/Pb, K/Ca, Rb/Sr, and Rb/Ca and grain size. Note from ~30 – 70 cm the flat lines in three of the XRF ratios are due to an instrument failure during the 30kV scan. The dark band in the middle of the sandy deposit at 70 – 80 cm is an artifact from the core being cut in half. The 1964 inferred gravity flow deposit is highlighted in red. This core was taken north of HI by Miller (2014).

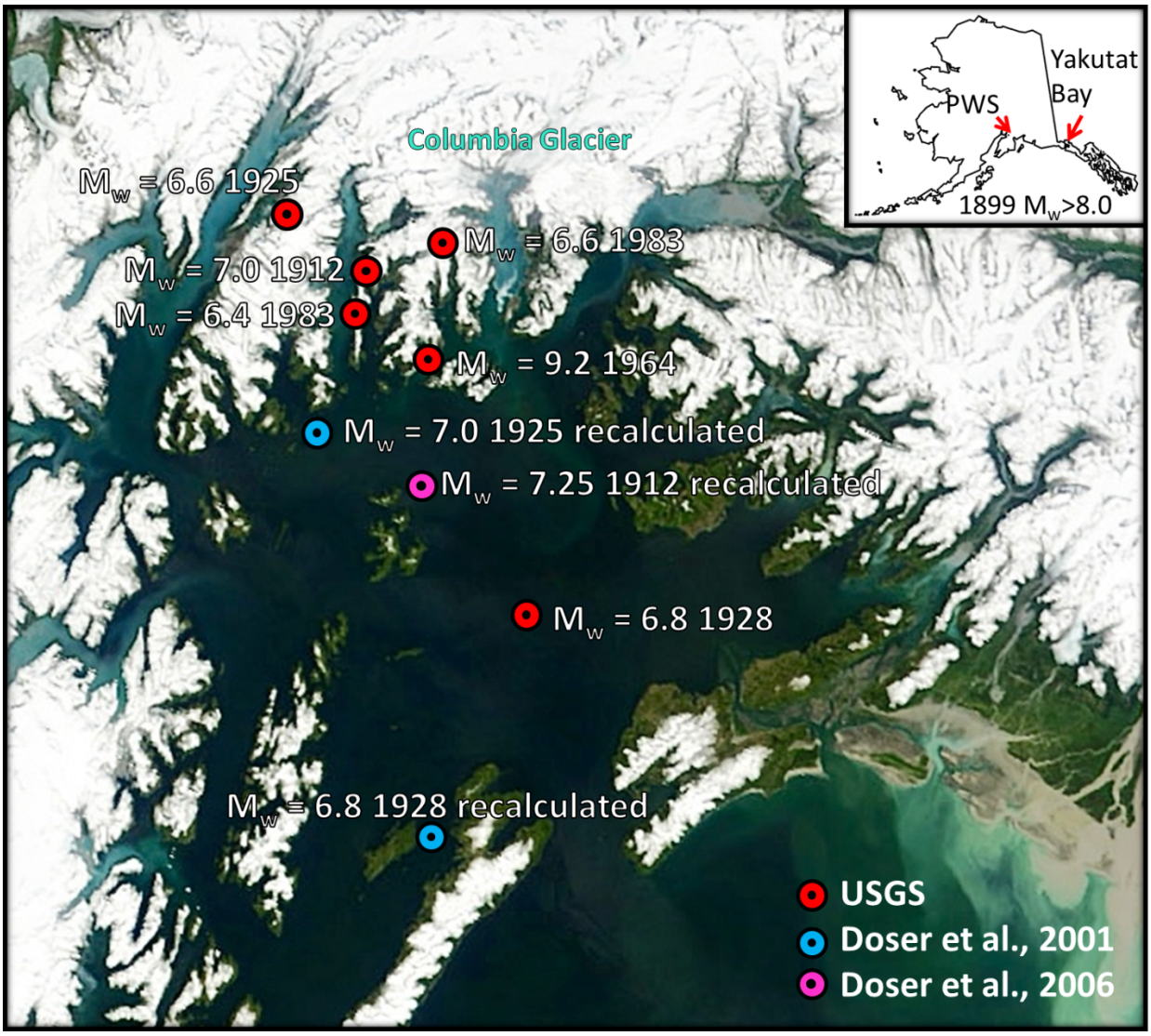

Figure 9. Map of epicenters and magnitudes of earthquakes with detected turbidites in PWS from the last 117 years. The upper right inset shows the relative location of the 1899 Yakutat earthquake, $M_w > 8.0$. The data for epicenters is from USGS (2016), Lander (1996), Doser et al. (2001) and Doser et al. (2006).

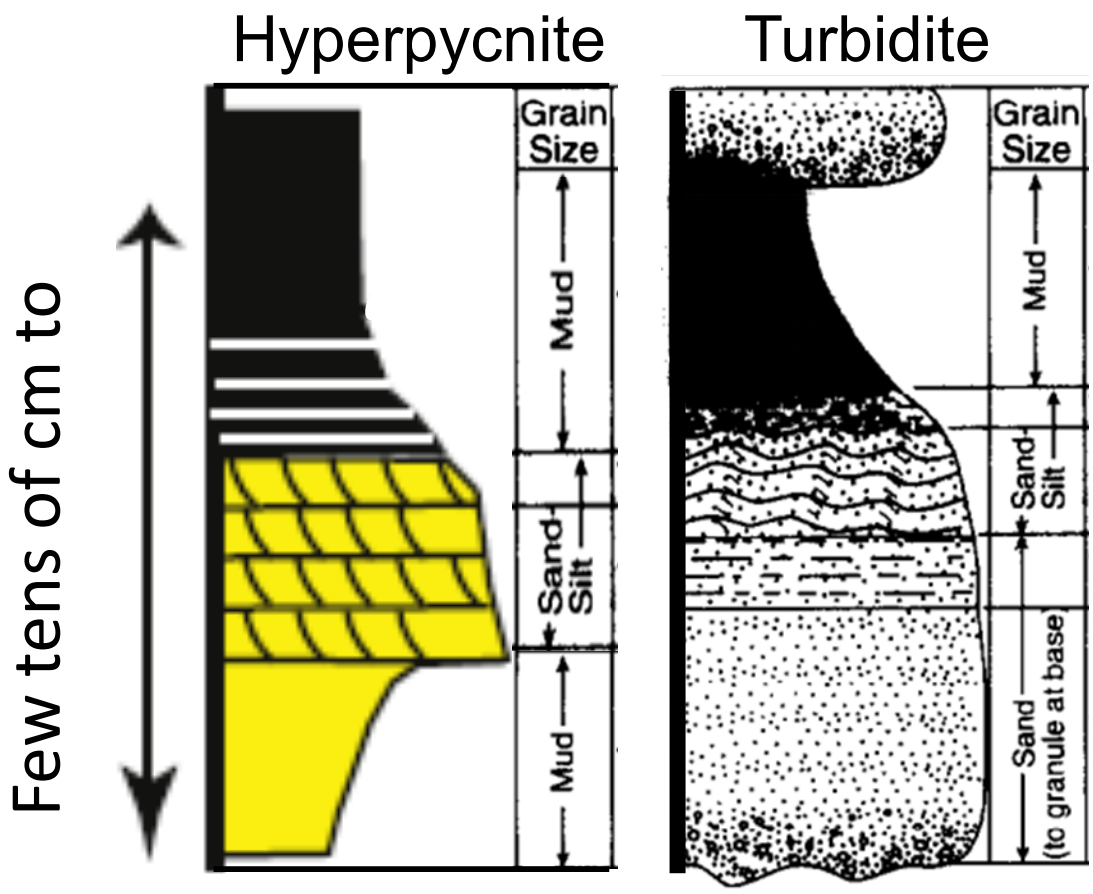

Figure 10. Right: Model of the idealized grain size structure of a surge-induced turbidity current deposit. The coarse base is deposited by the leading head, while the sand-silt and mud top are deposited during the main body and tail phases. Image modified from Shanmugam (1997). Left: Theoretical model of hyperpycnite grain size structure based on the model of Mulder et al. (2003). The coarsening upwards base is deposited during the waxing phase at the start of a hyperpycnal flow, while there fining upwards sequence is deposited after the peak velocity begins to wane. The contact between the top and bottom may be erosive. Image modified from Talling (2014).

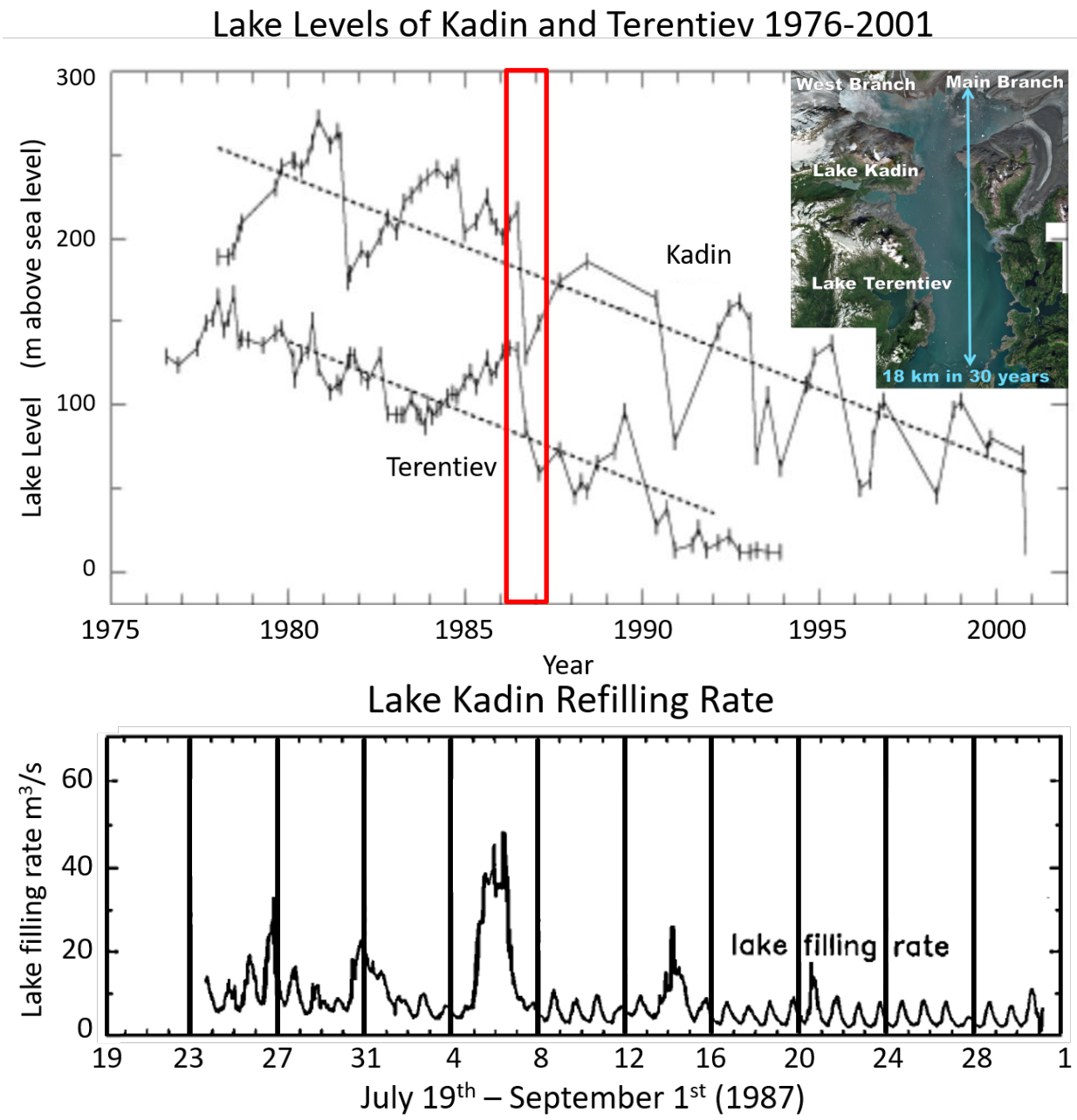

Figure 11. Top: Lake level graphs for Kadin and Terentiev. From early 1986 through early 1987 (red box) both lakes experienced a fall in lake level. Lake level data was gathered from aerial images taken on average every 2.5 months. Image modified from Krimmel (2001). Bottom: Measurements of lake Kadin filling rate. Maxima in filling are periods of rainfall or high wind events. The study period July 19th through August 31st 1987 (shown in red box in (A))occurred just after lake level fall events. Lake Kadin was gradually increasing stage into a temporary stable maximum lasting 2 years (1988-1990). Image modified from Meier et al (1994). Upper right inset: Satellite images retrieved March 2017 using the LandSat viewer. Lake Terentiev and Lake Kadin are visibly undammed by the glacier and are at stable water levels.

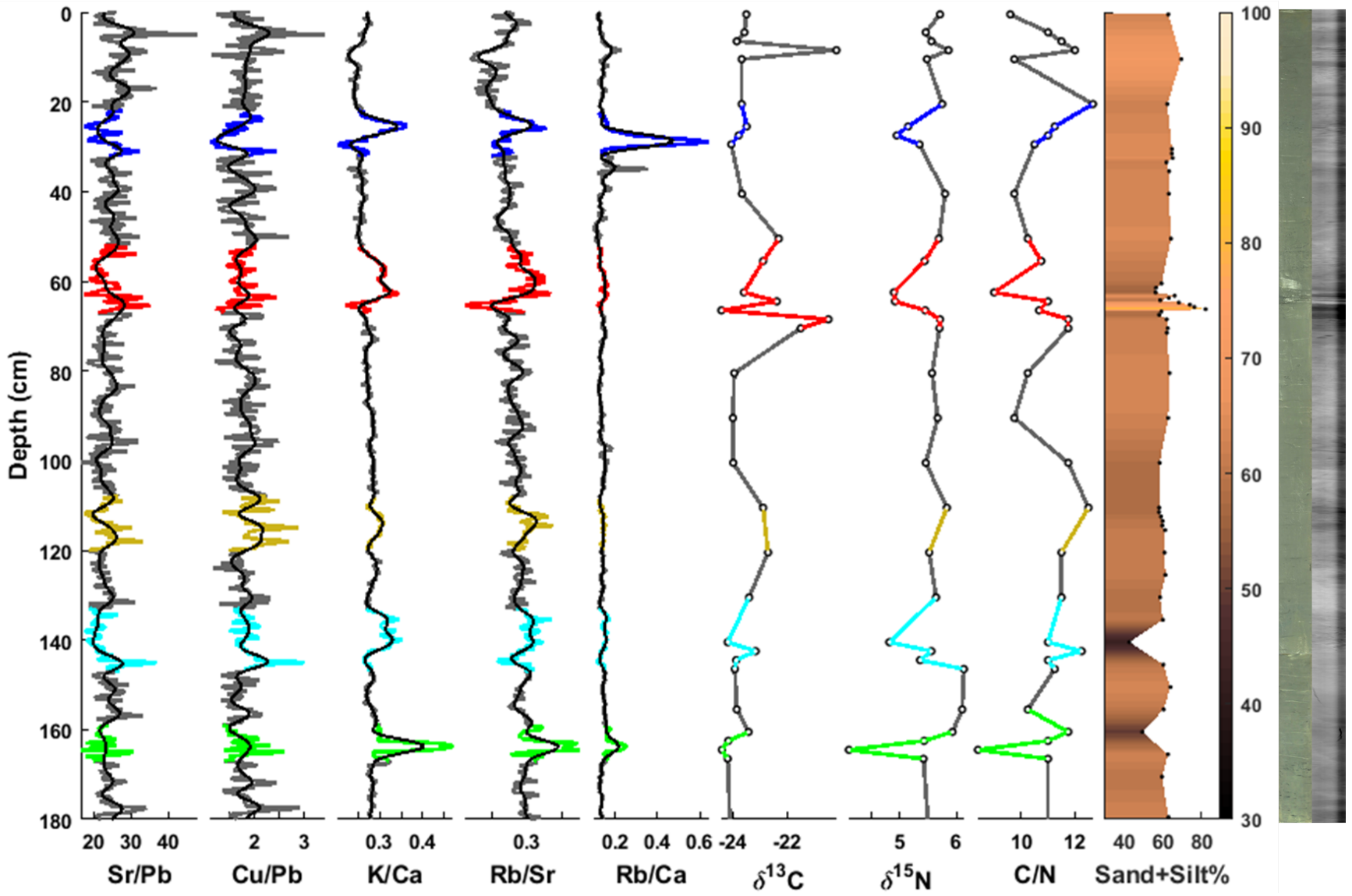
PWS-17
Depth (cm)
0
20
40
60
80
100
120
140
160
180
20 30 40
Sr/Pb
2 3
Cu/Pb
0.3 0.4
K/Ca
0.3
Rb/Sr
0.2 0.4 0.6
Rb/Ca
-24 -22
δ13C
5 6
δ15N
10 12
C/N
40 60 80
Sand+Silt%
100
90
80
70
60
50
40
30

Figure 12. From left to right: XRF ratios Sr/Pb, Cu/Pb, K/Ca, Rb/Sr, and Rb/Ca, $\delta^{13}C$, $\delta^{15}N$, C/N, and grain size data plotted alongside the visual/negative X-radiograph images of PWS-17. The 1983 (dark blue), 1964 (red), 1928 (yellow), 1912 (light blue), and 1899 (green) inferred sediment gravity flow deposits are highlighted. This core was collected in the southern end of the central channel in 2016.

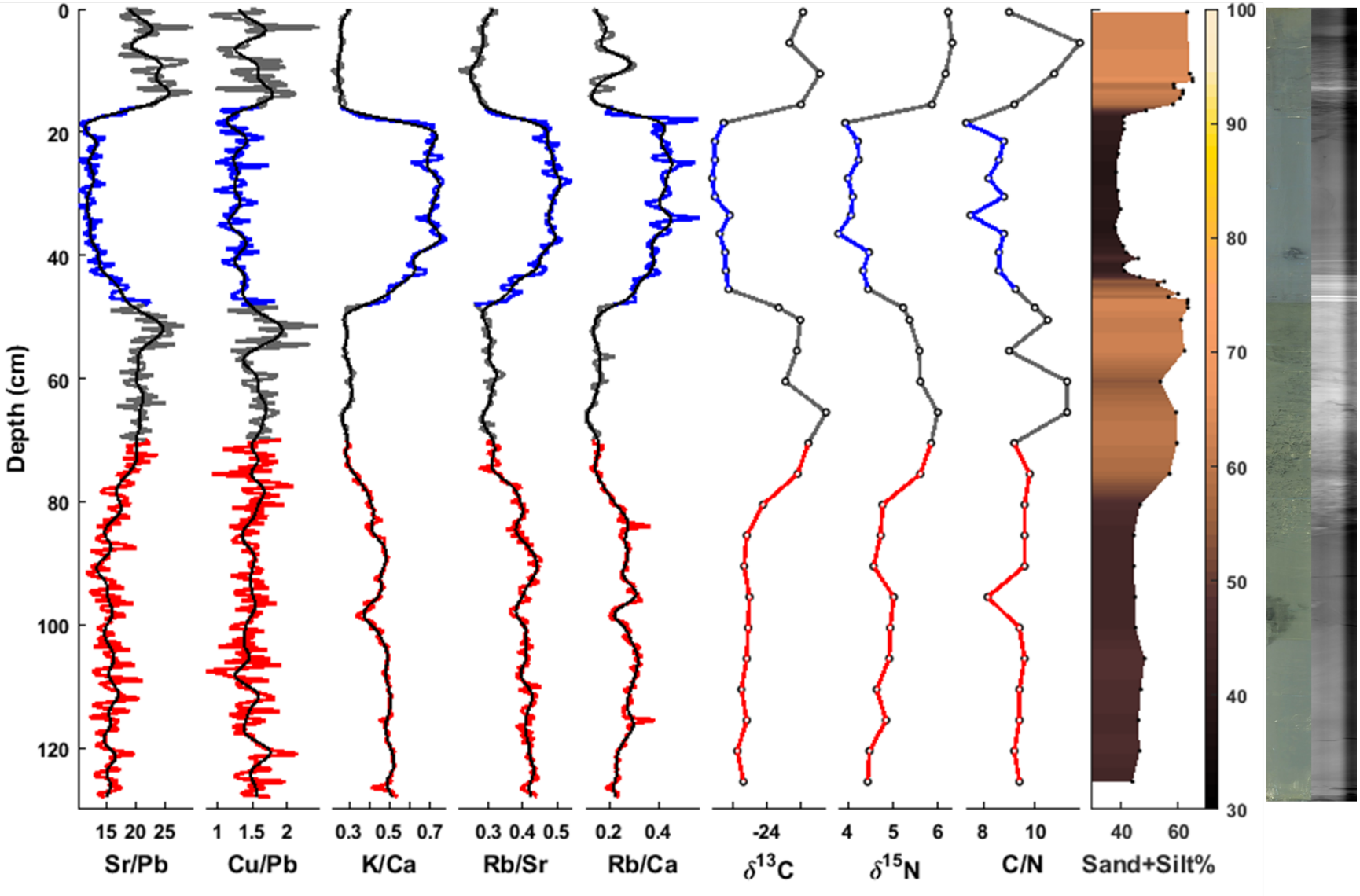
PWS-18
Depth (cm)
0
20
40
60
80
100
120
15 20 25
Sr/Pb
1 1.5 2
Cu/Pb
0.3 0.5 0.7
K/Ca
0.3 0.4 0.5
Rb/Sr
0.2 0.4
Rb/Ca
-24
δ13C
4 5 6
δ15N
8 10
C/N
40 60
Sand+Silt%
100
90
80
70
60
50
40
30

Figure 13. From left to right: XRF ratios Sr/Pb, Cu/Pb, K/Ca, Rb/Sr, and Rb/Ca, $\delta^{13}C$, $\delta^{15}N$, C/N, and grain size data plotted alongside the visual/negative X-radiograph images of PWS-18. The 1983 (dark blue) and 1964 (red) inferred sediment gravity flow deposits are highlighted. This core was collected in a deep (~455 m) basin in the central channel in 2016.

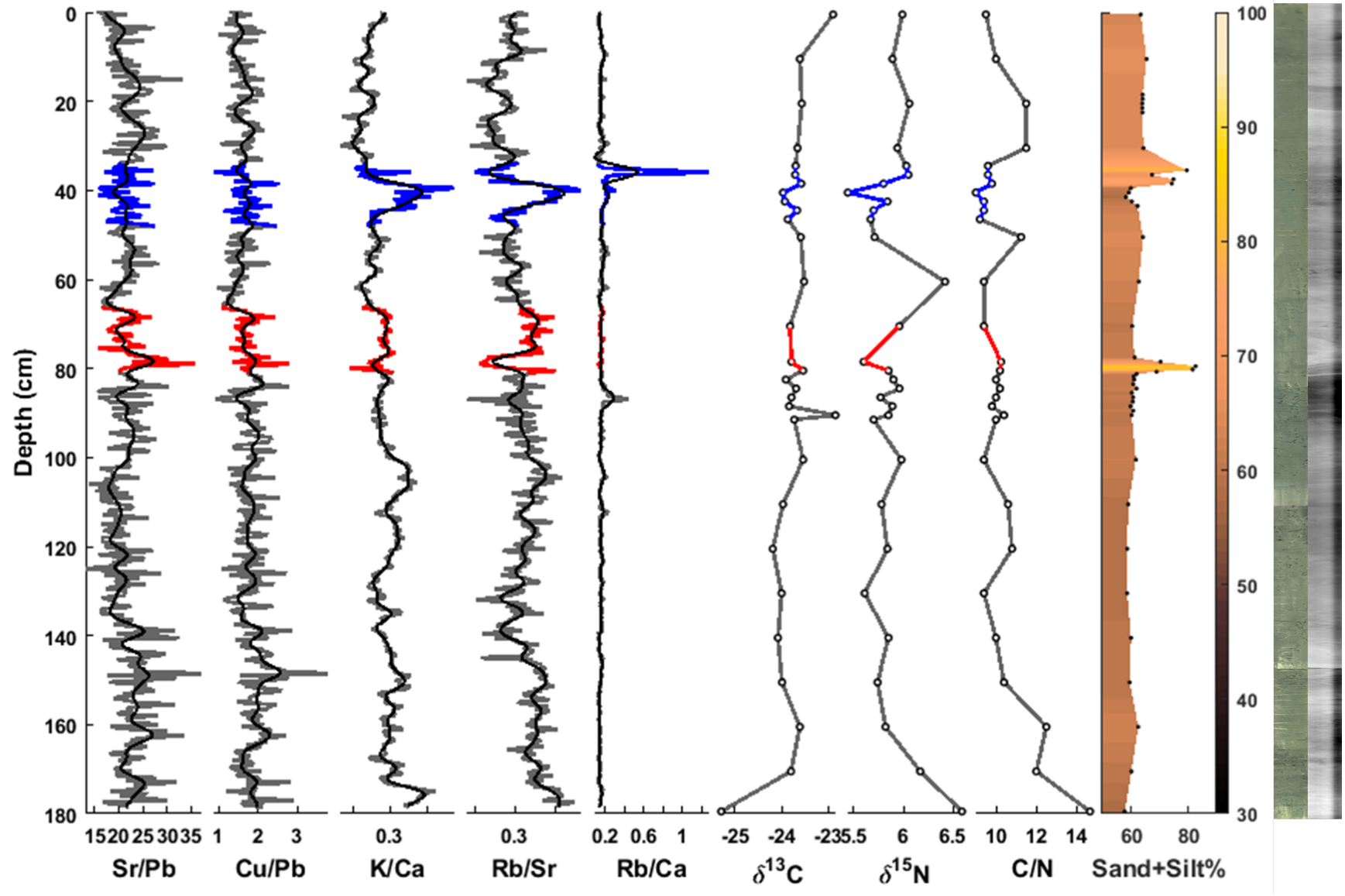
PWS-20
Depth (cm)
0
20
40
60
80
100
120
140
160
180
15 20 25 30 35
Sr/Pb
1 2 3
Cu/Pb
0.3
K/Ca
0.3
Rb/Sr
0.2 0.6 1
Rb/Ca
-25 -24 -23
$\delta^{13}C$
5.5 6 6.5
$\delta^{15}N$
10 12 14
C/N
60 80
Sand+Silt%
100
90
80
70
60
50
40
30

Figure 14. From left to right: XRF ratios Sr/Pb, Cu/Pb, K/Ca, Rb/Sr, and Rb/Ca, $\delta^{13}C$, $\delta^{15}N$, C/N, and grain size data plotted alongside the visual/negative X-radiograph images of PWS-20. The 1983 (dark blue) and 1964 (red) inferred sediment gravity flow deposits are highlighted. This core was collected in the central channel in 2016.

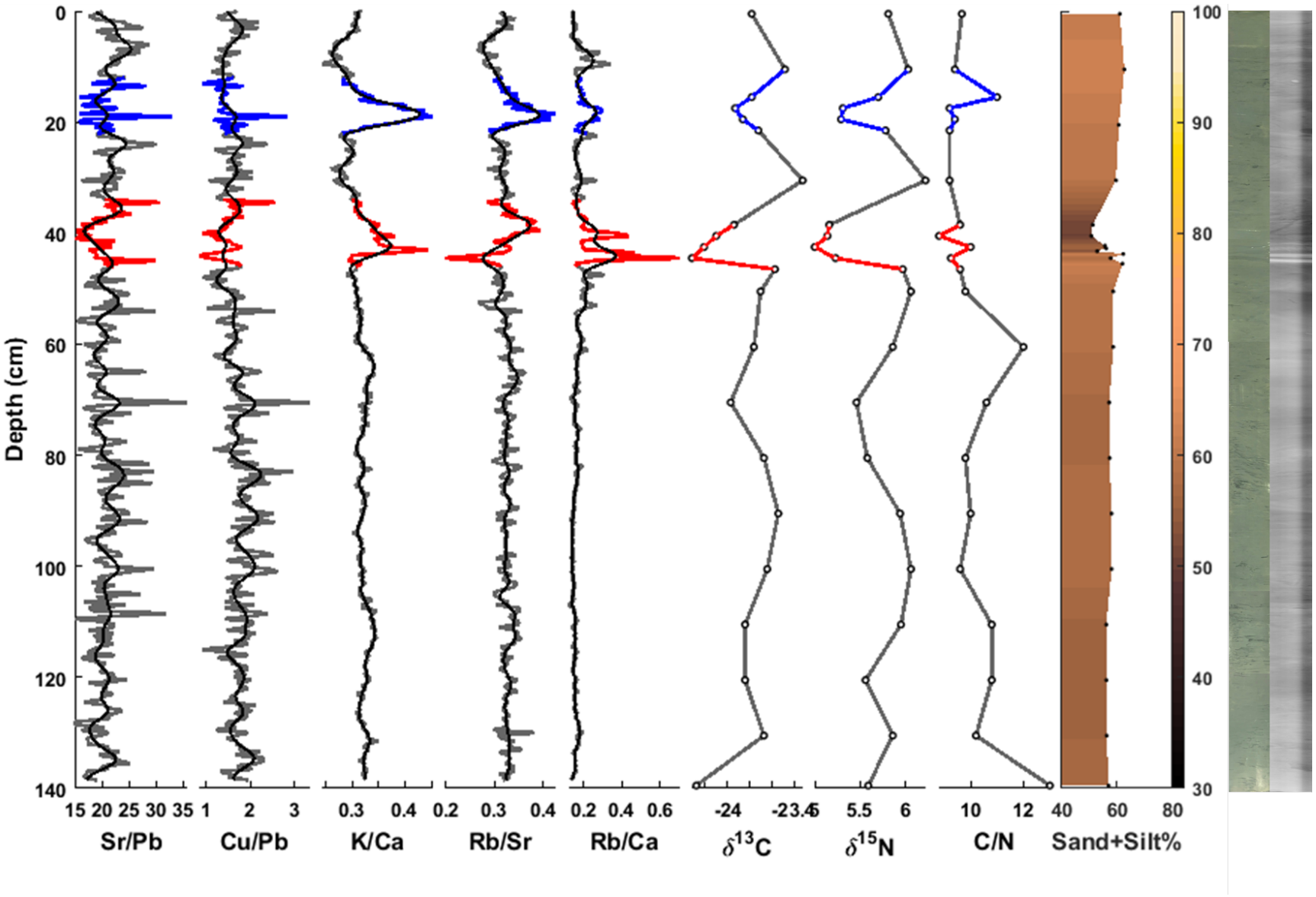
PWS-22
Depth (cm)
0
20
40
60
80
100
120
140
15 20 25 30 35
Sr/Pb
1 2 3
Cu/Pb
0.3 0.4
K/Ca
0.2 0.3 0.4
Rb/Sr
0.2 0.4 0.6
Rb/Ca
-24 -23.5
δ13C
5 5.5 6
δ15N
10 12
C/N
40 60 80
Sand+Silt%
100
90
80
70
60
50
40
30

Figure 15. From left to right: XRF ratios Sr/Pb, Cu/Pb, K/Ca, Rb/Sr, and Rb/Ca, $\delta^{13}C$, $\delta^{15}N$, C/N, and grain size data plotted alongside the visual/negative X-radiograph images of PWS-22. The 1983 (dark blue) and 1964 (red) inferred sediment gravity flow deposits are highlighted. This core was collected at the base of the eastern flank of the central channel in 2016.

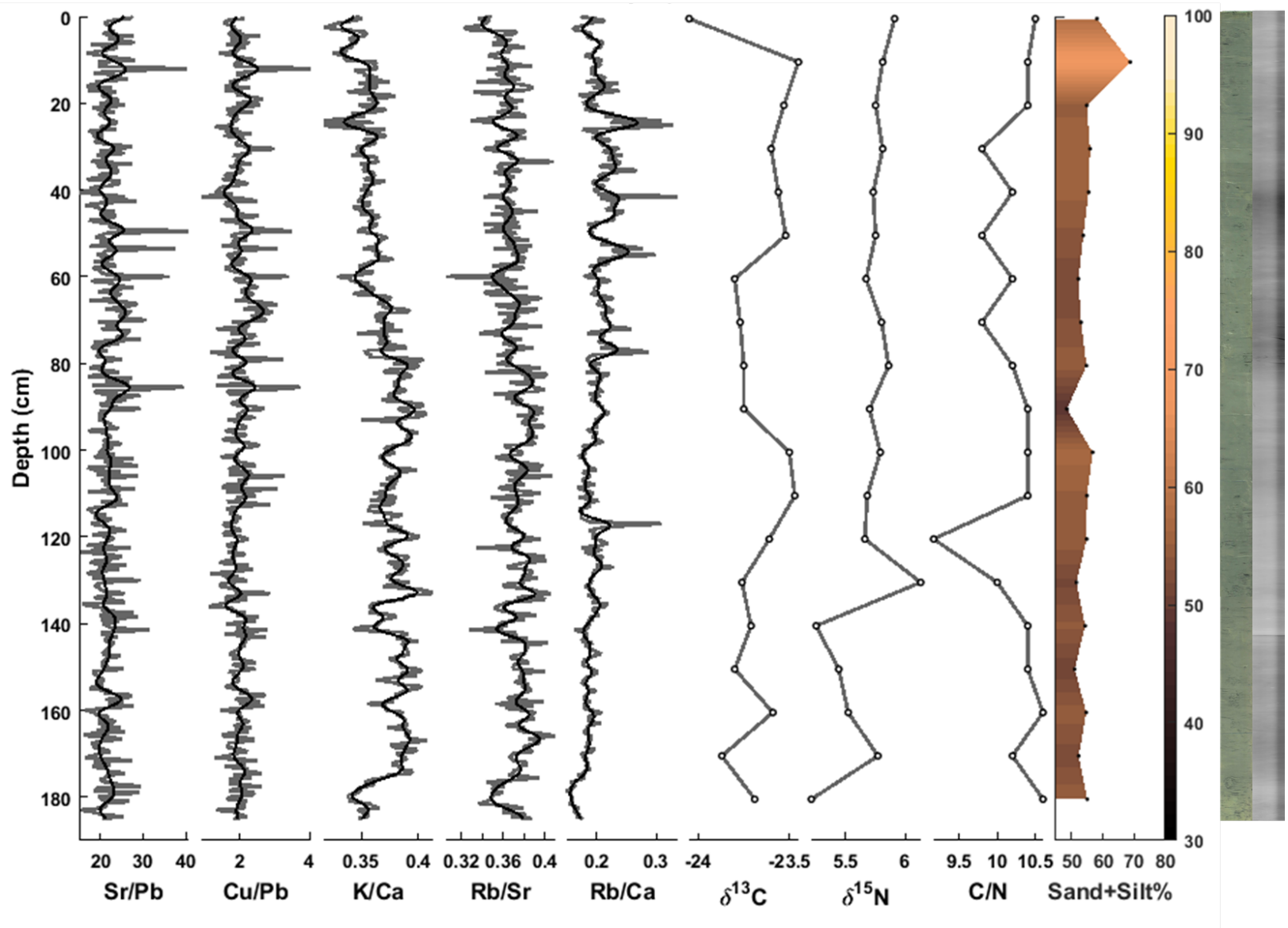
PWS-25
Depth (cm)
0
20
40
60
80
100
120
140
160
180
20 30 40
Sr/Pb
2 4
Cu/Pb
0.35 0.4
K/Ca
0.32 0.36 0.4
Rb/Sr
0.2 0.3
Rb/Ca
-24 -23.5
δ13C
5.5 6
δ15N
9.5 10 10.5
C/N
50 60 70 80
Sand+Silt%
100
90
80
70
60
50
40
30

Figure 16. From left to right: XRF ratios Sr/Pb, Cu/Pb, K/Ca, Rb/Sr, and Rb/Ca, $\delta^{13}C$, $\delta^{15}N$, C/N, and grain size data plotted alongside the visual/negative X-radiograph images of PWS-25. This core was collected on the eastern flank of the central channel in 2016.

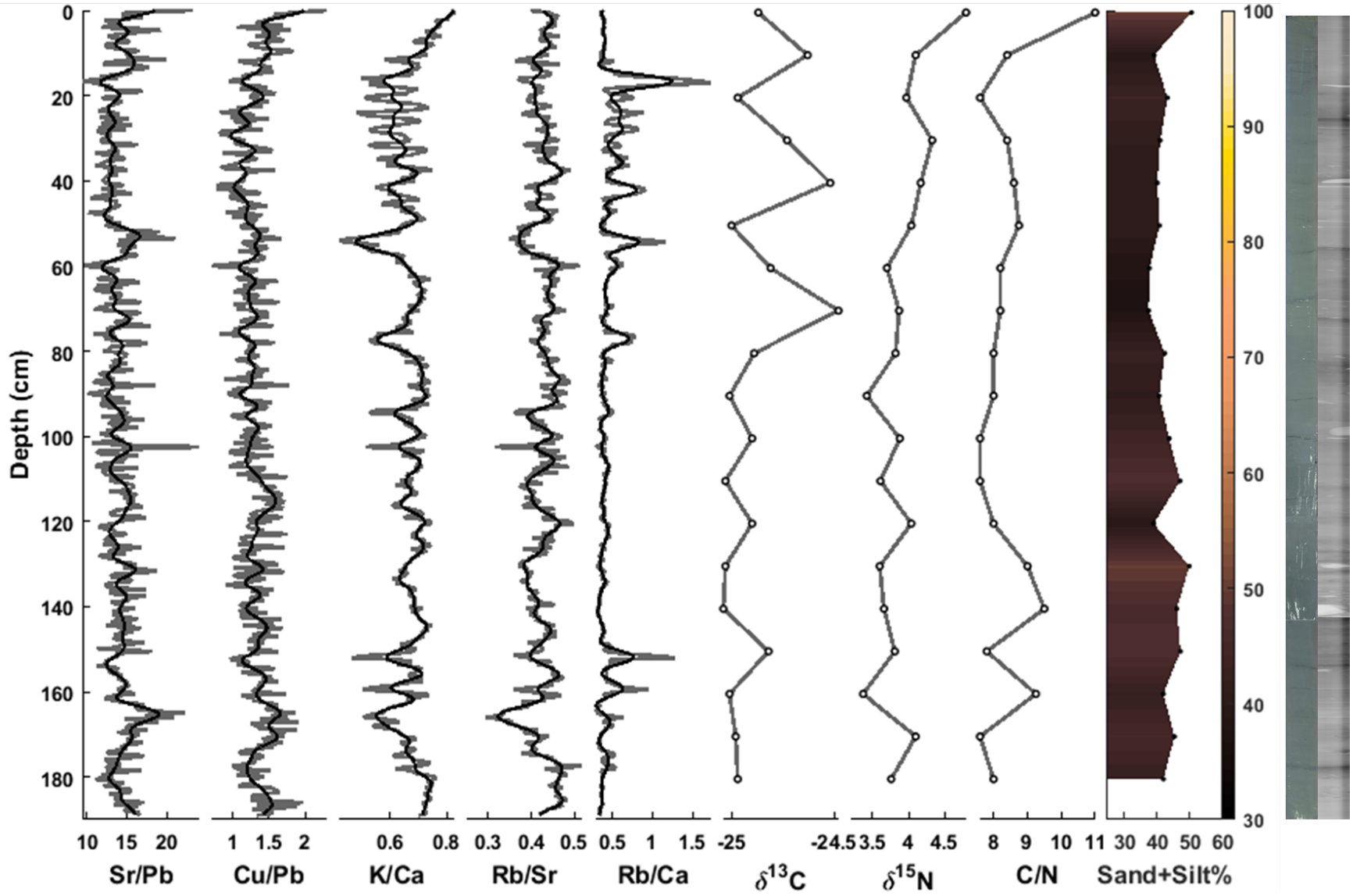
PWS-28
Depth (cm)
0
20
40
60
80
100
120
140
160
180
10 15 20
Sr/Pb
1 1.5 2
Cu/Pb
0.6 0.8
K/Ca
0.3 0.4 0.5
Rb/Sr
0.5 1 1.5
Rb/Ca
-25 -24.5
δ13C
3.5 4 4.5
δ15N
8 9 10 11
C/N
30 40 50 60
Sand+Silt%
100
90
80
70
60
50
40
30

Figure 17. From left to right: XRF ratios Sr/Pb, Cu/Pb, K/Ca, Rb/Sr, and Rb/Ca, $\delta^{13}C$, $\delta^{15}N$, C/N, and grain size data plotted alongside the visual/negative X-radiograph images of PWS-28. This core was collected near the mouth of Columbia Bay in 2016.

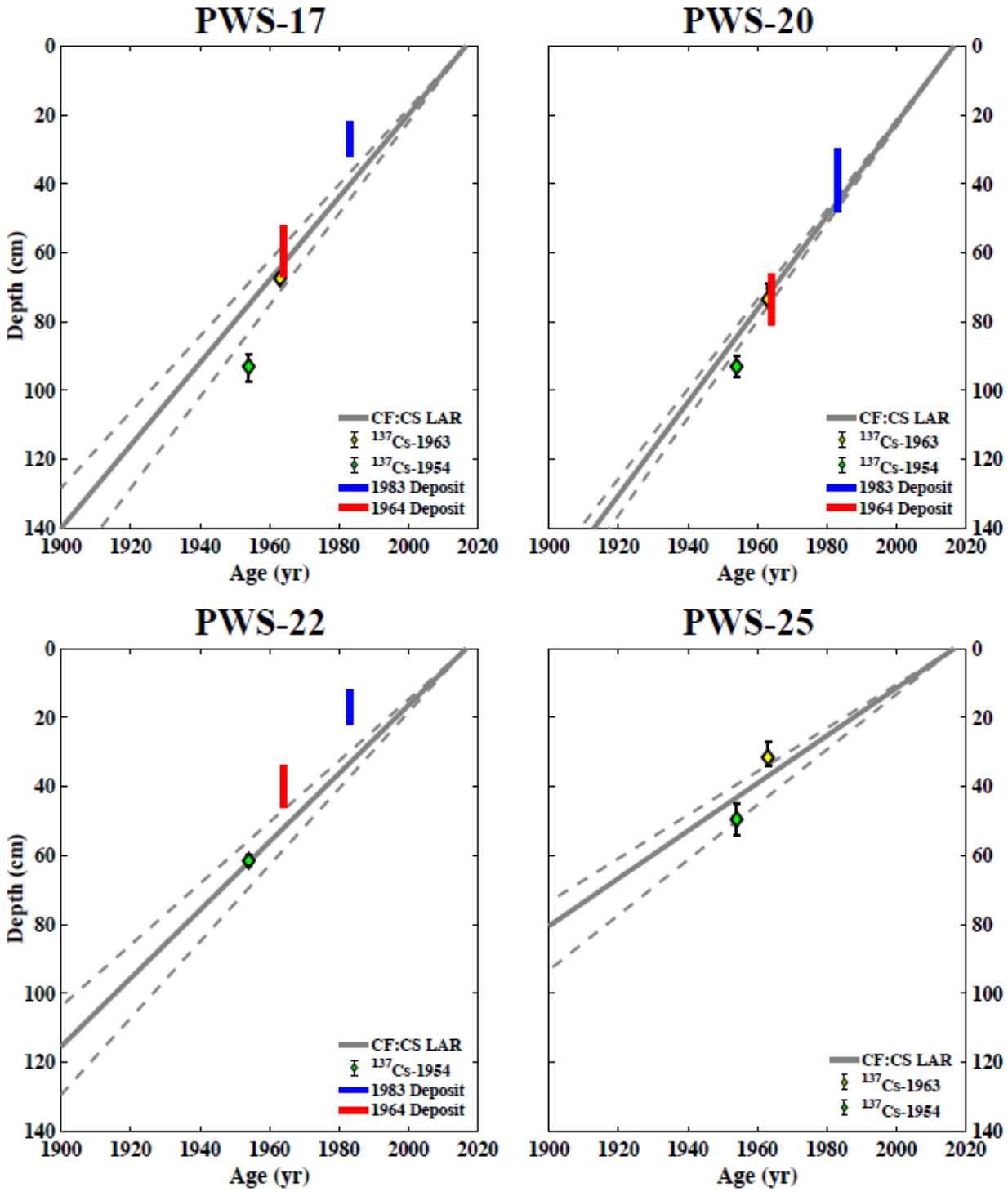

Figure 18. Age models of PWS-(17, 20, 22, 25) plotted using the ^{210}Pb Linear Accumulation Rate (LAR) derived from the CF:CS model in Table 2 as depth (cm) versus year. The span of the 1983 and 1964 deposits and the location of the ^{137}Cs peak and first appearance are plotted for reference, where applicable. The dashed lines represent the highest/lowest possible rates derived from the least squares of the standard error from regression analysis.

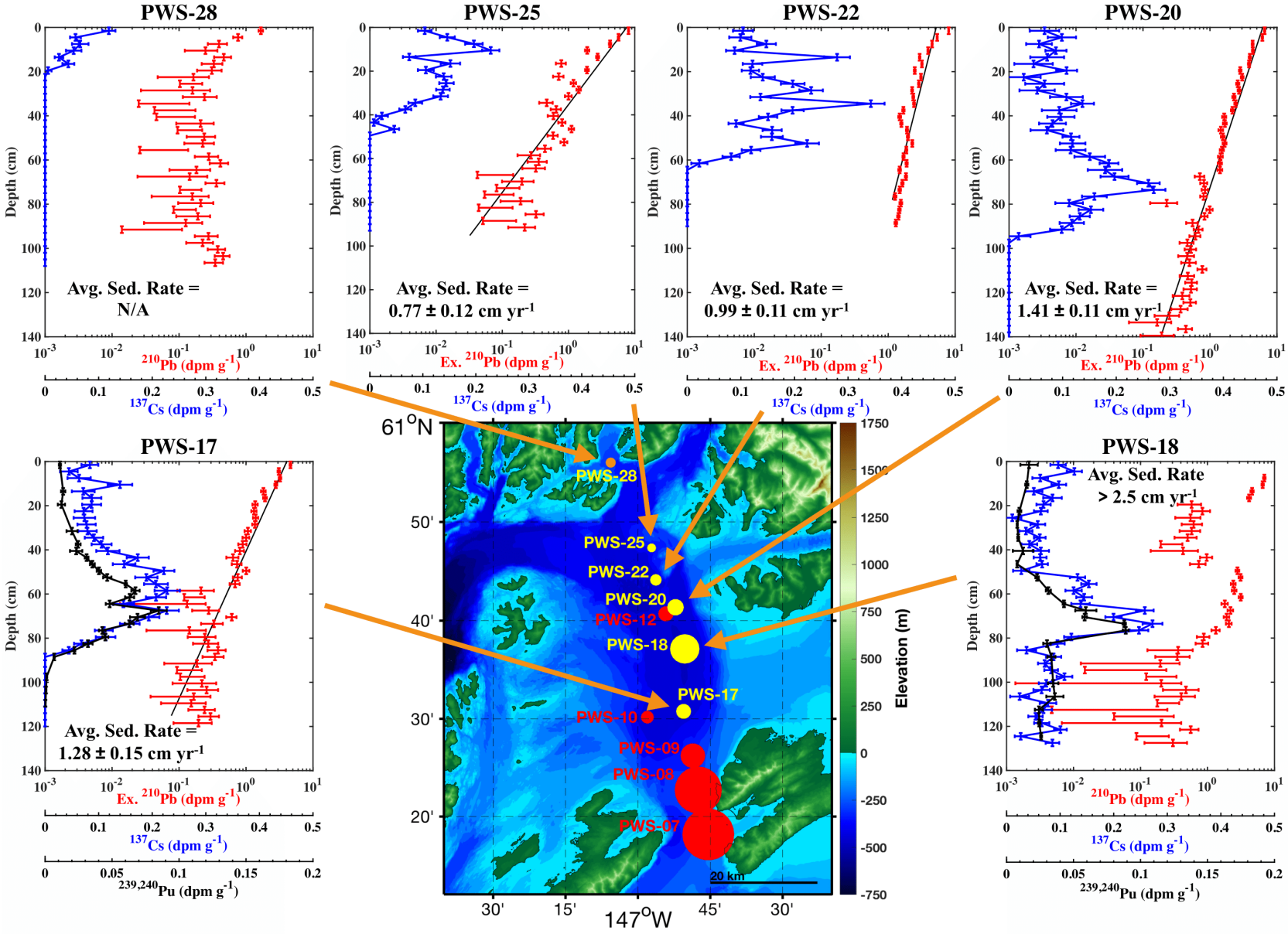
PWS-28
Avg. Sed. Rate = N/A
PWS-25
Avg. Sed. Rate = 0.77 ± 0.12 cm yr-1
PWS-22
Avg. Sed. Rate = 0.99 ± 0.11 cm yr-1
PWS-20
Avg. Sed. Rate = 1.41 ± 0.11 cm yr-1
PWS-17
Avg. Sed. Rate = 1.28 ± 0.15 cm yr-1
PWS-18
Avg. Sed. Rate > 2.5 cm yr-1
Depth (cm)
210Pb (dpm g-1)
Ex. 210Pb (dpm g-1)
137Cs (dpm g-1)
239,240Pu (dpm g-1)
61°N
50'
40'
30'
20'
30'
15'
147°W
45'
30'
PWS-28
PWS-25
PWS-22
PWS-20
PWS-12
PWS-18
PWS-17
PWS-10
PWS-09
PWS-08
PWS-07
20 km
Elevation (m)
1750
1500
1250
1000
750
500
250
0
-250
-500
-750

Figure 19. Geochronological data for the 2016 PWS cores PWS-(17, 18, 20, 22, 25, 28). All plots show the total ^{137}Cs and $^{239,240}Pu$ (where applicable) and the excess ^{210}Pb values (note: logarithmic scale), with the exception of PWS-28 which shows total ^{210}Pb. The average sedimentation rates and core locations are also included. Each isotope is plotted on a separate axis, with the top axis being ^{210}Pb, the middle ^{137}Cs, and the bottom $^{239,240}Pu$. The red dots correspond to cores collected in 2012 (Miller, 2014) and the yellow to cores collected in 2016. The relative size of the dot represents the magnitude of the average sedimentation rate (Table 2).

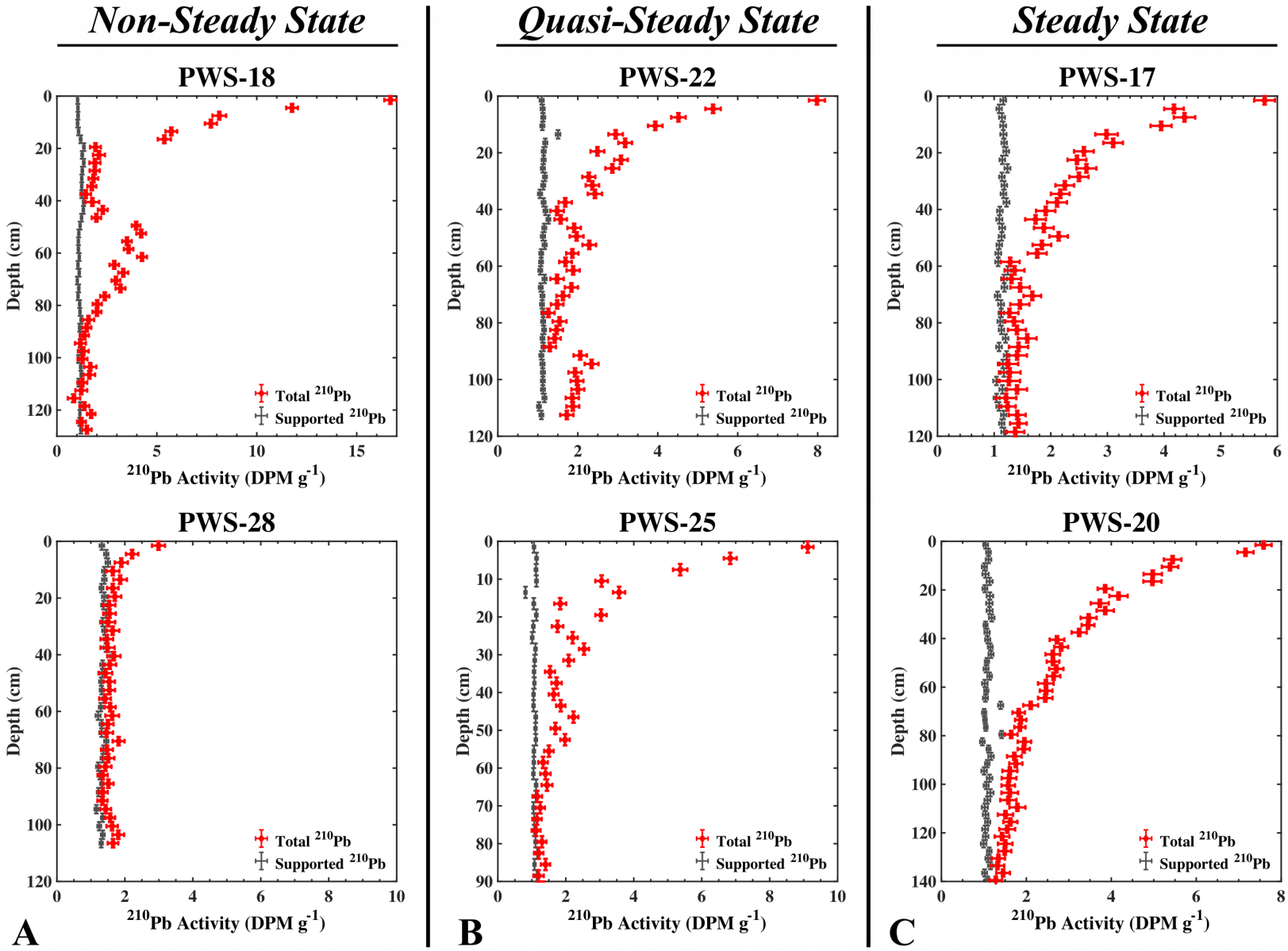
Non-Steady State
Quasi-Steady State
Steady State
PWS-18
PWS-22
PWS-17
PWS-28
PWS-25
PWS-20
Depth (cm)
^{210}Pb Activity (DPM g^{-1})
Total ^{210}Pb
Supported ^{210}Pb
A
B
C

Figure 20. Total ^{210}Pb profiles for cores collected in 2016 characterized as: A. Non-Steady State, B. Quasi-Steady State, and C. Steady State for the sedimentation rate calculation. The sedimentation rates in the steady- and quasi-steady state cores were calculated using the Constant Flux : Constant Supply (CF:CS) model and equation 2. Reliable sedimentation rates could not be calculated for non-steady state cores. Causes for the quasi- and non-steady state profiles are explored in the discussion.

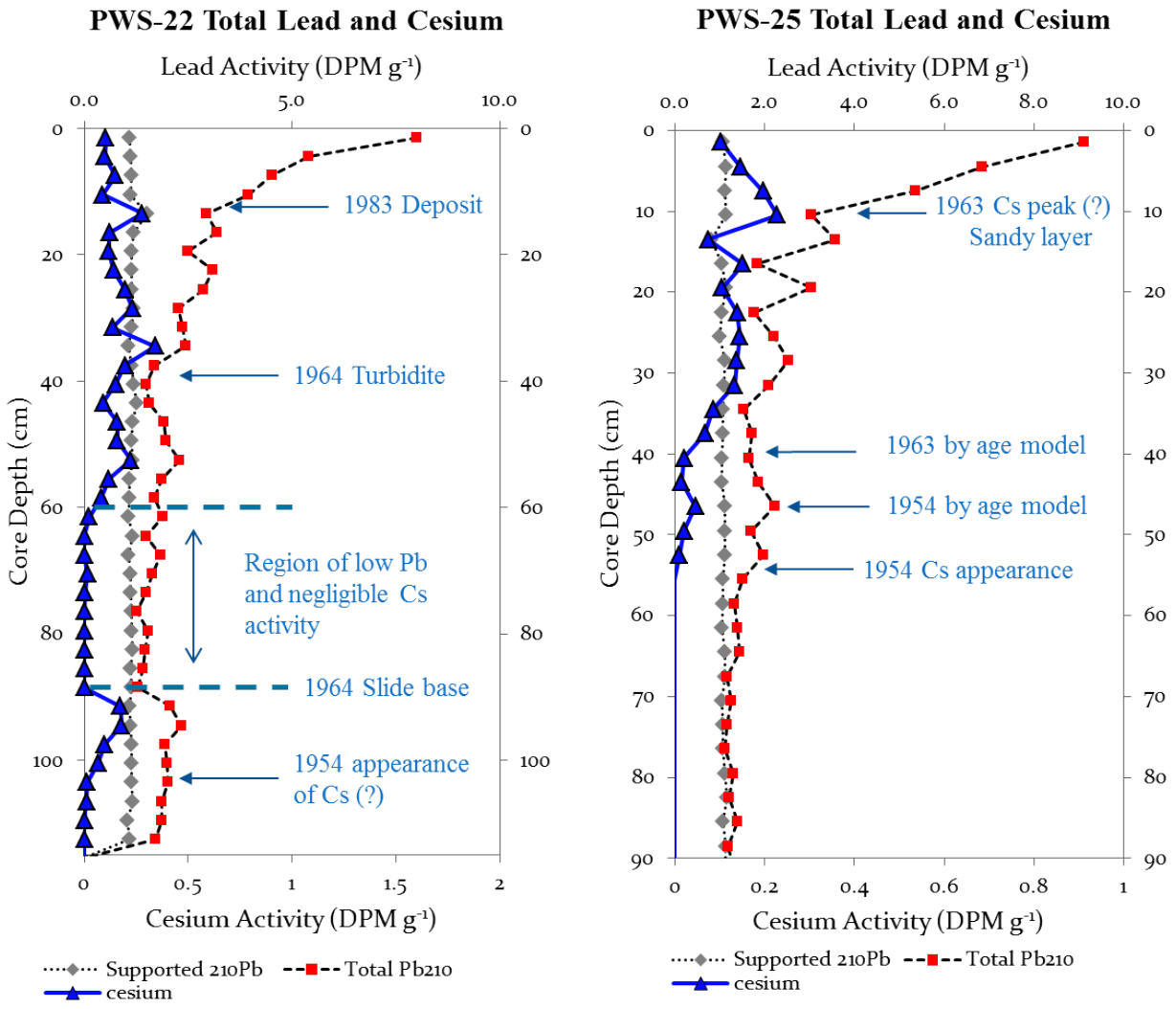

Figure 21. Plots of total and supported ^{210}Pb and ^{137}Cs activity in PWS-22 and PWS-25, which display quasi-steady state behavior. In PWS-22, the reappearance of ^{137}Cs at depth 90 cm along with an increase in excess lead suggests a potential slide occurd in 1964 and placed older sediment from upslope overtop younger sediments before the turbidity current passed the site and left the deposit from 34 to 46 cm. In PWS-25, the first appearance of ^{137}Cs occurs ~15 cm below the depth estimated by the age model, while the 1963 'peak' occurs 30 cm above the model depth estimate for 1963. There are fluctuations in total ^{210}Pb from 10-20 cm which are unnassociated with event deposits in the XRF, stable isotope, and grain size data and the visual/X-radiograph images.

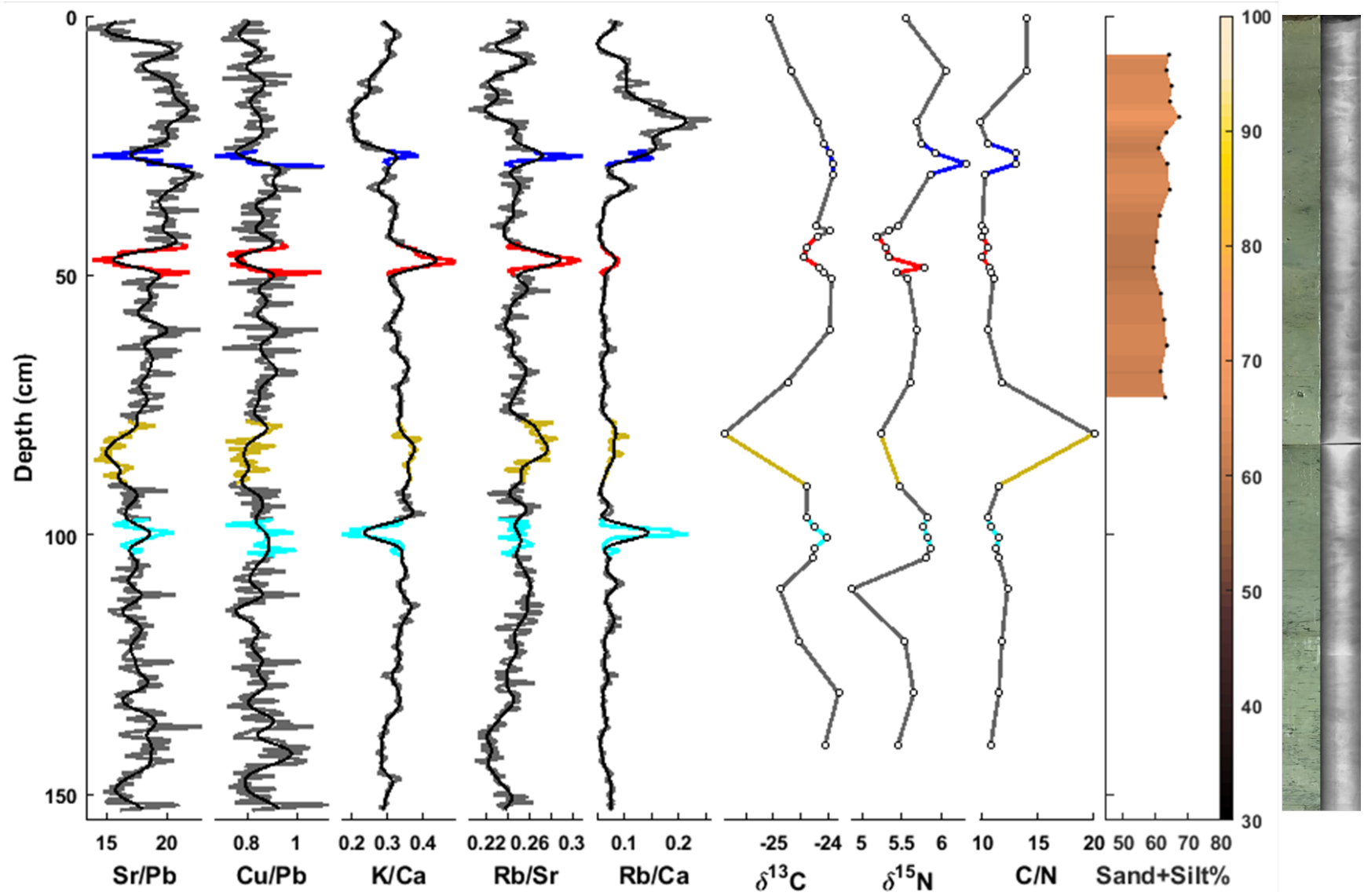
PWS-10
Depth (cm)
0
50
100
150
15 20
Sr/Pb
0.8 1
Cu/Pb
0.2 0.3 0.4
K/Ca
0.22 0.26 0.3
Rb/Sr
0.1 0.2
Rb/Ca
-25 -24
δ13C
5 5.5 6
δ15N
10 15 20
C/N
50 60 70 80
Sand+Silt%
100
90
80
70
60
50
40
30

Figure 22. From left to right: XRF ratios Sr/Pb, Cu/Pb, K/Ca, Rb/Sr, and Rb/Ca, $\delta^{13}C$, $\delta^{15}N$, C/N, and grain size data plotted alongside the visual/negative X-radiograph images of PWS-10. The 1983 (dark blue), 1964 (red), 1928 (yellow), and 1912 (light blue) inferred gravity flow deposits are highlighted. This core was collected in the southern end of the central channel by Miller (2014). Organic carbon data is from this study, the rest of the data is from Miller (2014).

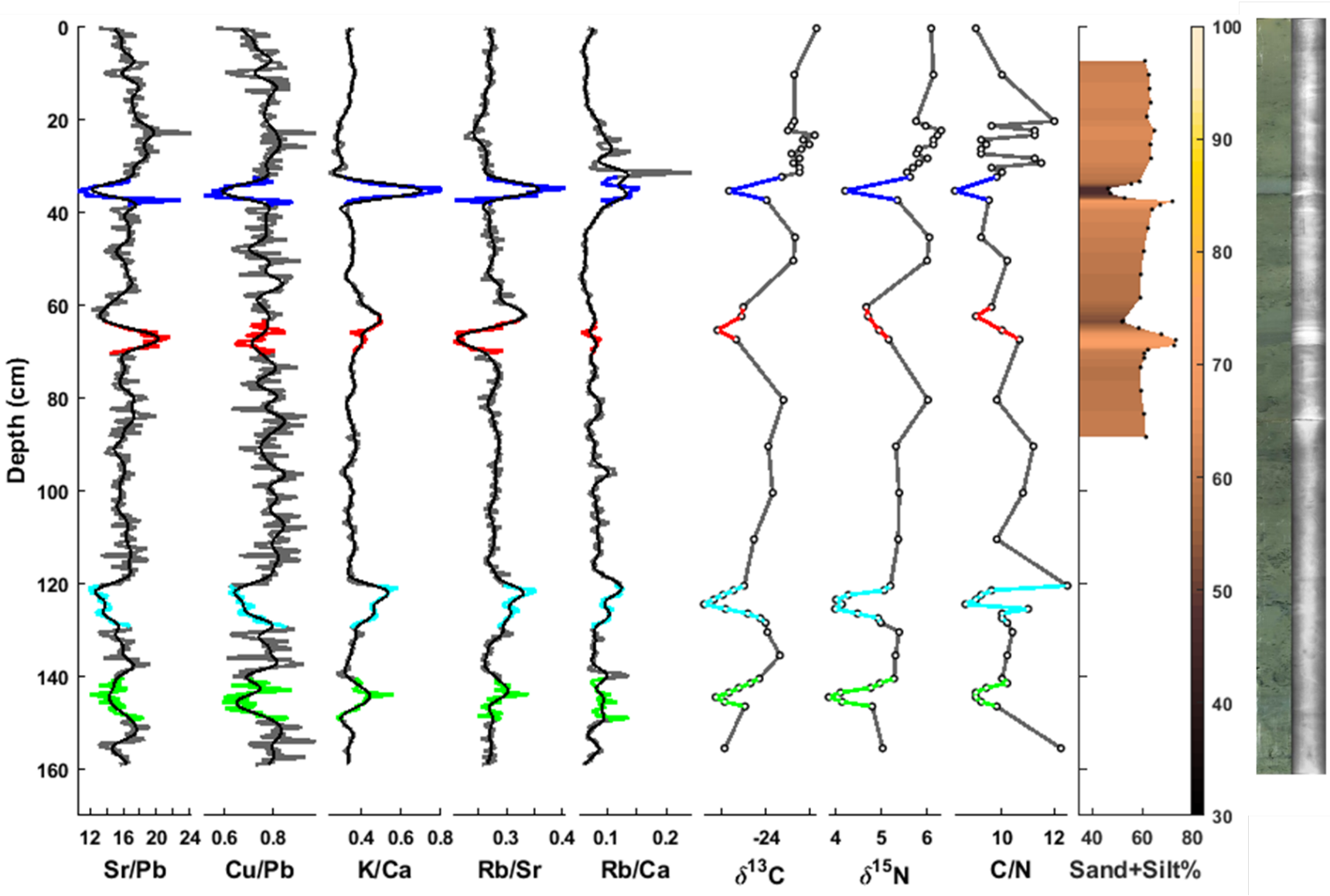
PWS-12
Depth (cm)
0
20
40
60
80
100
120
140
160
12 16 20 24
Sr/Pb
0.6 0.8
Cu/Pb
0.4 0.6 0.8
K/Ca
0.3 0.4
Rb/Sr
0.1 0.2
Rb/Ca
-24
$\delta^{13}C$
4 5 6
$\delta^{15}N$
10 12
C/N
40 60 80
Sand+Silt%
100
90
80
70
60
50
40
30

Figure 23. From left to right: XRF ratios Sr/Pb, Cu/Pb, K/Ca, Rb/Sr, and Rb/Ca, $\delta^{13}C$, $\delta^{15}N$, C/N, and grain size data plotted alongside the visual/negative X-radiograph images of PWS-12. The 1983 (dark blue), 1964 (red), 1912 (light blue), and 1899 (green) inferred gravity flow deposits are highlighted. This core was collected in the central channel by Miller (2014). Organic carbon data is from this study, the rest of the data is from Miller (2014).

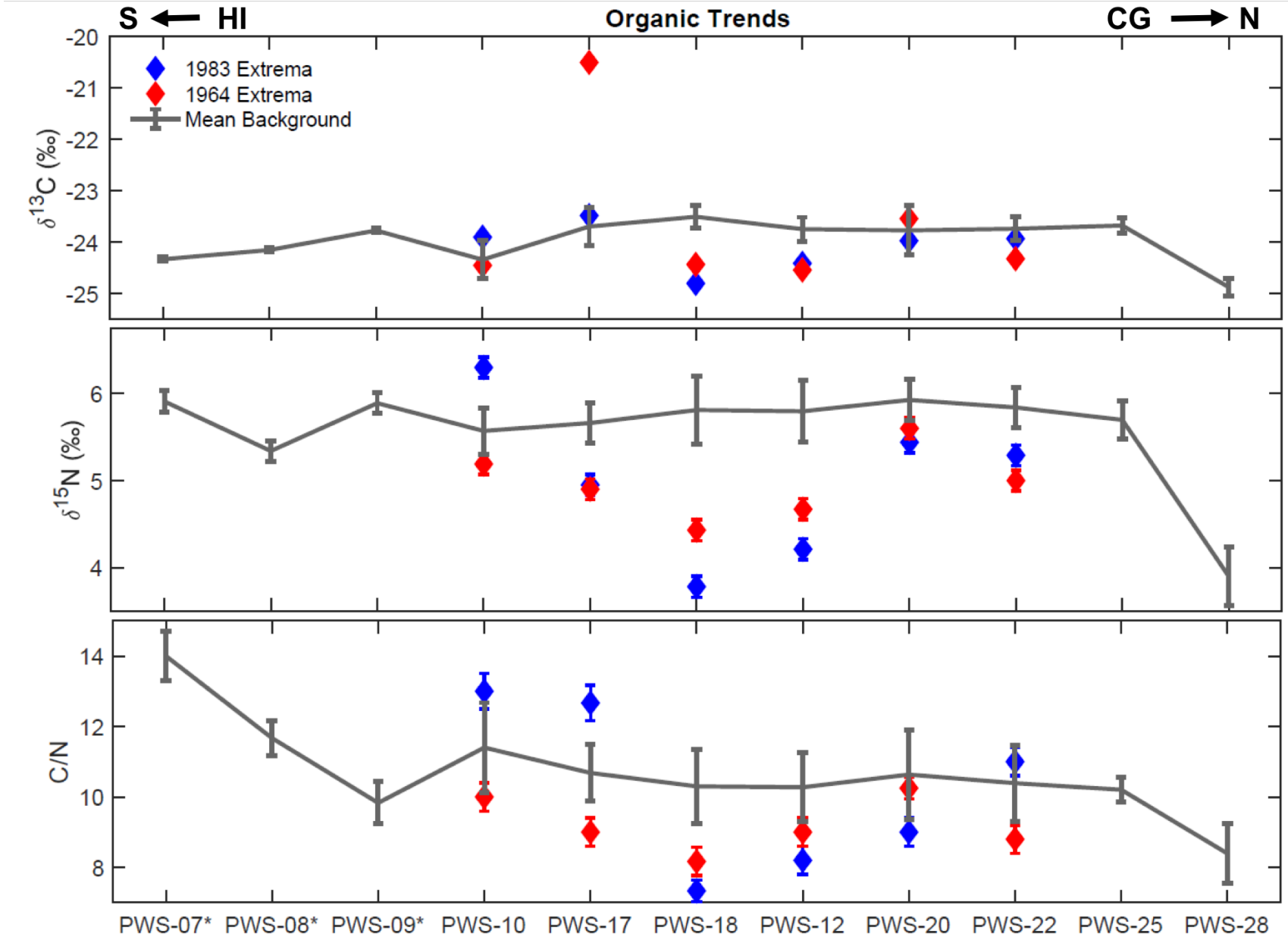
S ← HI
Organic Trends
CG → N
1983 Extrema
1964 Extrema
Mean Background
δ13C (‰)
δ15N (‰)
C/N
PWS-07*
PWS-08*
PWS-09*
PWS-10
PWS-17
PWS-18
PWS-12
PWS-20
PWS-22
PWS-25
PWS-28

Figure 24. Plots of $\delta^{13}C$ (top), $\delta^{15}N$ (middle), and C/N (bottom) values in the background (defined as any sediment not part of a gravity flow deposit, gray line) and the 1983 (blue) and 1964 (red) inferred gravity flow deposits in each core from south to north. In PWS-10 through PWS-28, the background values are the means ± standard deviation and the deposit values are the extrema ± instrumental error. The 1983 deposit maxima in all values in PWS-10, and maxima in $\delta^{13}C$ and C/N in PWS-17, the rest are all minima. The 1964 deposit has maxima in the $\delta^{13}C$ of PWS-17 and PWS-20 and a maxima in C/N in PWS-20, the rest are all minima. Error bars are not shown for extrema on $\delta^{13}C$ because the marker size is larger than the bars. Refer to Fig. 27 for 1964 and Fig. 30 for 1983 to see which deposits contain maxima vs minima. *Stable isotopes were only measured in the surface (0 - 3 cm) of PWS-(07, 08, 09), and are plotted as part of the background ± instrumental error. There is a decreasing northward trend in C/N from PWS-07 to PWS-09, which is mirrored by a slight increasing trend in $\delta^{13}C$. The deposit extrema general fall below background levels. The most significant exception to this trend is the peak of $\delta^{13}C$ in the base of the 1964 deposit in PWS-17 (Fig. 12).

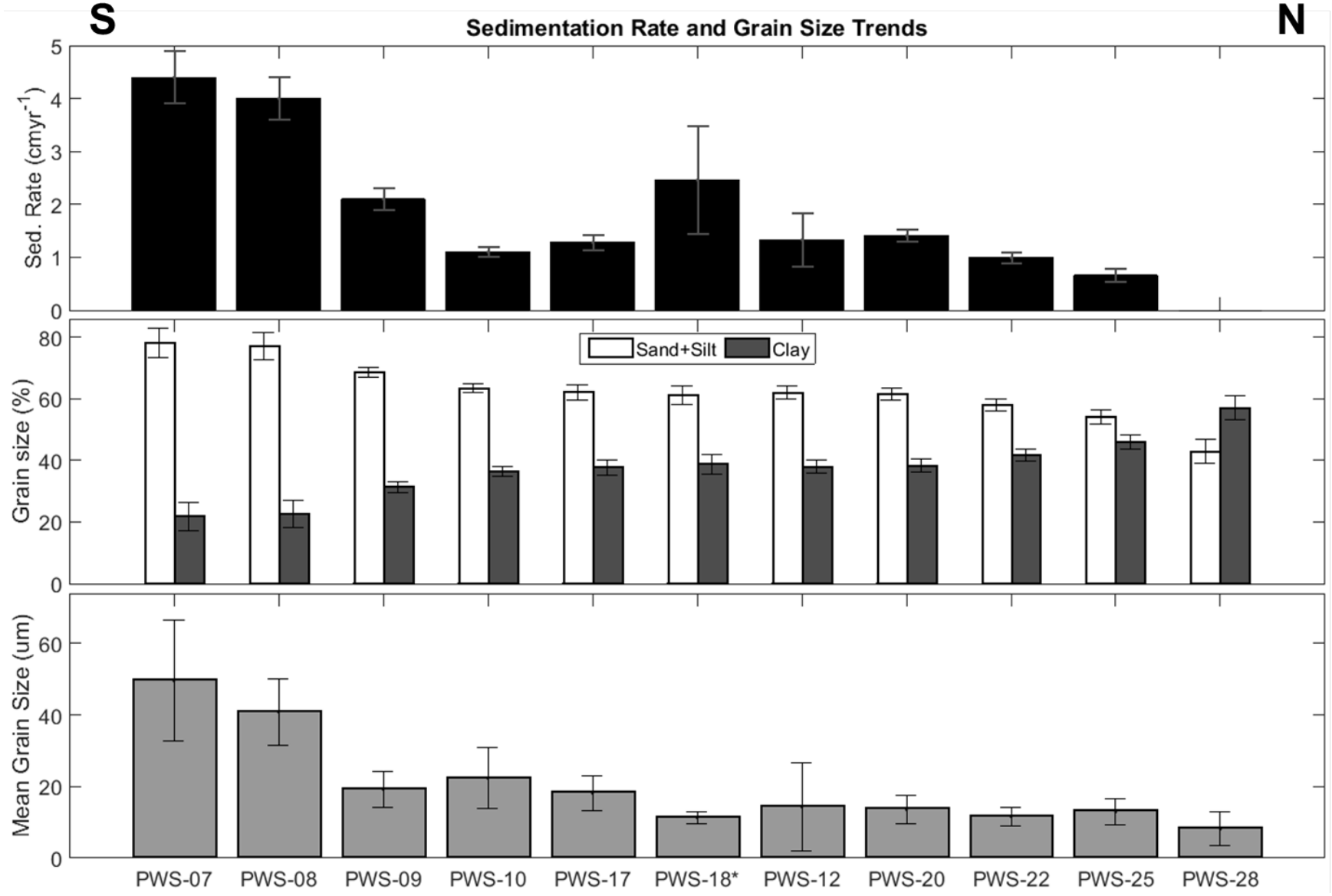
S
Sedimentation Rate and Grain Size Trends
N
Sed. Rate (cmyr-1)
Grain size (%)
Sand+Silt
Clay
Mean Grain Size (um)
PWS-07
PWS-08
PWS-09
PWS-10
PWS-17
PWS-18*
PWS-12
PWS-20
PWS-22
PWS-25
PWS-28

Figure 25. Plots of sedimentation rate (top), percent sand+silt and clay (middle), and mean grain size (bottom) for the background (define as any sediment not part of a gravity flow deposit) in each core from south to north. Grain size data was gather and sedimentation rate calculations done for PWS-(07, 08, 09, 10, 12) by Miller (2014). *The PWS-18 rate plotted is the ^{137}Cs, $^{239,240}Pu$ max penetration estimate. Error bars on the sedimentation rate are the same shown in Table 2. Error bars on the grain size and % and mean represent the whole-core standard deviation. There is a trend of decreasing sedimentation rate, sand+silt content, and mean grain size with increasing clay content moving northward from HI (PWS-07) towards CG (PWS-28).

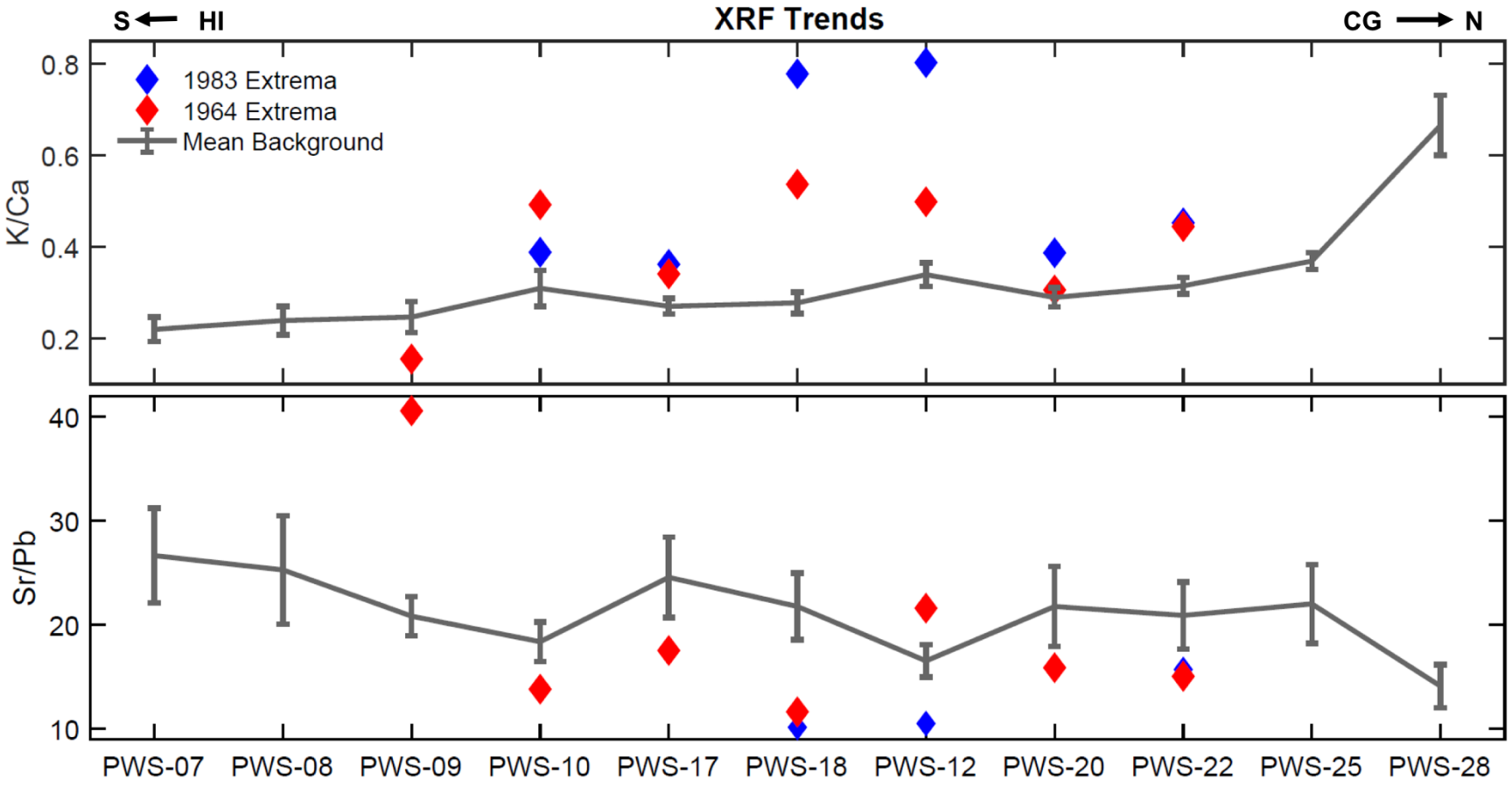
S ← HI
XRF Trends
CG → N
1983 Extrema
1964 Extrema
Mean Background
K/Ca
0.8
0.6
0.4
0.2
Sr/Pb
40
30
20
10
PWS-07
PWS-08
PWS-09
PWS-10
PWS-17
PWS-18
PWS-12
PWS-20
PWS-22
PWS-25
PWS-28

Figure 26. Plots of K/Ca (top) and Sr/Pb (bottom) values in the background (define as any sediment not part of a gravity flow deposit, gray line) and the 1983 (blue) and 1964 (red) gravity flow deposits in each core from south to north. XRF data for PWS-(07, 08, 09, 10, 12) were gathered by Miller (2014). The background values are the mean ± standard deviation, while the deposit values are the extrema. The 1983 deposits all have maxima in K/Ca and minima in Sr/Pb. The 1964 deposits have maxima in K/Ca and minima in Sr/Pb in all but PWS-09 (min in K/Ca and max in Sr/Pb) and PWS-12 (max in both). The instrumental error is smaller than the marker size, so no error bars are shown on the deposit extrema. Refer to Fig. 27 for 1964 and Fig. 30 for 1983 to see which deposits contain maxima vs minima. The deposit extrema plot above the background in K/Ca and below the background in Sr/Pb, indicating the 1964 and 1983 flows were sourced from local PWS sediment with the exception of the 1964 deposit in PWS-09. The highest K/Ca signatures occur in the 1983 deposit in PWS-12 and PWS-18, and their values are higher than the mean background of PWS-28, which serves as an endmember for Columbia Glacier and northern PWS sediment. Likewise, the Sr/Pb signature in the 1983 deposit of these two cores is lower than PWS-28.

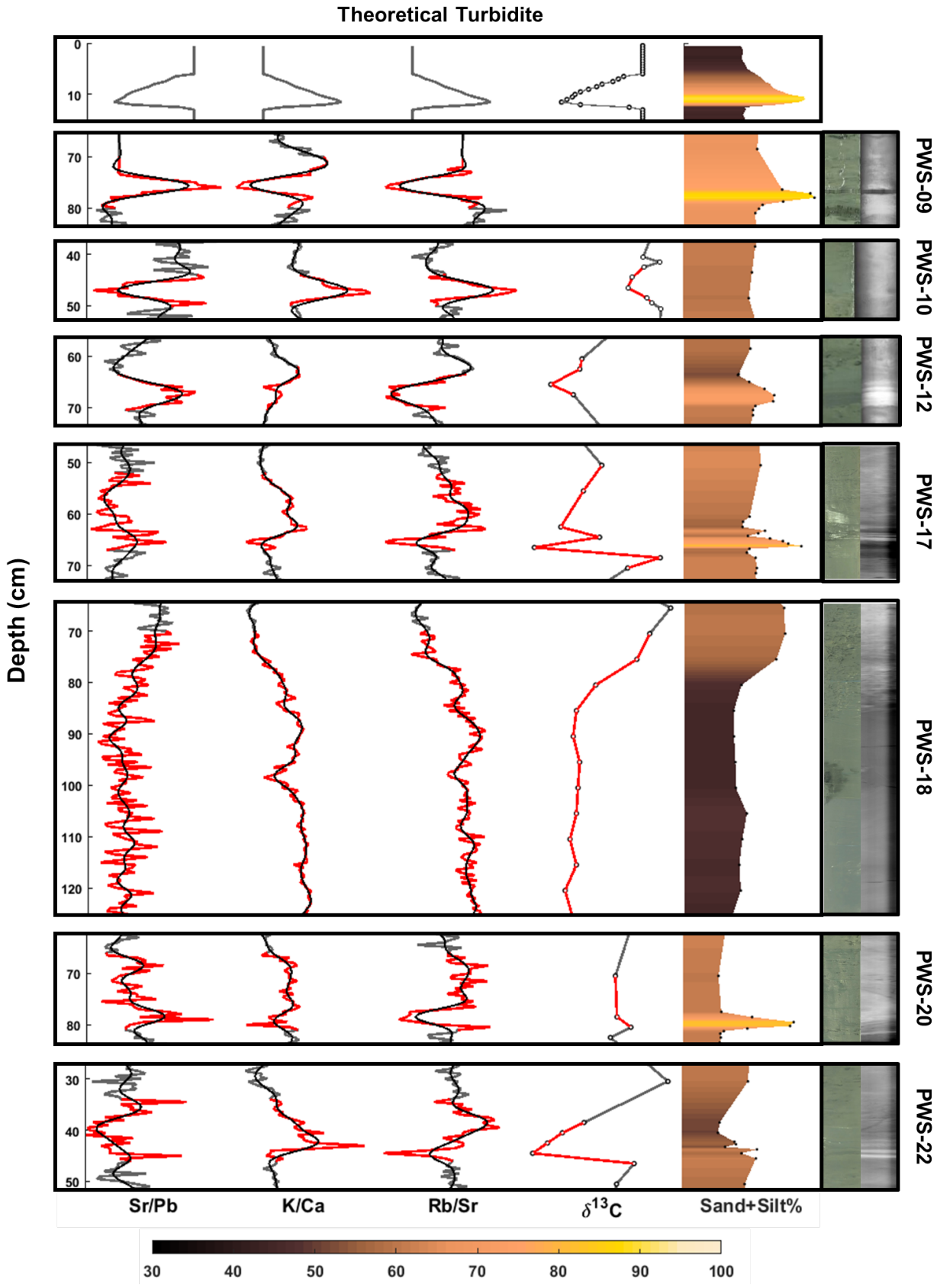
Theoretical Turbidite
Depth (cm)
PWS-09
PWS-10
PWS-12
PWS-17
PWS-18
PWS-20
PWS-22
Sr/Pb
K/Ca
Rb/Sr
δ13C
Sand+Silt%
30
40
50
60
70
80
90
100

Figure 27. Comparison of the 1964 gravity flow deposit composition in the XRF, $\delta^{13}C$, grain size, and visual/X-radiograph data between all cores with distinguishable deposits. XRF, Grain size, and visual/X-radiograph data for PWS-(09, 10, 12) were gathered by Miller (2014). The theoretical structure of a turbidite is displayed at the top for comparison with the observed turbidites. The grain size color bar for percent sand+silt is displayed at the bottom. The XRF and stable isotope scales have been stretched per each core to best emphasize the extrema for comparison between coring sites. In general the K/Ca and Rb/Sr is higher while the Sr/Pb is lower with the exception of coarser layers where the Sr/Pb has a maxima and K/Ca and Rb/Sr have minima (e.g., PWS-(12, 17, 20)). The $\delta^{13}C$ is generally lower within deposits. There are generally coarse layers at the base of the deposit, suggesting it is a turbidite. PWS-10 was only coarsely sampled and likely occurred at the limit of runout which may account of the lack of a coarse basal layer. PWS-18 was not long enough to capture the base, but there is a slight increase in sand+silt content around 105 cm, suggesting it may have a coarser base.

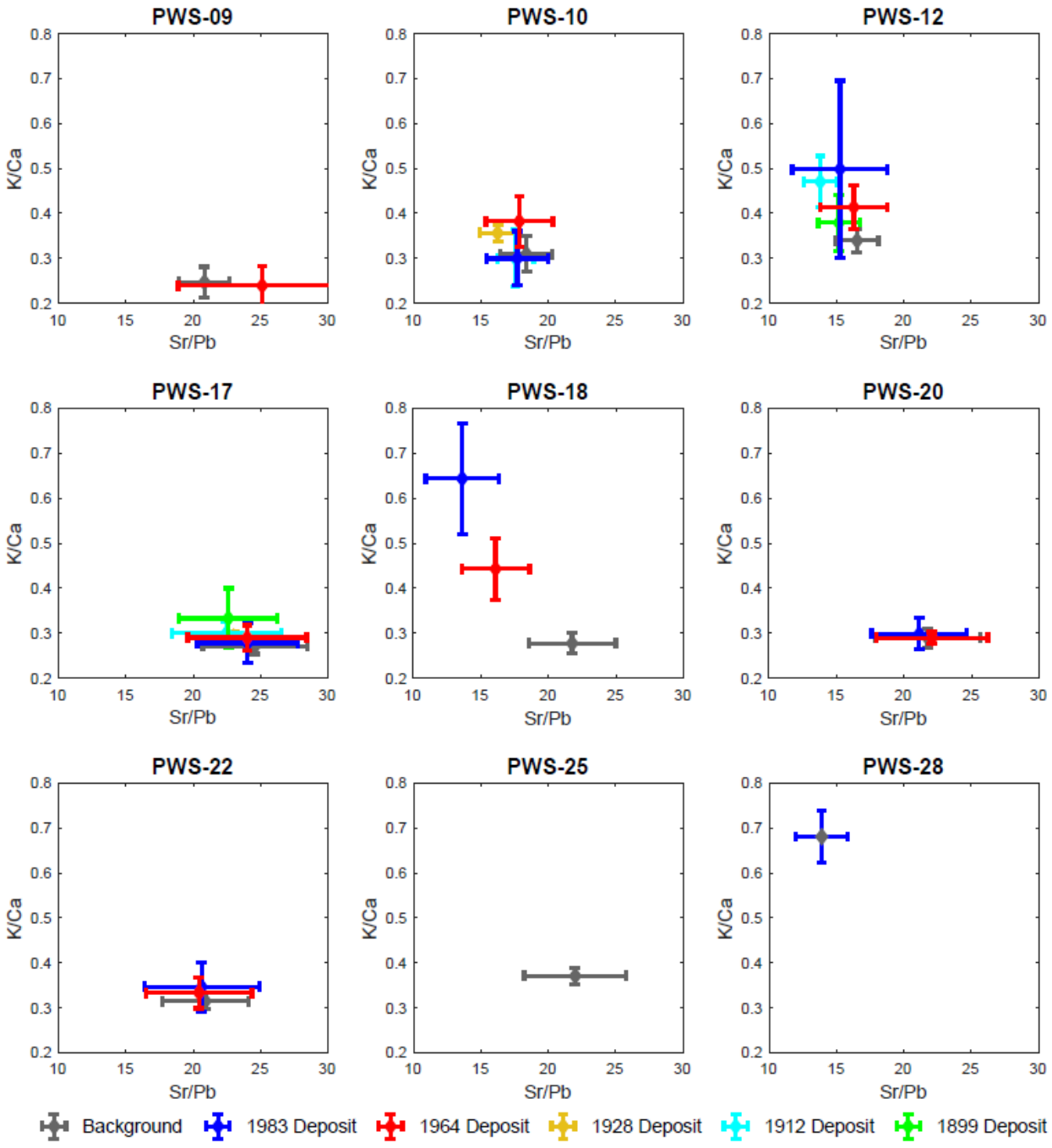
PWS-09
PWS-10
PWS-12
PWS-17
PWS-18
PWS-20
PWS-22
PWS-25
PWS-28
K/Ca
Sr/Pb
0.2
0.3
0.4
0.5
0.6
0.7
0.8
10
15
20
25
30
Background
1983 Deposit
1964 Deposit
1928 Deposit
1912 Deposit
1899 Deposit

Figure 28. Plots of K/Ca (local PWS signature) versus Sr/Pb (CR signature) per core. XRF data for PWS-(09, 10, 12) were gathered by Miller (2014). The mean value of each inferred gravity flow deposit is plotted with standard deviation error bars. Any sediment not related to the deposits is plotted as the mean background in gray. The mean background in PWS-28 serves as an endmember for Columbia Glacier sediment and is plotted in gray and blue. PWS-12 and PWS-18 have the highest degree of deviation between deposit and background signatures. The 1983 deposits in these cores have the lowest Sr/Pb and highest K/Ca signatures and fall within the range of the Columbia Glacier sediment, while the 1964 deposits have mix signatures between the 1983 deposits and the background. A similar trend is observed in the stable isotope data in Fig. 29.

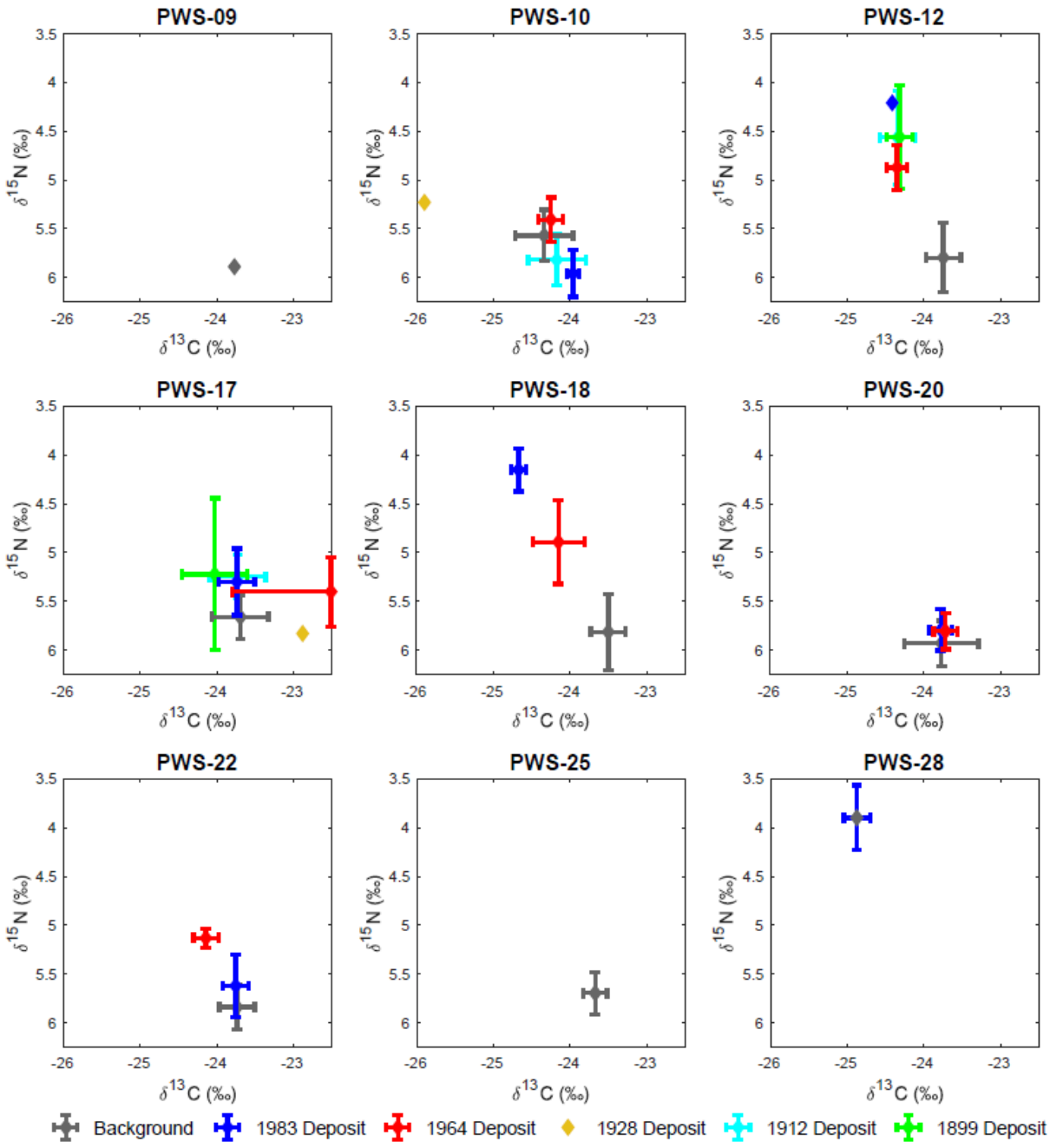
PWS-09
PWS-10
PWS-12
PWS-17
PWS-18
PWS-20
PWS-22
PWS-25
PWS-28
δ15N (‰)
δ13C (‰)
3.5
4
4.5
5
5.5
6
-26
-25
-24
-23
Background
1983 Deposit
1964 Deposit
1928 Deposit
1912 Deposit
1899 Deposit

Figure 29. Plots of $\delta^{15}N$ versus $\delta^{13}C$ per core. The mean value of each deposit is plotted with standard deviation error bars. Any sediment not related to the deposits is plotted as the mean background in gray. Samples with lower $\delta^{15}N$ and $\delta^{13}C$ plot towards the upper right while higher signatures plot towards the lower left. The mean background in PWS-28 serves as an endmember for Columbia Glacier sediment, is plotted in gray and blue, and has the lowest signatures observed. The single background sample in PWS-09 is the top 0 – 3 cm of the core and represents southern PWS signatures, and the 1928 deposits in PWS-10 and PWS-17 were likewise sampled with only one point, thus contain no standard deviation error bars. The 1983 deposit in PWS-12 could only be sampled from 3 cm intervals previously composited by Miller (2014), thus higher resolution sampling was not possible. The data points from the top and bottom of the deposit were mixed with background sediment which diluted the signatures, so only the sample from the center of the deposit is plotted. Similar to the trends observed in Fig. 28, cores PWS-12 and PWS-18 have the highest degree of deviation between deposit and background signatures, with the 1983 deposit close in value to Columbia Glacier sediment and the 1964 deposit falling between 1983 and the background.

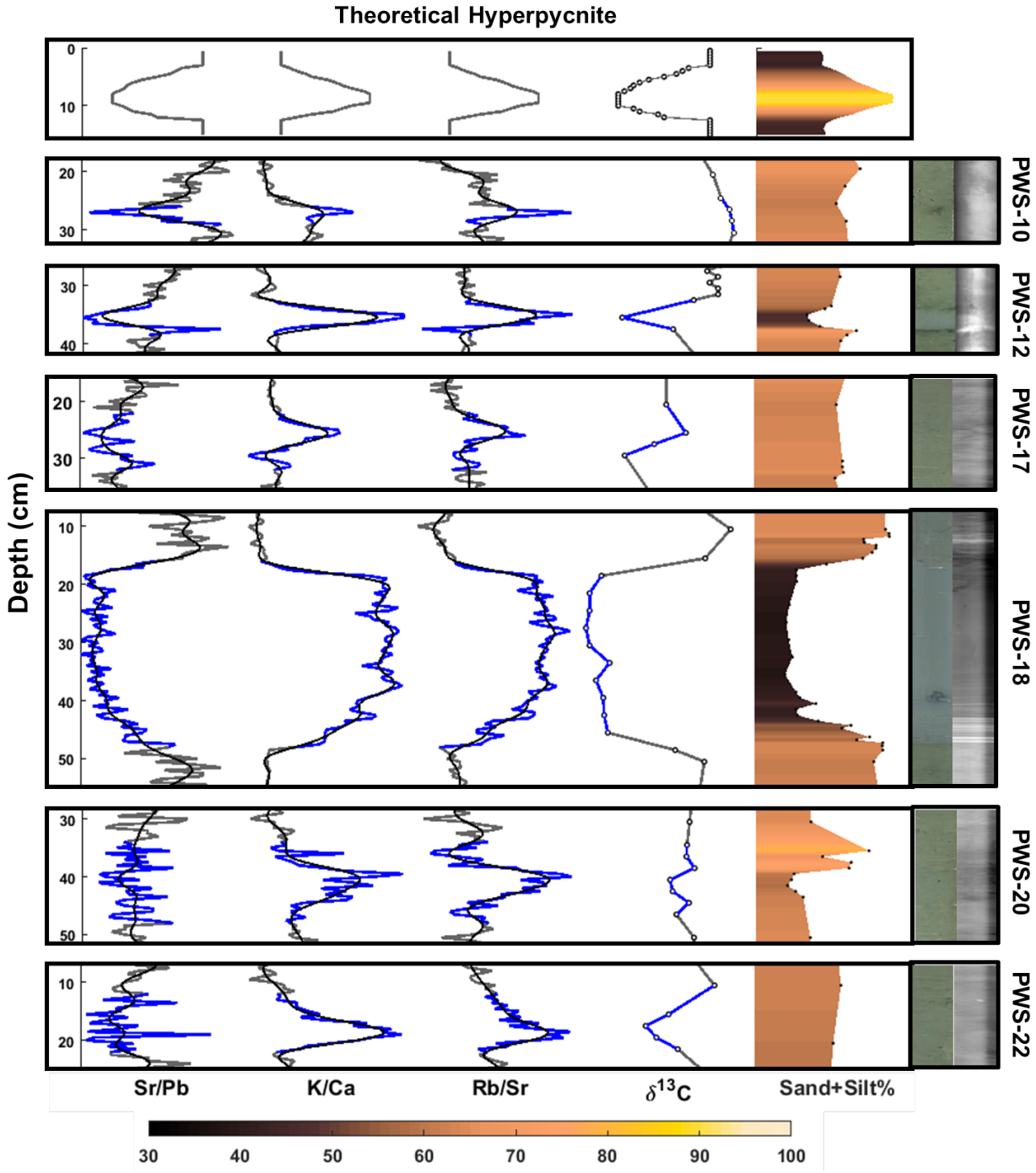
Theoretical Hyperpycnite
Depth (cm)
PWS-10
PWS-12
PWS-17
PWS-18
PWS-20
PWS-22
Sr/Pb
K/Ca
Rb/Sr
δ13C
Sand+Silt%
30
40
50
60
70
80
90
100

Figure 30. Comparison of the 1983 gravity flow deposit composition in the XRF, $\delta^{13}C$, grain size, and visual/X-radiograph data between all cores with distinguishable deposits. XRF, Grain size, and visual/X-radiograph data for PWS-10 and PWS-12 were gathered by Miller (2014). Black dots on the grain size image indicate where sampling was done. The theoretical structure of a hyperpycnite is displayed at the top for comparison with the observed deposits. The grain size color bar for percent sand+silt is displayed at the bottom. The XRF and stable isotope scales have been stretched per each core to best emphasize the extrema for comparison between coring sites. The K/Ca and Rb/Sr are consistently higher while Sr/Pb is lower in all deposits, and the $\delta^{13}C$ is generally lower. There are lamina at the base of the deposit in PWS-12 and PWS-18 that are overlain by sections of finer particles, while PWS-20 has a coarse layer which occurs above the K/Ca and Rb/Sr maxima. The grain size structure does not fit the theoretical structure of a turbidite or a hyperpycnite and may depict a flow predominantly composed of finer particles.

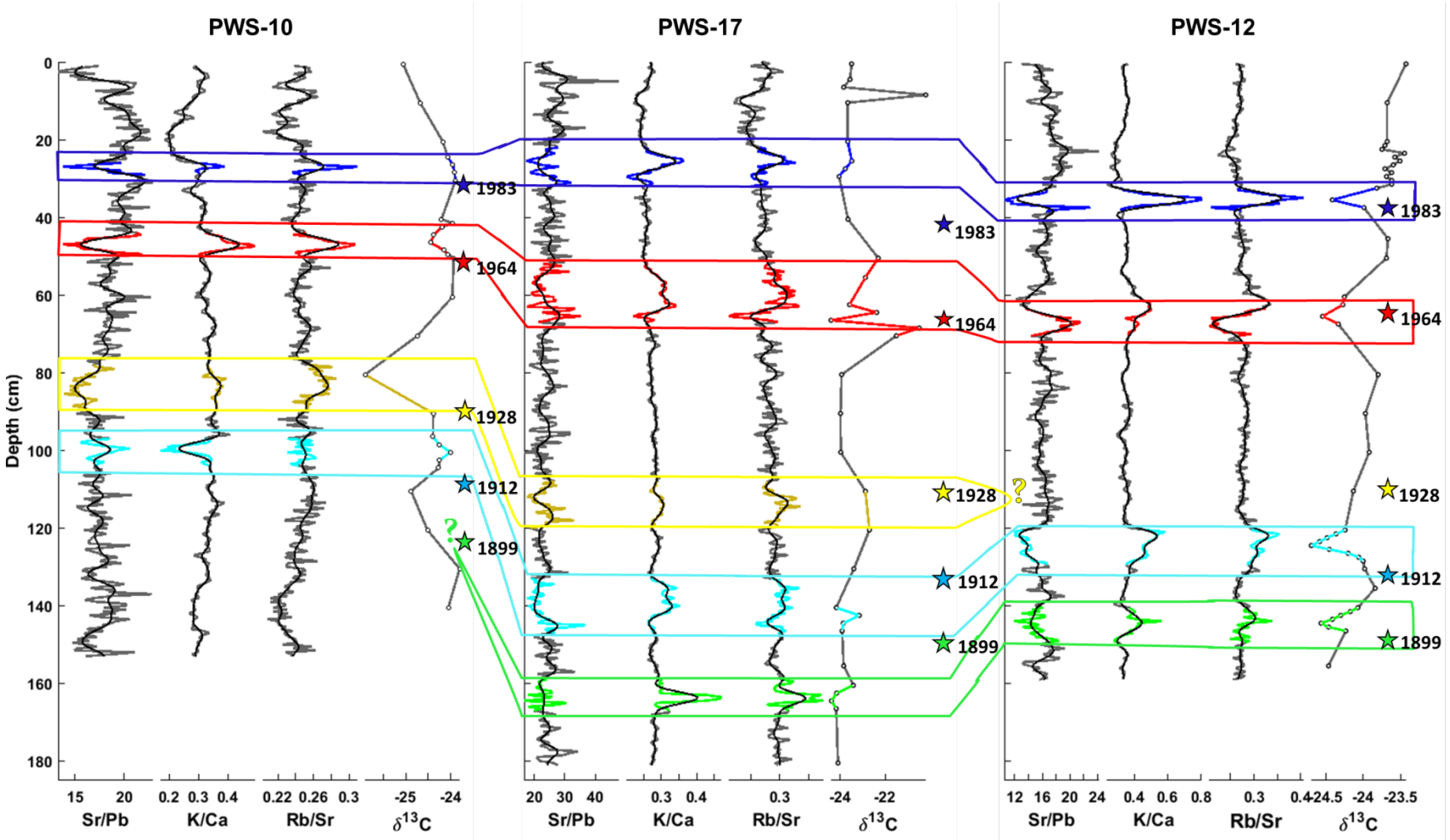
PWS-10
PWS-17
PWS-12
Depth (cm)
0
20
40
60
80
100
120
140
160
180
1983
1964
1928
1912
1899
?
15 20
Sr/Pb
0.2 0.3 0.4
K/Ca
0.22 0.26 0.3
Rb/Sr
-25 -24
δ13C
20 30 40
0.3 0.4
0.3
-24 -22
12 16 20 24
0.4 0.6 0.8
0.3 0.4
-24.5 -24 -23.5

Figure 31. Correlation of deposits between the XRF ratios Sr/Pb, K/Ca, and Rb/Sr, and $\delta^{13}C$ values in PWS-(10, 12) from Miller (2014) and PWS-17 (this study). Along with the 1983 (blue) and 1964 (red) gravity flow deposits also present in PWS-(09, 18, 20, 22),these cores contained additional deposits from 1928 (yellow), 1912 (bright blue), and 1899 (green). This region appears to be more sensitive to gravity flow events than cores near HI and the eastern channel flank. The dated depths of earthquakes which may have triggered these flows are marked with a star of corresponding color using the average sedimentation rates from Table 2. The 1928 M_w = 6.8 earthquake may have generated a local flow in southern PWS near the epicenter. The 1912 event has differing signatures across all three cores, that suggests the 1912 M_w=7.25 earthquake may have generated multiple flows around PWS which were delivered to the central channel. The 1899 event is associated with a M_w > 8.0 earthquake which occurred over 300 km away from PWS but caused documented submarine landslides in Valdez. The PWS signatures, low $\delta^{13}C$, and runout of the deposit (i.e., reaching limit of runout before PWS-10) suggest only a northern flow occurred.

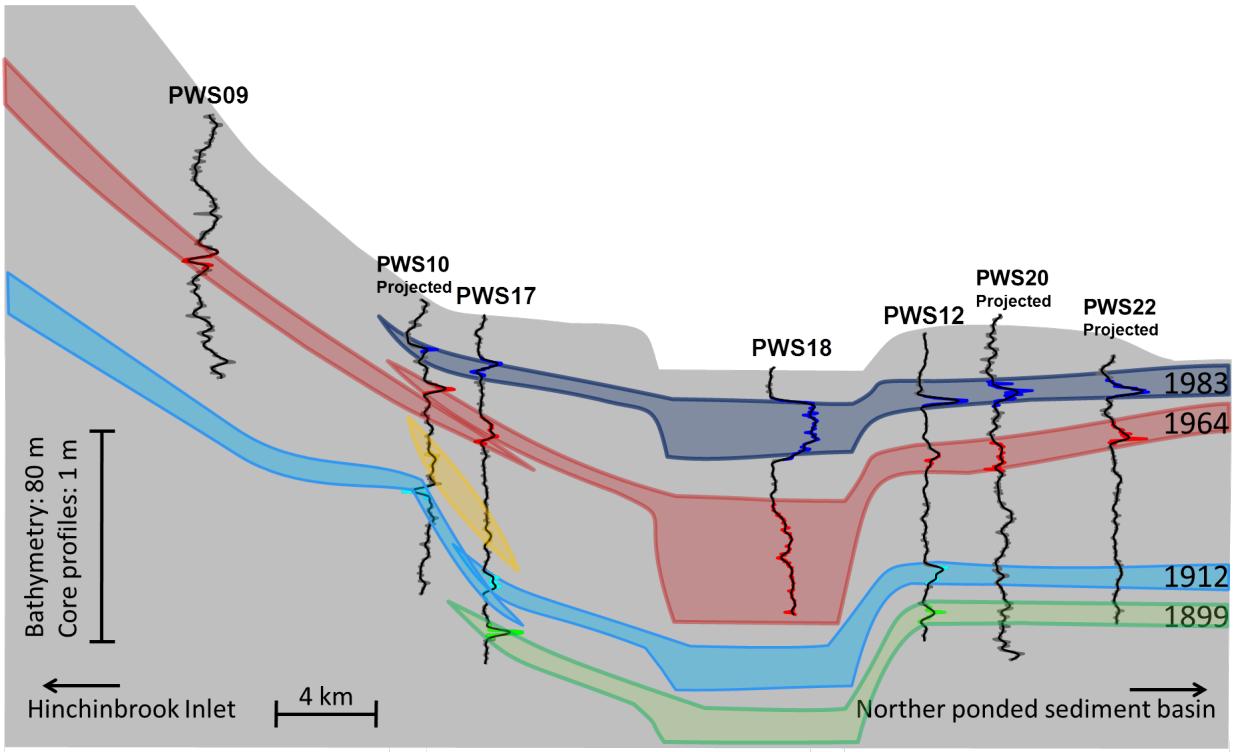

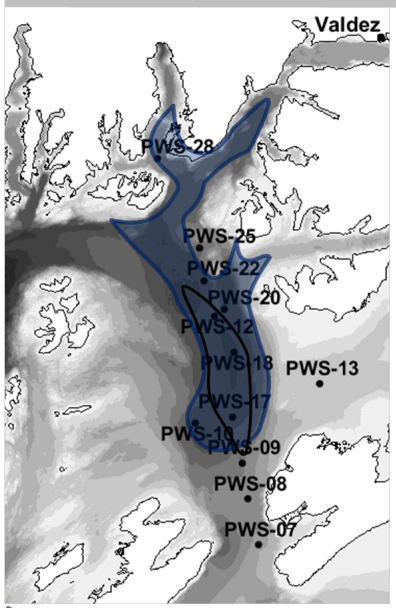

1983 flow

Best paleoseismic record

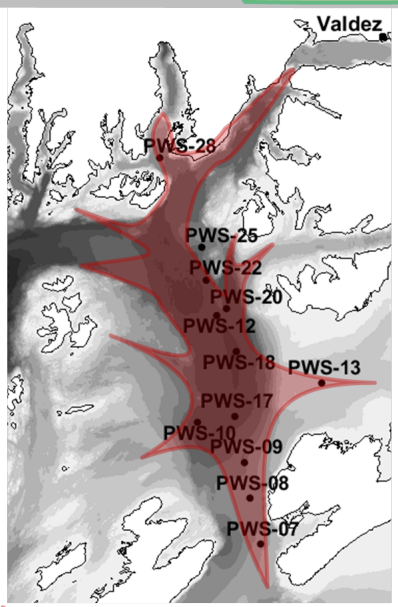

1964 Turbidity currents

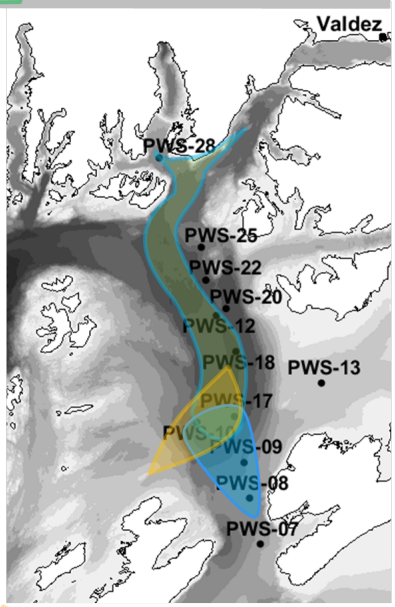

1928 flow

1912 southern flow

1912/1899 northern flow

Figure 32. Top: Cartoon cross section from HI to the northern ponded sediment basin. K/Ca ratios from each core location are shown and used to draw the theorized extent of all deposits observed in this study. The vertical bathymetry exaggeration is 150x while the core profiles and deposit thicknesses are 12000x. Core profiles for PWS-(10, 20, 22) are projected onto the cross section because they are offset to the west (PWS-10) and east (PWS-20 and PWS-22) of the cross section. PWS-10 does not intersect the path of the southern 1964 gravity flow, and PWS-20 and PWS-22 do not intersect the path of the 1912 and 1899 flows. The 1928 flow was sourced to the west of the cartoon cross section and flowed eastward to PWS-10 and PWS-17 rather than the north-south direct of the other flows. Bottom: Maps of the inferred gravity flow path associated with 1983 (left), 1964 (middle), and the older three turbidites (right). The region within the central channel with the most distinct deposits in XRF and stable isotope signatures (Figs. 28 and 29) and the highest sensitivity to flows (i.e., most likely to receive gravity flow deposition) is indicated by a black outline on the 1983 map.